

# TARGETING OF SUPPRESSIVE MYELOID CELLS VIA SMALL MOLECULE IMMUNOMODULATORS

by

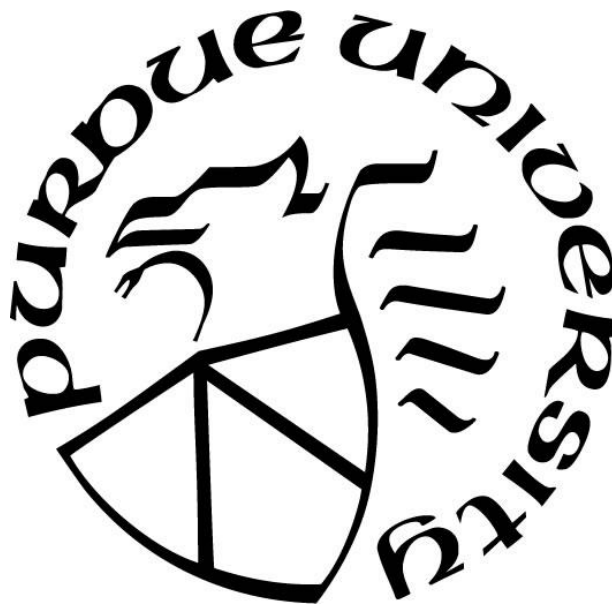
**Erin Michelle Kischuk**

**A Dissertation**

*Submitted to the Faculty of Purdue University*

*In Partial Fulfillment of the Requirements for the degree of*

**Doctor of Philosophy**



Department of Comparative Pathobiology

West Lafayette, Indiana

December 2019

**THE PURDUE UNIVERSITY GRADUATE SCHOOL**  
**STATEMENT OF COMMITTEE APPROVAL**

Dr. Timothy L. Ratliff, Chair

Department of Comparative Pathobiology

Dr. Gaurav Chopra

Department of Chemistry

Dr. Deborah W. Knapp

Department of Veterinary Clinical Sciences

Dr. David H. Thompson

Department of Chemistry

**Approved by:**

Dr. Jason R. Cannon

Head of the Graduate Program

*For my family.*

## TABLE OF CONTENTS

LIST OF TABLES .....	7
LIST OF FIGURES .....	8
ABSTRACT .....	10
CHAPTER 1. INTRODUCTION AND LITERATURE REVIEW .....	11
1.1 The Tumor Microenvironment.....	11
1.1.1 Structure and Composition of the Tumor Microenvironment.....	11
1.1.2 Immunity in the Tumor Microenvironment .....	12
1.2 Immunosuppressive Myeloid Cells .....	14
1.2.1 Myeloid-derived Suppressor Cells .....	15
1.2.2 Tumor-associated Macrophages .....	16
1.2.3 Cancer-mediated Induction of MDSC and TAM .....	17
1.3 Immunotherapy Strategies for Suppressive Myeloid Cells in Cancer .....	17
1.3.1 MDSC-targeted Immunotherapy .....	18
1.3.2 TAM-targeted Immunotherapy .....	19
1.4 Nitric Oxide in the Tumor Microenvironment.....	22
1.5 Introduction to Research Problems, Hypotheses, and Methodology .....	23
1.6 Purpose of Studies .....	24
CHAPTER 2. RESEARCH METHODOLOGY .....	25
2.1 Common Methods .....	25
2.1.1 Mice .....	25
2.1.2 Cell Culture .....	25
2.1.3 Tumor models.....	25
2.1.4 Flow Cytometry .....	26
2.1.5 Statistical Analysis.....	26
CHAPTER 3. FOLATE-TARGETED PHOTODYNAMIC THERAPY ABLATES MDSC FROM INFLAMED TISSUE AND INDUCES TUMOR REGRESSION IN A MOUSE MODEL .....	27
3.1 Introduction.....	27
3.2 Methods .....	28
3.2.1 Mice .....	28

3.2.1 Folate-targeted compounds .....	28
3.2.2 BCG infection model .....	28
3.2.3 OTL38 labeling experiments.....	28
3.2.4 Photodynamic therapy .....	29
3.2.5 Imaging .....	29
3.2.6 Tissue harvest and preparation for FACS .....	29
3.3 Results .....	30
3.4 Discussion .....	32
CHAPTER 4. <i>IN VIVO</i> TREATMENT WITH GCL2, A NUCLEAR HORMONE RECEPTOR MODULATOR, REDUCES TUMOR GROWTH AND MDSC INFILTRATION .....	43
4.1 Introduction.....	43
4.2 Methods .....	43
4.2.1 Mice .....	43
4.2.2 Imaging .....	44
4.2.3 Drug treatment.....	44
4.2.4 Tissue harvest .....	45
4.2.5 Organ histology .....	45
4.2.5 T cell stimulation .....	45
4.3 Results .....	45
4.4 Discussion .....	47
CHAPTER 5. DEVELOPMENT OF A MACHINE LEARNING APPROACH TO IDENTIFY NOVEL CELL-SPECIFIC IMMUNOMODULATORS OF SUPPRESSIVE MYELOID CELLS IN THE TME.....	60
5.1 Introduction.....	60
5.2 Methods .....	62
5.2.1 Mouse models and cell isolation .....	62
5.2.2 OT-I cell activation.....	63
5.2.3 MACS enrichment of Ly6C <sup>+</sup> Ly6G <sup>neg</sup> cells.....	63
5.2.4 <i>Ex vivo</i> compound treatments.....	63
5.2.5 Griess assay .....	64
5.2.6 Gene expression.....	64

5.2.7 <i>In vivo</i> drug treatments.....	64
5.2.8 T cell suppression assay .....	65
5.3 Results .....	65
5.4 Discussion.....	69
CHAPTER 6. SUMMARY AND FUTURE DIRECTIONS .....	92
REFERENCES .....	95

## LIST OF TABLES

Table 5.1 Compounds tested in Rounds 0 – 3 .....	83
Table 5.2 JMGC02S interaction targets excluded from Reactome enrichment analysis .....	84
Table 5.3 JMGC02S interaction targets included in Reactome enrichment analysis .....	85
Table 5.4 Top 5 significantly enriched pathways .....	86
Table 5.5: Significantly differentially expressed proteins.....	87
Table 5.6 Proteins appearing only in vehicle- or compound-treated samples.....	89
Table 5.7 Proteins contained in sets of predicted and detected targets .....	90

## LIST OF FIGURES

Figure 3.1 FACS gating strategy and photodynamic therapy in a BCG infection model.....	35
Figure 3.2 FACS gating strategy and photodynamic therapy in a tumor model .....	36
Figure 3.3 Intradermal BCG recruit FR $\beta$ -expressing MDSC subsets to the infection site .....	37
Figure 3.4 Folate-targeted PDT reduces the viability of G-MDSC at the site of BCG infection..	38
Figure 3.5 Tumors recruit FR $\beta$ -expressing myeloid cells and accumulate a folate-targeted photosensitizer.....	39
Figure 3.6 Folate-targeted PDT rapidly depletes FR $\beta$ -expressing MDSC from the tumor .....	40
Figure 3.7 Folate-targeted PDT transiently depletes myeloid cells from MB49-Luc tumors.....	41
Figure 3.8 Folate-targeted PDT slows tumor growth and improves survival .....	42
Figure 4.1 In vivo imaging and GCL.2 treatments .....	50
Figure 4.2 FACS gating strategy of T cells in the peritoneal MB49-Luc tumor model .....	51
Figure 4.3 Liver and spleen weight increases in healthy and tumor-bearing mice treated with GCL.2 .....	52
Figure 4.4 GCL.2 slows the rate of early tumor growth <i>in vivo</i> .....	53
Figure 4.5 GCL.2 administered by IP injection route does not impact tumor growth but does alter immune cell frequencies .....	54
Figure 4.6 GCL.2 increases liver and spleen weight and induces mild histological changes .....	56
Figure 4.7 GCL.2 administered by oral gavage route slows tumor growth and reduces primary tumor weight .....	57
Figure 4.8 Bioluminescence in the primary tumor location correlates with tumor weight.....	58
Figure 4.9 GCL.2 treatment increases the frequency of IFN $\gamma$ <sup>+</sup> T cells in the primary tumor and reduces the frequency of MDSC in the tumor ascites .....	59
Figure 5.1 <i>Ex vivo</i> compound treatment assays.....	72
Figure 5.2 <i>In vivo</i> treatments with JMGC02S81 .....	73
Figure 5.3 Diagram of experiments with compounds.....	74



Figure 5.4 Round 0 predictions exhibit minimal activity against the NO production pathway ....	75
Figure 5.5 The accuracy of machine learning predictions for compounds that modulate the NO production pathway improves with iteration .....	76
Figure 5.6 Activity defined by single observations during screening is reproducible during the validation phase .....	77
Figure 5.7 Preliminary dose-response shows compound concentration used for screening and validation phases is neither minimal nor maximal .....	78
Figure 5.8 Activity defined by single observations during screening is less robust for female-derived cells .....	79
Figure 5.9 Short-term treatment with JMGC02S81 is non-toxic <i>in vivo</i> and reduces the suppressive capacity of tumor-derived Ly6C <sup>+</sup> Ly6G <sup>neg</sup> cells .....	80
Figure 5.10 Short-term treatment with JMGC02S81 in a model of benign inflammation alters the expression of activation markers on tissue-infiltrating CD8 <sup>+</sup> T cells.....	82

## ABSTRACT

Author: Kischuk, Erin, M. PhD

Institution: Purdue University

Degree Received: December 2019

Title: Targeting of Suppressive Myeloid Cells via Small Molecule Immunomodulators

Committee Chair: Timothy Ratliff

Suppressive myeloid cells including myeloid-derived suppressor cells (MDSC) and tumor-associated macrophages (TAM), are a significant barrier to cancer immunotherapy. These cells enhance tumor growth and metastasis and promote immune escape by suppressing the anti-tumor T cell response. One of the key mechanisms of suppression is the production of nitric oxide (NO) via iNOS which leads to the modification and inactivation of various proteins involved in T cell effector function. Previous efforts to control suppressive myeloid cells have included direct elimination, blockade of accumulation or function at the tumor site, and conversion to an anti-tumor phenotype. Unfortunately, though several strategies have been tested in preclinical models and in clinical trials, there are currently no approved and effective therapies that are selective for these cells. The discovery of new drugs for these cells is hampered by the limited availability of primary cells for screening. The studies herein describe efforts to develop effective immunotherapies that target suppressive myeloid cells more specifically. Using a specific receptor, FR $\beta$ , combined with photodynamic therapy we were able to deplete MDSC and TAM from solid tumors. This strategy limits the cytotoxic effects to the target cells within the tumor site. We also pursued a strategy of targeting accumulation and/or suppressive function via testing of GCL.2, a compound expected to reduce the accumulation of MDSC at the tumor site. Finally, we targeted the NO production pathway using synthetic small molecules. Importantly, we did not target iNOS directly but utilized a computer-based model that analyzed the interactions of compounds with a large set of putatively overexpressed targets in suppressive MDSC. Experimental data was integrated into the model to refine additional selections. With this approach, we were able to identify several hit compounds and verified the immunomodulatory activity of one compound *in vivo*. These studies demonstrate that targeting the suppressive phenotype is a viable approach to cancer immunotherapy, and we have also validated a novel approach to drug discovery for suppressive myeloid cells.

## CHAPTER 1. INTRODUCTION AND LITERATURE REVIEW

### 1.1 The Tumor Microenvironment

The malignant cells of the tumor are inseparable from the tumor microenvironment (TME), and in recent years cancer therapy has increasingly focused on the TME as well as the tumor. Cancer immunotherapy targeting the TME was hailed as the breakthrough of the year by *Science* in 2013; however, immunotherapy is still not the hoped-for silver bullet in the oncology clinic.<sup>1</sup> The generally immunosuppressive nature of the TME plays a key role in limiting the success of cancer immunotherapy. The TME, which supports and protects the malignant cells, is defined as the non-malignant cells and structures of the tumor including vasculature, extracellular matrix (ECM), and stromal cells such as fibroblasts and immune cells. An appreciation of the masterful tumor-mediated design and manipulation of the TME is necessary in order to develop efficacious therapies that will ameliorate its pro-tumor activity.

#### 1.1.1 Structure and Composition of the Tumor Microenvironment

The vasculature is a pivotal feature of the TME. Tumor growth is severely limited without a network of blood vessels to supply nutrients and remove metabolic waste, and the vasculature underlies the development of the rest of the TME<sup>2,3</sup>. Transformed cells acquire the capacity to drive angiogenesis very early by secreting pro-angiogenic factors that exert mitogenic effects on endothelial cells.<sup>2,4,5</sup> Indeed, vascular endothelial growth factor (VEGF) is directly implicated in supporting tumor growth *in vivo*.<sup>6</sup> VEGF and other tumor-derived pro-angiogenic factors can induce endothelial anergy—failure to upregulate adhesion molecules in response to inflammation—in the tumor vasculature.<sup>7,8</sup> This serves to protect the tumor through impairing infiltration by cytotoxic lymphocytes (CTLs). A well-developed tumor vasculature has also been shown to enable metastasis through simple access to circulation as well as specific permissiveness of transendothelial migration by tumor cells.<sup>9,10</sup> The importance of angiogenesis in cancer is underscored by observations that combination with antiangiogenic agents can improve the efficacy of immunotherapy.<sup>11,12</sup>

In addition to being malformed and dysfunctional, tumor blood vessels are hyperpermeable, and this initiates deposition and subsequent remodeling of the tumor ECM by fibroblasts.<sup>13,14</sup> Tumor ECM—composed of collagen and fibronectin as well as molecules not typically found in connective tissue like tenascin-C—is often dense and stiff, serving to further enhance the malignant phenotype of the tumor cells.<sup>15–17</sup> Importantly, the dense nature of the ECM can limit delivery of small and macromolecule therapeutics to the tumor by slowing diffusion or by molecular exclusion due to high interstitial fluid pressure<sup>18</sup>. Collagen-dense stroma impedes T cell migration and correlates with poorer clinical outcomes.<sup>19</sup> Tumors orchestrate this sculpting of the ECM by producing factors, chiefly transforming growth factor beta (TGF $\beta$ ) and interleukin (IL)-

6, that activate cancer-associated fibroblasts (CAFs).<sup>20–23</sup> Activated CAFs exhibit a myofibroblast-like phenotype characterized by increased collagen synthesis as well as secretion of tumor-promoting growth factors, matrix metalloproteinases (MMPs) that drive invasion, and chemokines that recruit pro-tumor myeloid cells.<sup>20,24</sup> Thus, CAFs serve an integral role in shaping and maintaining the TME, but anti-CAF monotherapy is insufficient for tumor regression and should be paired with additional immunotherapy.<sup>25–27</sup>

In addition to initiating angiogenesis and ECM deposition, the tumor also attracts and reprograms infiltrating leukocytes to meet its needs. In response to TNF $\alpha$ , which can be secreted by the tumor, neutrophils produce MMP-9 to aid in tumor angiogenesis and invasion.<sup>28–31</sup> VEGF, secreted by tumor cells and CAFs, attracts monocytes and macrophages. VEGF also induces the anti-inflammatory M2 macrophage phenotype often associated with poorly tumoricidal tumor-associated macrophages (TAM).<sup>32–35</sup> Tumors also recruit monocytes via CC motif chemokine ligand (CCL) 2 and colony-stimulating factor (CSF)-1 and subsequently co-opt the wound-healing activities of differentiated M2 macrophages to support further angiogenesis as well as metastasis.<sup>36–38</sup> An additional CCL2-mediated influx of immature myeloid cells called myeloid-derived suppressor cells (MDSC) is associated with enhanced tumor growth and angiogenesis through MMP-9 production as well as resistance to anti-angiogenic therapy and metastasis.<sup>39–41</sup> Importantly, both TAM and MDSC are known to potently inhibit anti-tumor T cell activity through a variety of mechanisms.<sup>42,43</sup>

### 1.1.2 Immunity in the Tumor Microenvironment

The formation of tumor vasculature is an excellent example of how the tumor can efficiently alter the environment to meet its needs. The array of coordinated changes made to the TME to promote ongoing angiogenesis belies any suggestion that tumors are disorganized. Moreover, the redundancy of pro-angiogenic and pro-tumor functions among the various elements of the TME can make therapy less effective. In addition to ensuring its own survival through angiogenesis the tumor also enforces an immunosuppressive environment. The tumor immune microenvironment has recently gained traction as an important variable in clinical outcome for patients receiving immune checkpoint blockade (ICB) therapy. This has led to the classification of immunologically “hot” tumors that are infiltrated by immune cells, including activated CTLs, and the “cold” counterparts which are infiltrated by immune cells but feature only poorly activated CTLs restricted to the tumor periphery.<sup>44</sup> Li *et al* elaborated a potential mechanism to explain high and low T cell infiltration using pancreatic tumor clones derived from a single parental line.<sup>45</sup> Dendritic cells in the tumor are responsible for the increased T cell recruitment, but this effect is overwhelmed by tumor-derived CXC motif ligand (CXCL) 1 which biases the immune infiltrate toward other myeloid cells like MDSC, thereby reducing T cell recruitment. Granulocyte (G)-CSF also has a minor role in this process. Interestingly, higher T cell infiltration and responsiveness to therapy correspond with activation of T cells as indicated by higher expression of markers such as programmed death receptor-1 (PD-1), lymphocyte activating 3 (LAG3), T cell immunoglobulin

and mucin-domain containing-3 (TIM3), and cytotoxic T lymphocyte antigen-4 (CTLA-4).<sup>45</sup> Given “hot” tumors tend to respond well to ICB therapy it is hypothesized that converting “cold” tumors to a “hot” phenotype may rescue the responsiveness to therapy.<sup>46,47</sup> However, effector function—proliferation as well as expression of granzyme B and interferon gamma (IFN $\gamma$ )—is not different between high and low T cell tumors, supporting the notion that overcoming the barrier to infiltration is only part of the battle.<sup>45</sup>

Inflammation is now considered to be an “enabling characteristic” of cancer. Chronic inflammation is responsible for the accumulation in tumors of immune regulatory cells such as MDSC and TAM that suppress the anti-tumor immune response.<sup>48</sup> Early evidence that tumors can induce a suppressive phenotype came from studies showing phagocytic cells from spleens of tumor-bearing but not normal mice severely suppress mitogenic responses of T cells.<sup>49</sup> Later, it was shown that tumor lysate-derived factors can induce the suppressive phenotype.<sup>50</sup> This suppression is reversible via resection of the tumor.<sup>51</sup> It was further shown in the mouse Lewis lung carcinoma model that tumors can induce the expansion of suppressor cells in the bone marrow via a soluble factor.<sup>52</sup> Various tumor-associated factors—such as transforming growth factor beta (TGF $\beta$ ), granulocyte-macrophage colony-stimulating factor (GM-CSF), CCL2, and prostaglandin E2 (PGE<sub>2</sub>)—have now been implicated in the expansion and recruitment of immune-suppressive populations, and thus modulation of these factors is considered a potential avenue of cancer therapy.<sup>53</sup> TGF $\beta$  polarizes macrophages to the anti-inflammatory M2 phenotype and potently suppresses CD8+ T cell proliferation and effector functions.<sup>54,55</sup> It is associated with the “cold” tumor phenotype in clinical bladder cancer samples, and antibody blockade of TGF $\beta$  signaling in tumor-bearing mice reverses T cell exclusion from tumors while reducing the MDSC population.<sup>56,57</sup> GM-CSF-secreting tumor cell vaccines have been explored clinically with mixed results, possibly because low doses of GM-CSF are immunostimulatory while higher systemic levels, such as those secreted by a tumor, increase the frequency of suppressive MDSC.<sup>58–61</sup> In mice, GM-CSF-secreting tumors become resistant to ICB therapy in association with the increased presence of suppressive myeloid cells. Sensitivity to ICB therapy is restored following inhibition of phosphoinositide 3-kinase (PI3K), a downstream effector of the GM-CSF receptor that potentiates the suppressive phenotype.<sup>62,63</sup> CCL2 is a potent factor in the recruitment of MDSC, TAM, and regulatory T cells (Treg) to the tumor.<sup>64,65</sup> Overproduction of PGE<sub>2</sub>, an inflammatory molecule, is implicated in lack of T cell responsiveness in head and neck cancer patients; this may be attributed to its ability to expand the MDSC population.<sup>66,67</sup>

The characterization of immune checkpoints such as programmed death ligand 1 (PD-L1) has driven more recent initiatives in immunotherapy. PD-1 is expressed by activated T cells and is similar to CTLA-4, another receptor with T cell-inhibitory properties. PD-L1 is a member of the B7 protein family along with the ligands for CTLA-4. It was first identified as an inducible surface ligand on monocytes following inflammatory stimulation such as IFN- $\gamma$ , and its engagement with PD-1 on T cells impairs proliferation and cytokine production.<sup>68</sup> Subsequently, endothelial cells as well as tumor cells were also found to express PD-L1, suggesting an additional mechanism by

which T cells are suppressed in the TME.<sup>69,70</sup> Moreover, T cell sensitivity to PD-L1 is increased when IL-2 levels are low, one of the first signs of T cell exhaustion as frequently occurs in the TME.<sup>71–73</sup> Increased PD-L1 expression by tumor cells is a negative prognostic indicator in several malignancies.<sup>74–77</sup> Blockade of PD-L1 or deletion of PD-1 in mice is sufficient to slow or completely block myeloma growth, highlighting the potential of anti-PD-L1/PD-1 therapy.<sup>78</sup> The FDA has approved anti-PD-L1/PD-1 therapy for malignancies including urothelial carcinoma, gastric cancer, colorectal cancer, non-small cell lung carcinoma, and melanoma.<sup>79</sup> However, the overall response rates to this ICB therapy remain dismally low at less than 30 percent, and its efficacy is correlated with tumor expression of PD-L1.<sup>80</sup> A key population involved in the failure of ICB therapy is MDSC; higher frequency of MDSC in circulation is predictive of decreased ICB efficacy, and TAM are also being recognized as an attractive target.<sup>81,82</sup> Both MDSC and M2 macrophages express PD-L1; however, PD-L1 blockade does not entirely abrogate MDSC suppressive function.<sup>83,84</sup> Therefore, it is necessary to combine ICB with therapies that target MDSC and TAM, and efforts are underway to identify viable strategies. In mice, blockade of CXCR2 to impair MDSC recruitment in concert with anti-PD-1 slowed tumor growth and enhanced survival.<sup>85</sup> The combination of a tyrosine kinase inhibitor and a toll-like receptor (TLR)-7/8 agonist with anti-PD-L1 reduces both MDSC and TAM, resulting in improved anti-tumor CD8<sup>+</sup> T cell responses and slowed tumor growth<sup>86</sup>. Inhibition of PI3K or Class IIa HDACs converts macrophages to an anti-tumor phenotype and enhances the efficacy of anti-PD-1 therapy.<sup>62,87</sup> In each case, the combination therapy is superior to monotherapy, reinforcing the importance of a multifaceted approach to address immunosuppressive elements, particularly myeloid cells, in the TME.

## 1.2 Immunosuppressive Myeloid Cells

Study of immune suppressor cells in the context of cancer began in earnest in the 1970s with the identification of an adherent and phagocytic spleen-derived population in tumor-bearing mice that could depress T cell responses to mitogens.<sup>49</sup> The presence of these cells corresponded with an inability to control tumor growth in mice, and circulating monocytes were also implicated in suppression of T cell responses in cancer patients.<sup>88–90</sup> These cells were not restricted to tumor-bearing hosts; they were also found in the spleens and bone marrow of mice following systemic administration of Bacillus Calmette-Guerin and in mice with graft-versus-host disease.<sup>91,92</sup> Further characterization of these cells revealed the absence of surface markers for lymphocytes or macrophages, making them similar to natural killer (NK) cells though they lacked the cytotoxic functions. This inspired the name “natural suppressor (NS) cells”.<sup>93</sup> Eventually, murine NS cells were found to be Sca-1<sup>+</sup> Mac1<sup>+</sup>, and their suppressive activity, mediated mainly by TGFβ, seemed to require IFN-γ stimulation, suggesting a link between inflammatory stimulus and subsequent anti-inflammatory activity.<sup>92,94,95</sup> The human counterparts to murine NS cells express CD34 and correlate with increased risk of recurrence or metastasis in head and neck squamous cell carcinoma patients.<sup>96,97</sup>

### 1.2.1 Myeloid-derived Suppressor Cells

MDSC are most frequently studied using mouse models due in large part to the ease of manipulation and ability to study both tumor tissue and lymphoid organs. The generally accepted surface markers of murine MDSC are the common myeloid markers CD11b and GR-1, and this inspired the name myeloid or myeloid-derived suppressor cells.<sup>61</sup> GR-1 can be separated into the epitopes Ly6G and Ly6C, and their differential expression within the population of immature myeloid cells gives rise to two functionally and morphologically distinct subsets. The monocyte-like M-MDSC are Ly6C<sup>high</sup> Ly6G<sup>neg</sup> and the granulocyte-like G-MDSC are Ly6C<sup>+</sup> Ly6G<sup>high</sup>.<sup>98</sup> However, the populations described by these markers also contain mature neutrophils, and monocytes as well as MDSC, making it difficult to obtain samples of uniform composition to study MDSC biology. The immaturity of MDSC is exemplified by observations that they will differentiate to mature macrophages or dendritic cells in culture.<sup>99</sup> In part due to the lack of specific markers MDSC are defined functionally by their capacity to suppress the activity of T cells, B cells, and NK cells.<sup>100–103</sup> The two MDSC subsets rely on distinct mechanisms for their suppressive function. M-MDSC primarily utilize nitric oxide (NO) production via inducible nitric oxide synthase (iNOS) while G-MDSC activity is NO-independent and partially derived from Arginase 1 (ARG1) activity.<sup>98</sup> Human equivalents of the murine MDSC subsets are defined as CD33<sup>+</sup>CD14<sup>+</sup>HLA-DR<sup>-/low</sup>CD15<sup>-</sup> (M-MDSC) and CD33<sup>low</sup>CD14<sup>-</sup>CD15<sup>+</sup> (G-MDSC). As in mice, human MDSC marker sets also identify monocytes and neutrophils, respectively, which cannot currently be distinguished from MDSC except via functional assays.<sup>104,105</sup>

MDSC functional activity against CD8<sup>+</sup> T cells and in support of tumor growth has been ascribed to several mediators, including NO, reactive oxygen species (ROS), reactive nitrogen species (RNS), and IL-10.<sup>105</sup> More recently, ARG1 has been controversial in its importance to MDSC function.<sup>106</sup> In the case of NO, ROS, and RNS, T cell functions are modulated via downregulation of the CD3 $\zeta$  chain under oxidative stress, nitration of the TCR rendering it incapable of recognizing antigen, and nitration of lymphocyte-specific protein tyrosine kinase (LCK) in T cells leading to reduced IL-2 production.<sup>107–109</sup> These mechanisms all require cell-cell contact between MDSC and T cells, and while T cell suppression was initially believed to be antigen-independent an antigen-dependent mode of suppression has also been described.<sup>98,110</sup> By producing IL-10, MDSC can subvert the anti-tumor M1 macrophage phenotype to a pro-tumor M2 program and also recruit regulatory CD4<sup>+</sup> T cells (Treg) in an arthritis model.<sup>111,112</sup>

The mechanistic study of MDSC function is ongoing in the search for novel immunotherapies, but these efforts are hampered in part by inconsistencies stemming from the anatomical site from which MDSC are obtained. In mice, CD11b<sup>+</sup> GR1<sup>+</sup> cells can be isolated from the tumor or inflammatory site as well as from primary and secondary lymphoid organs.<sup>113</sup> In the study of cancer, murine MDSC are frequently isolated from the spleen while human MDSC are often obtained from peripheral blood. This choice is at least partly due to the relative scarcity of MDSC in tumor tissue as well as availability of clinical samples and the resulting difficulty of obtaining a sufficient quantity of cells for study.<sup>114–116</sup> However, only MDSC from the diseased tissue are

capable of suppressing T cells immediately upon isolation while peripheral MDSC require activation by inflammatory signals in order to exert suppressive function.<sup>117,118</sup> The complexity of the *in vivo* inflammatory microenvironment cannot be perfectly recapitulated *ex vivo*, making it likely that some aspects of MDSC biology are not captured by the substitution of peripheral MDSC for those from the affected tissue. Additionally, tumors of different tissues exhibit heterogeneity concerning the types and frequencies of recruited MDSC.<sup>118,119</sup> The lack of a single definitive marker set identifying MDSC in mice and humans as well as functional heterogeneity make therapeutic intervention a nontrivial pursuit.

## 1.2.2 Tumor-associated Macrophages

Tumor-associated macrophages (TAM), a population related to and potentially derived from MDSC, are associated with poor prognosis in a variety of cancers.<sup>120,121</sup> TAM are one of the most abundant cells in the tumor mass and frequently display a pro-tumor phenotype similar to the alternatively-activated or M2 macrophage.<sup>122</sup> An important aspect of tumor biology lies in the macrophage repolarization that occurs in the TME. Initially, tumor-infiltrating macrophages may display an M1-like phenotype induced by local factors such as TNF $\alpha$ . This leads to cytotoxicity mediated by production of nitric oxide via iNOS. As the tumor progresses, a conversion to M2-like programming has been observed. The influence of tumor-derived cytokines such as IL-10, TGF $\beta$ , and PGE<sub>2</sub>, along with exposure to apoptotic tumor cells, have been proposed as potential mechanisms for this change.<sup>123</sup> There is also evidence that a feedback loop exists in which high levels of NO can inhibit the M1 phenotype.<sup>124</sup> In mice, the TAM compartment contains cells that are CD11b<sup>+</sup> Ly6C<sup>low/int</sup> F4/80<sup>+</sup> MHCII<sup>low/high</sup> with the MHCII<sup>low</sup> subset segregating to a more M2-like phenotype and correlating with tumor hypoxia.<sup>125,126</sup> The core markers for human TAM include CD11b, HLA-DR, and CD14 (shared with monocytes).<sup>127</sup> Importantly, a strict M1 versus M2 polarization model was once believed to exist in the tumors of mice and humans but has given way to the notion that TAM exist along a spectrum of polarizations associated with specialized roles in the tumor.<sup>128,129</sup>

Like MDSC, TAM employ a number of mechanisms in their tumor-promoting function. TAM are frequently polarized toward a pro-tumor M2-like phenotype. This skewed activation has been linked to defective NF- $\kappa$ B signaling due to overexpression of the inhibitor p50, leading to an inability to express pro-inflammatory cytokines such as IL-12.<sup>130,131</sup> Loss of TNF $\alpha$  signaling in macrophages allows expression of molecules associated with the M2 phenotype in a STAT6-dependent manner.<sup>132</sup> Accordingly, TAM can suppress T cell proliferation via an ARG1- and NO-dependent mechanism.<sup>133</sup> This clearly signifies an exception to the usual association of iNOS and nitric oxide production with macrophage cytotoxicity. PD-L1 expression is also induced in TAM by tumor cells and, as with MDSC, is associated with hypoxia.<sup>134,135</sup> By secreting IL-10, TAM can induce the differentiation of Treg, and secretion of CCL20 further promotes the migration of Treg to the tumor.<sup>136,137</sup> Additionally, VEGF<sup>+</sup> TAM accumulate in poorly vascularized regions of breast



tumors and have been shown to secrete CCL18 and VEGF to promote tumor angiogenesis, aiding both in tumor growth and in recurrence after chemotherapy.<sup>138–140</sup>

### 1.2.3 Cancer-mediated Induction of MDSC and TAM

As with some aspects of their function, the origins of MDSC and TAM are interrelated. The influx of these cells in the tumor site results from a large increase in myelopoiesis in the bone marrow, trafficking to the tumor, and induction of the effector phenotype. In the case of MDSC, tumor-derived GM-CSF has been implicated in the differentiation of CD11b<sup>+</sup>GR-1<sup>+</sup> cells from common myeloid precursors in the bone marrow.<sup>141,142</sup> Ordinarily, these cells differentiate into mature granulocytes, dendritic cells, and macrophages, but in cancer this process is pathologically inhibited and driven toward an immature immunosuppressive phenotype. Factors implicated in MDSC expansion and activation include STAT3 activation, IRF8 signaling, NF-κB activation, and the COX2/PGE<sub>2</sub> pathway among others.<sup>143</sup> Two major pathways involved in MDSC trafficking to the tumor are mediated by CCL2/CCR2 and CCR5.<sup>144–146</sup>

The appearance of TAM in the tumor is proposed to occur through at least three distinct processes. Like MDSC, the first process is CCL2-dependent and involves the sustained influx of Ly6C<sup>+</sup>CCR2<sup>+</sup> circulating monocytes into the tumor site.<sup>147</sup> Both CSF1 and VEGF have also been demonstrated to have chemoattractant properties for macrophages without affect their polarization.<sup>148,149</sup> Although some tissue macrophages have fetal origins, it appears that most of the TAM population, whether tissue-resident or newly-recruited, originates from circulating bone marrow-derived monocytes that proliferate locally to maintain the pool.<sup>150</sup> Newly-arrived monocytes differentiate into TAM in a manner dependent on RBP-J, a negative regulator of Notch signaling, and gain the capacity to suppress T cells.<sup>147,151</sup> However, evidence for TAM of embryonic origin was recently reported in a pancreatic cancer model in which fetally-derived TAM proliferate locally and exhibit distinct tumor-promoting activities from monocyte-derived TAM.<sup>152</sup> The third mechanism for accumulation of TAM in the tumor is via differentiation from MDSC. Tumor hypoxia was shown to drive increased expression of CD45 and subsequent phosphatase activity that reduces the activity of STAT3, thereby allowing differentiation of MDSC to TAM.<sup>153</sup> An additional regulatory role in MDSC-to-TAM differentiation has been demonstrated for SIRT1, a regulator of glycolysis, in a mechanism that also involves mTOR and HIF1α activation.<sup>154</sup> Importantly, not all TAM are immune-suppressive as demonstrated by the differentiation of MDSC into M1-like TAM via TLR7 activation.<sup>155</sup>

## 1.3 Immunotherapy Strategies for Suppressive Myeloid Cells in Cancer

The pervasiveness of suppressive myeloid cells in the TME and their hampering effect on cancer immunotherapy makes them an attractive and important therapeutic target. For both MDSC and TAM, there are three key approaches to abolishing their tumor-promoting activities: 1) reduce the number and/or trafficking of cells, 2) prevent activation of the suppressive phenotype or convert

to an anti-tumor phenotype, and 3) inhibit the suppressive functions. At present, there are no FDA-approved therapeutics specifically for MDSC or TAM. This is due in part to incomplete understanding of their biology and a lack of specific targets. However, several strategies utilized in direct cancer therapy have secondary efficacy against MDSC and TAM.

### 1.3.1 MDSC-targeted Immunotherapy

VEGF has been shown to regulate the expansion and maturation of several types of myeloid cells.<sup>53</sup> Sunitinib, an inhibitor of VEGF and c-kit signaling, has also been shown to reduce the frequency of MDSC in renal cell carcinoma patients with an associated decrease in Treg numbers and an improvement in IFN $\gamma$  production by CD8<sup>+</sup> T cells.<sup>156</sup> However, high levels of GM-CSF can abrogate the effects of sunitinib on MDSC.<sup>157</sup> Certain cytotoxic drugs can preferentially impact MDSC while sparing other immune cell populations. In tumor-bearing mice, gemcitabine reduces the total number of splenic MDSC, leading to enhanced anti-tumor activity of CD8<sup>+</sup> T cells and NK cells.<sup>158</sup> In pancreatic cancer patients, gemcitabine treatment reduces G-MDSC numbers but does not affect M-MDSC. Interestingly, shorter survival times correlate with higher numbers of M-MDSC, suggesting that gemcitabine may be a more appropriate therapeutic in tumors where the G-MDSC predominate.<sup>159</sup> The thymidylate synthase inhibitor 5-fluorouracil (5-FU) induces apoptosis in MDSC at doses below the threshold for anti-tumor effect. This is ascribed to low expression of thymidylate synthase in MDSC which increases their sensitivity to the drug.<sup>160</sup> Unfortunately, the anti-tumor effects of these drugs are transient as the pool of MDSC is constantly replenished by the bone marrow. Antibody-mediated depletion of MDSC has also been explored in animal models and in the clinic. Anti-GR-1 therapy in tumor-bearing mice produces profound reductions in tumor burden accompanied by decreased markers of angiogenesis and increased cytotoxic function in CD8<sup>+</sup> T cells and NK cells.<sup>161</sup> More recently, Qin *et al* reported that an Fc-fusion protein—termed “peptibody”—can deplete both MDSC subsets in contrast to the G-MDSC biased depletion of anti-GR-1. The putative target of this peptibody is in the S100 family of proteins which are known to regulate the accumulation of MDSC.<sup>162,163</sup> CSF-1 is involved in MDSC trafficking to the tumor and is particularly induced as part of the DNA damage response to radiotherapy in mice and humans.<sup>164</sup> Inhibiting CSF1R signaling in a mouse model of prostate cancer leads to decreased tumor growth in irradiated mice associated with a reduction in tumor-associated MDSC as well as TAM.<sup>165</sup> Interestingly, CSF1R inhibition in a mouse model of melanoma has failed to show any effect on MDSC due to low initial infiltration, suggesting that MDSC-targeting therapies need to be tailored to the unique features of the tumor in question. On the other hand, the phenotype of TAM shifts to M1-like and there is an increase in functional CD8<sup>+</sup> T cells in the tumor.<sup>166</sup> CCL2 also plays a key role in MDSC recruitment in tumor-bearing mice and cancer patients.<sup>56,167,168</sup> However, blockade of CCL2/CCR2 does not always result in decreased numbers of MDSC, and results from clinical trials in cancer therapy have been disappointing.<sup>169,170</sup>

All-trans retinoic acid (ATRA), a derivative of vitamin A, has been shown to drive maturation of MDSC into macrophages and dendritic cells by reducing ROS levels.<sup>171,172</sup> Treatment of lung cancer and renal cell carcinoma patients with ATRA decreases the frequency of circulating MDSC and improves T cell function.<sup>171,173</sup> A role in maturation of myeloid cells has also been demonstrated for Vitamin D<sub>3</sub>. Vitamin D<sub>3</sub> treatment of tumor-bearing mice reduces the frequency of suppressive myeloid cells by counteracting the activity of tumor-derived GM-CSF, leading to reduced tumor metastasis.<sup>174</sup> It has since been shown that treatment of MDSC precursors with D<sub>3</sub> inhibits activation of their suppressive function.<sup>175</sup>

A key mechanism in MDSC-mediated suppression is production of RNS and ROS via ARG1 and iNOS, making inhibition of these pathways a potential therapeutic target. Treatment of tumor-bearing mice with phosphodiesterase-5 inhibitors reduces expression and function of ARG1 and iNOS, resulting in decreased T cell suppression and slowed tumor growth. Similar effects have been observed following *ex vivo* treatment of circulating MDSC from cancer patients.<sup>176</sup> A class I HDAC inhibitor, entinostat, abrogates MDSC suppressive function in mice by reducing STAT3 activation, resulting in downregulation of ARG1, iNOS, and COX2. This leads to a reduction in tumor growth and enhanced anti-tumor T cell responses.<sup>177</sup> A small number of STAT3 inhibitors are currently in phase II clinical trials as single or combination therapy for malignancy. Nitroaspirins, a class of drugs that can donate nitric oxide molecules, have shown promise in mice by downregulating iNOS and ARG1 activity through a feedback inhibition mechanism.<sup>178</sup> Several nitroaspirins tested in tumor-bearing mice produce a decrease in MDSC function and an increase in tumor-specific CD8<sup>+</sup> T cells that augments DNA vaccine immunotherapy.<sup>179</sup> A newly reported avenue to target MDSC is via the folate receptor beta (FR $\beta$ ). MDSC at the site of inflammation upregulate FR $\beta$ , and the receptor is amenable to targeting by folate-linked small molecules, making it possible to deliver cargo ranging from imaging agents to cytotoxic molecules. (G. Cresswell *et al*, manuscript submitted)

### 1.3.2 TAM-targeted Immunotherapy

Strategies to therapeutically target TAM fall along the same lines as for MDSC though most strategies focus on reducing TAM accumulation and converting TAM from a pro-tumor to a tumoricidal phenotype. While there is some overlap due to the shared myeloid/monocyte lineage of M-MDSC and TAM there are some caveats to targeting TAM. Specifically, macrophages have an additional frontline role in innate immune functions during homeostasis whereas MDSC are only present in pathological conditions. More recently, modulating the frequency or function of myeloid cell populations is being considered in combination with immune checkpoint blockade as neither approach is sufficient by itself.

Bisphosphonates are an FDA-approved class of anti-cancer drugs that exert direct action against tumors as well as TAM by inducing apoptosis via mitochondrial dysfunction and by interfering in the mevalonate pathway that is vital to G protein signaling.<sup>180</sup> Zoledronate treatment reduces the

pro-angiogenic activities of TAM via inhibition of NF- $\kappa$ B activity and autocrine VEGF signaling, effectively repolarizing macrophages to a more M1-like phenotype.<sup>181</sup> On the other hand, clodronate-loaded liposomes are internalized by phagocytes and induce apoptosis in macrophages. Interestingly, both pro- and anti-tumor effects have been observed with the use of clodronate in tumor-bearing mice.<sup>180</sup> This observation may be due to the lack of selectivity for M1 versus M2-like TAM and consequent deletion of cells that may have anti-tumor functions, suggesting that a more nuanced approach to TAM than total depletion is necessary. Trabectin, which induces TRAIL-mediated apoptosis, has shown preferential efficacy against TAM compared to other immune cells in both mice and humans due to the increased expression of TRAIL receptors in TAM and versus non-signaling TRAIL decoy receptors in other immune cells. In mice, this results in anti-tumor activity mediated in part by reduced angiogenesis and decreased CCL2 production that corresponds with fewer mature intratumoral macrophages.<sup>182</sup> TAM can also be depleted via bacterial toxins. In one rodent model, a dramatic effect was demonstrated with an attenuated strain of *Shigella flexneri* in which specifically the tumor macrophage population was reduced by 74 percent following systemic infection. This resulted in complete tumor regression in mouse model of breast cancer that was attributed to a strong intratumoral inflammatory response following infection.<sup>183</sup> Given the risks of systemic infection with pathogenic organisms a targeted approach is more attractive. To that end, TAM were shown to express FR $\beta$  whereas macrophages in other tissues did not, so *Pseudomonas* toxin conjugated to an anti-FR $\beta$  antibody was used to deplete TAM and slow glioma growth.<sup>184</sup> As with MDSC, blockade of chemoattractant pathways, including CCL2/CCR2 and CSF1/CSF1R as well as CXCL12/CXCR4, has been considered for TAM. As mentioned earlier, although anti-CCL2/CCR2 therapy has shown promise in preclinical cancer models it has thus far been disappointing in clinical trials. Moreover, the therapeutic effects of CCL2/CCR2 blockade may be tumor type-specific as serum CCL2 levels and tumor macrophage infiltration were positively correlated with survival in pancreatic cancer patients.<sup>185</sup> A humanized anti-CSF-1 antibody, RG7155, induces apoptosis in macrophages *in vitro* and was subsequently shown to reduce the number of tumor-infiltrating macrophages in mice. Similar results were observed in a small cohort of patients with giant cell tumors or solid tumors in which a more favorable CD8<sup>+</sup>/CD4<sup>+</sup> ratio developed. Importantly, the effects of CSF1/CSF1R blockade are dependent on the level of pre-treatment macrophage infiltration, suggesting it is not appropriate for all patients.<sup>186</sup> The chemokine CXCL12 is involved in monocyte extravasation and TAM migration and is further implicated in inducing M2 programming.<sup>187,188</sup> CXCL12-mediated TAM migration toward tumor blood vessels has been implicated in metastasis, and the CXCR4 inhibitor CTCE-9908 reduces metastasis in mouse models of prostate and breast cancer.<sup>189,190</sup> Another inhibitor, AMD3100, is currently being evaluated in a phase I clinical trial for metastatic pancreatic and colorectal cancers and ovarian cancer.<sup>191</sup>

While depletion of TAM may reduce immunosuppression in the short term the constantly-renewing population limits the effectiveness of such strategies. Indeed, it is more advantageous to convert the pro-tumor population into tumoricidal TAM. One approach is to block initial differentiation to the M2 phenotype by interfering with STAT3 and STAT6 signaling. In a small

study of glioma patients, a small molecule STAT3 inhibitor promoted an anti-tumor macrophage and microglia phenotype while enhancing a pro-inflammatory cytokine milieu and boosting T cell proliferation.<sup>192</sup> Sunitinib, another STAT3 inhibitor, downregulates the pro-angiogenic phenotype of TAM and MDSC in a mouse model of renal cell carcinoma.<sup>193</sup> STAT6<sup>-/-</sup> mice can only produce TAM with an M1-like phenotype and are resistant to tumor metastasis. This effect is dependent on a defect in IL-4R signaling and requires production of nitric oxide, a molecule associated with tumoricidal macrophages.<sup>194</sup> A small molecule inhibitor of STAT6 activation reduces tumor angiogenesis along with the pro-angiogenic phenotype of TAM.<sup>195</sup> As yet, no STAT6 inhibitors have been evaluated for clinical use. Manipulating the PI3K $\gamma$ /AKT/PTEN pathway has shown promise as an immunotherapy as activation of the pathway promotes M2 polarization, including increased STAT3 activation, decreased production of pro-inflammatory cytokines, and increased ARG1 expression.<sup>196</sup> Rapamycin, an inhibitor of mTOR, has both anti-cancer and immunomodulatory properties. The anti-angiogenic action of rapamycin has been demonstrated to derive from a reduction in the frequency of IL-10-producing TAM in favor of IL-12 producing cells.<sup>197</sup> PI3K $\gamma$  activation in macrophages results in decreased NF- $\kappa$ B activation with a concomitant increase in CEBP/ $\beta$  activation which promotes the anti-inflammatory TAM phenotype. T cells from tumor-bearing mice are more cytotoxic in the absence of PI3K $\gamma$  signaling, and this effect is dependent on loss of signaling specifically in the macrophage compartment. Furthermore, PI3K $\gamma$  loss synergizes with anti-PD-1 immunotherapy to reduce tumor burden and induce immunological memory in animals experiencing complete tumor regression.<sup>62</sup>

Nutrient metabolism pathways have also been exploited to target TAM, including those for iron, vitamin D, and folic acid. An interesting difference between M1 and M2 macrophages is the bias toward iron uptake versus efflux, respectively.<sup>198</sup> Iron is important for cancer cell proliferation, so a mechanism to increase extracellular iron is consistent with the predominantly pro-tumor phenotype of TAM.<sup>199</sup> Macrophages activated with IL-10 *in vitro* and then treated with an iron chelator do not promote breast cancer cell proliferation or migration as effectively as those treated with IL-10 alone.<sup>198</sup> Treating an orthotopic mouse model of breast cancer with iron oxide nanoparticles drives M1 polarization and slows tumor growth. It further protects against the formation of liver and lung nodules in a lung cancer metastasis model.<sup>200</sup> Since the specific formulation in these studies, ferumoxytol (Feraheme), is already FDA-approved for treatment of iron-deficiency anemia these results provide support for a potential off-label use in cancer therapy. Another polarization-dependent difference in macrophages is in Vitamin D metabolism. Production of the defense peptide cathelicidin depends on vitamin D metabolism which is also reduced in TAM. Consequently, cathelicidin is produced at lower levels by M2 macrophages which reduces their tumoricidal capacity. Treating TAM with vitamin D<sub>3</sub> enhances cathelicidin production and tumor cell killing but does not actually shift the M2 phenotype toward an M1 program.<sup>201</sup> Finally, upregulation of folate receptor beta is induced by the M2-promoting growth factor CSF-1.<sup>202</sup> It has been observed for TAM in multiple solid tumors, and the presence of FR $\beta$ <sup>+</sup> TAM correlates positively with disease stage and lymph node metastasis, suggesting that FR $\beta$  is not only a targetable marker but also an indicator of disease aggressiveness.<sup>203</sup> Indeed, FR $\beta$

targeting of inflammatory macrophages with depletion-mediating monoclonal antibodies resolves rheumatoid arthritis in mice.<sup>204</sup> Currently, FR $\beta$  has been utilized chiefly to target imaging agents or cytotoxic molecules to TAM, but it is conceivable that phenotype-altering agents could also be specifically delivered to TAM in this manner.

### 1.4 Nitric Oxide in the Tumor Microenvironment

Nitric oxide plays a pivotal role in MDSC suppressive function and in the tumor-promoting activities of TAM; thus, NO and its production pathway can be appreciated as a potential target for immunotherapy. Nitric oxide (NO) is a highly reactive small molecule with important roles in normal biology, such as blood vessel dilation, as well as important implications for immune function, such as host defense against pathogens. There are three isoforms of nitric oxide synthase: endothelial (eNOS), neuronal (nNOS), and inducible (iNOS) with the first two being constitutively expressed in the descriptive tissues and the latter being restricted to immune cells in the absence of malignancy. Inflammatory cytokines such as IL-1 $\beta$ , TNF $\alpha$ , and IFN $\gamma$  upregulate *Nos2* (gene product: iNOS) via NF- $\kappa$ B, AP-1, C/EBP $\beta$ , and JAK/STAT. There is additional regulation at the mRNA level modulation of transcript stability and expression of iNOS-targeting microRNA. At the protein level, iNOS has a short half-life before being targeted for degradation by ubiquitination. At the next level, the availability of its cofactor BH4 is required for iNOS homodimerization and subsequent enzymatic function. Finally, there is a feedback mechanism in which NO itself can disrupt the iNOS homodimer and abrogate its function.<sup>205</sup> L-arginine is the required substrate for NO production via conversion to L-citrulline with NADPH and O<sub>2</sub> as cofactors. In myeloid cells, the cationic amino acid transporter 2 (CAT2) responsible for L-arginine uptake is essential for iNOS function.<sup>206</sup> NO can react with superoxide anion to form peroxynitrite which can modify protein tyrosine residues to activate or inactivate the modified enzyme. Proteins with free thiol groups can be S-nitrosylated by NO to modify their function. A third mechanism by which NO can alter cell function is by increased cGMP concentrations to affect G-protein signaling as well as cGMP-gated channels.<sup>205</sup>

In the TME, sources of NO include tumor cells as well as stromal cells such as macrophages and MDSC, and these cells are themselves modulated by NO. Indeed, tumors express NOS isoforms, and NO can activate NOTCH signaling to promote stemness in tumor cells.<sup>207</sup> NO exerts a tumor-promoting effect by enhancing HIF1 $\alpha$ -mediated upregulation of VEGF expression, leading to increased tumor vascularization.<sup>208</sup> It is noteworthy that NO can exert cytotoxic or anti-survival effects on tumor cells depending on its concentration. Low levels of NO have been shown to inhibit caspase activation and mitochondrial permeability to block apoptosis. On the other hand, high levels of NO can activate cell death pathways via p38/MAPK, p53, and mitochondrial cytochrome c release.<sup>205</sup> This concentration-specific effect of NO may explain in part why the differential activity of TAM toward tumor cells segregates with iNOS expression. Nitration of the chemokine CCL2 renders it incapable of attracting CD8<sup>+</sup> T cells to the tumor while in contrast nitrosylated CCL2 is more effective in recruiting MDSC.<sup>209</sup> As mentioned previously, NO can modify the TCR

to reduce its ability to recognize antigen, but MHC molecules and antigenic peptides can also be nitrosylated to exert a similar effect.<sup>108,210,211</sup> In addition to rendering T cells non-responsive at a primary level, NO also impairs T cell proliferation in response to IL-2 by inhibiting downstream signaling of IL-2R.<sup>212</sup> Induction of tumor-promoting CD4<sup>+</sup> Treg is opposed by suppression of TGF $\beta$  via iNOS, suggesting that any therapeutic approach involving iNOS and NO requires specific targeting to the myeloid compartment.<sup>213</sup>

A number of small molecule inhibitors of NO production have been evaluated for anti-tumor effects *in vivo* using mouse models of cancer. These include nitro group donors (e.g. nitroaspirins) and iNOS inhibitors (e.g. L-NMMA, L-NIL, L-NAME). Following NO blockade, decreased MDSC suppressive function is accompanied by improvement in tumor-specific CD8<sup>+</sup> T cell responses.<sup>207</sup> NO exerts differential effects on certain immune cells, so appropriate combination therapies must be considered when the effects are in opposition to the desired relief of NO-mediated immunosuppression. For example, the anti-tumor efficacy of a TLR7 agonist is enhanced by combination with a NOS inhibitor which offsets the iNOS-inducing side effects of TLR7 activation.<sup>214</sup> Similarly, the iNOS inhibitor L-NIL is combined with cyclophosphamide in order to counteract the Treg infiltration resulting from iNOS inhibition in the CD4<sup>+</sup> T cell compartment.<sup>213</sup> Currently, L-NMMA is being evaluated in a phase Ib clinical trial (NCT03236935) against various solid tumors in combination with anti-PD-1 therapy. Despite encouraging preclinical results, the clinical use of NOS inhibitors to treat sepsis, arthritis, and cardiogenic shock has met with failure and, unsurprisingly, has even caused severe cardiac side effects.<sup>215</sup> Thus, caution must be exercised in moving forward with clinical use of NOS inhibitors.

## 1.5 Introduction to Research Problems, Hypotheses, and Methodology

The activity of immunosuppressive myeloid cells in the TME contributes significantly to tumor progression and metastasis and is a critical factor in restraining the anti-tumor immunity during cancer immunotherapy. One barrier to targeting MDSC and TAM is that some therapies, such as iNOS inhibition and CCL2/CCR2 blockade, are directed against pathways shared with normal tissues or other immune cells which may cause toxicity or paradoxically further inhibit immunotherapy. These problems emphasize the necessity of targeting therapy to specific tissues and/or cell populations. Chapter 3 describes work testing the hypothesis that limiting activation of a folate-linked cytotoxic molecule to the tumor site will deplete suppressive myeloid cells and exert an anti-tumor effect. This builds on previous work in the Ratliff lab which identified FR $\beta$  as a targetable marker of MDSC and TAM.

Some functional targets for MDSC and TAM are known, but the present inability to completely abrogate MDSC function in particular suggests that additional undetermined suppressive mechanisms are active. The technical feasibility of testing all potential targets, however, is a problem due to the limited availability of tumor-derived MDSC which are the ideal test population. Moreover, functional pathways such as NO production may be regulated by a cooperative network

rather than one molecule or pathway. Chapter 4 describes work testing the hypothesis that a compound, GCL.2, predicted bioinformatically to impact the immune response but not known to directly affect MDSC functional targets will decrease MDSC function and induce an anti-tumor response. To further refine this idea, the work in Chapter 5 tests the hypothesis that a bioinformatics-based profile of interactions between compounds and gene products upregulated in tumor-derived MDSC will efficiently predict compounds that impair NO production and myeloid cell-mediated suppression of T cells. This further expands on the idea in Chapter 3 of limiting the impact of therapeutics to only the suppressive cells.

To address these hypotheses, mouse models of cancer and inflammation were utilized as sources of suppressive myeloid cells for experiments herein as described in Chapter 2. These models include the MB49 bladder cancer cell line, the RM-1 prostate cancer cell line, the EL-4 lymphoma cell line, and the POET-3 model of inducible autoimmune prostatitis. The FR $\beta$  targeting studies in Chapter 3 used a photodynamic therapy (PDT) approach with a folate-linked molecule kindly provided by OnTarget Labs (West Lafayette, IN). The work in Chapters 4 and 5 was a collaboration with Dr. Gaurav Chopra (Dept. of Chemistry, Purdue University) in which computational bioinformatics, protein structure prediction and compound interaction modeling, and chemical synthesis were used to develop a novel machine-learning approach to identify compounds with the capacity to reduce NO production in tumor-derived myeloid cells. A gene expression microarray previously performed in the Ratliff lab was the source of upregulated genes used for the compound-target interaction modeling. Various approaches to evaluate the impact on MDSC were utilized in this work including quantitative real-time polymerase chain reaction (qRT-PCR), Griess assay, fluorescence-assisted cell sorting (FACS), magnet-assisted cell sorting (MACS), and an *ex vivo* antigen-specific T cell suppression assay. Tumor growth was evaluated using direct measurement as well as bioluminescence imaging.

## 1.6 Purpose of Studies

The goal of this project is to develop immunotherapy approaches tailored to target the suppressive phenotype of myeloid cells in the TME. Targeting a phenotype and its underlying network rather than a single function-associated entity increases the likelihood that these approaches will have universal efficacy across cancer types. Additionally, using site- and cell population-specific therapies will limit toxicity and off-target effects, making such therapies more tolerable to patients. Finally, identifying the molecular networks responsible for the activity of therapeutic compounds will expand current understanding of the biology of suppressive myeloid cells.



## **CHAPTER 2. RESEARCH METHODOLOGY**

### **2.1 Common Methods**

#### **2.1.1 Mice**

Male and female mice were used for the experiments described herein. Breeding colonies for all mice in these studies were maintained in the Purdue University Transgenic Mouse Core Facility (TMCF) under 12-hour light/dark cycles with ad libitum food and water. All procedures were conducted in accordance with a protocol approved by the Purdue University Animal Care and Use Committee. Prior to tissue harvest or when humane endpoints were reached mice were euthanized by CO<sub>2</sub> asphyxiation using a PACUC-approved Euthanex regulator (EP-1305) and cage lid (E-20028) followed by secondary cervical dislocation. Information about specific strains or sexes used is given in the methods section of the relevant chapters.

#### **2.1.2 Cell Culture**

Luciferase-expressing MB49 (MB49-Luc) mouse bladder cancer cells were previously generated in the Ratliff lab via retroviral transduction of the parental MB49 cell line (a kind gift from Dr. Ian Summerhayes, Harvard Medical School) with the pLenti CMV Puro LUC (w168-1) plasmid (#17477) obtained from Addgene (Watertown, MA). The RM-1 mouse prostate cancer cell line was purchased from ATCC (Manassas, VA). The E.G7-ova mouse lymphoma line was a kind gift from Dr. William Heath, University of Melbourne. Cells were cultured in Dulbecco's Modified Eagle's Medium (DMEM) supplemented with 10% fetal calf serum (FCS), 1 mM sodium pyruvate, 4 mM L-glutamine, and 1% penicillin-streptomycin. Cells were passaged at approximately 90% confluence every 2 to 3 days. Cells were injected into mice within 5 passages after recovering from frozen stocks.

#### **2.1.3 Tumor models**

For peritoneal ascites tumors,  $1 \times 10^6$  cells were suspended in 100  $\mu$ L of phosphate-buffered saline (PBS) and injected into the peritoneal space. Tumors were allowed to grow for a total of 7 days prior to harvest of the ascites. For intradermal tumors,  $2 \times 10^5$  MB49-Luc cells,  $3 \times 10^6$  E.G7-ova cells, or  $1 \times 10^6$  RM-1 cells were injected under the skin following depilation with Nair. Tumors were allowed to grow for 10 – 14 days until a rounded nodule approximately 3 mm in diameter was visible prior to any treatments.

### 2.1.4 Flow Cytometry

Flow cytometry analysis was carried out using the BD FACS Canto (Purdue University Department of Comparative Pathobiology) or the BD Fortessa LSR (Purdue University Flow Cytometry and Cell Separation Core Facility). Data were analyzed using FlowJo software (Treestar, Inc).

To evaluate T cell proliferation, OT-I cells were incubated with EdU which was detected via conjugation to Alexa488 dye.

For analysis of lymphoid and myeloid populations a standard staining protocol was followed. Cells were resuspended in PBS at  $1 \times 10^7$  cells/mL. To label dead cells, Zombie fixable viability dye (BioLegend) was used at a 1:2000 dilution and incubated for 10 minutes at room temperature. Anti-mouse Fc block (BioLegend) was added at a 1:500 dilution and incubated for 10 minutes at 4°C to prevent non-specific binding of antibodies by phagocytes. Finally, the indicated fluorescent antibodies were added at a 1:1000 dilution and incubated for 15 minutes at 4°C. Cells were then washed in PBS, fixed for 10 minutes in 10% neutral-buffered formaldehyde, washed in PBS, and stored at 4°C until analysis. Any intracellular staining was performed after surface staining and after fixation. Intracellular antibodies were diluted at 1:500 in permeabilization buffer (0.1% saponin, 0.5% BSA in PBS) and incubated with cells for 30 minutes at room temperature. Fluorescence compensation was performed using CompBeads (BD Biosciences) appropriate to the antibody isotypes. The following antibody clones purchased from BioLegend were used: 30-F11 (CD45), M1/70 (CD11b), HK1.4 (Ly6C), 1A8 (Ly6G), BM8 (F4/80), 10F.9G2 (PD-L1), 145-2C11 (CD3 $\epsilon$ ), 53-6.7 (CD8a), GK1.5 (CD4), RMT3-23 (TIM3), C9B7W (LAG3), 29F.1A12 (PD-1), and XMG1.2 (IFN $\gamma$ ). To detect iNOS, an anti-mouse antibody (D6B6S, Cell Signaling Technology) was used for studies in Chapter 4, and a polyclonal antibody (NBP1-50606, Novus Biologicals) was used for studies in Chapter 5. Anti-FR $\beta$  was kindly provided by Dr. Dimiter Dimitrov (National Institutes of Health) and fluorescently labeled using an antibody labeling kit (Thermo Fisher Scientific) according to manufacturer's instructions.

### 2.1.5 Statistical Analysis

Data are presented as mean  $\pm$  standard deviation (SD). Except where indicated, an unpaired one-tailed Student's *t*-test was performed using GraphPad Prism 6 (La Jolla, CA).

## **CHAPTER 3. FOLATE-TARGETED PHOTODYNAMIC THERAPY ABLATES MDSC FROM INFLAMED TISSUE AND INDUCES TUMOR REGRESSION IN A MOUSE MODEL**

### **3.1 Introduction**

Direct depletion of TAM and MDSC is one of the key strategies under investigation as a means of relieving immunosuppression in the TME and restoring a robust anti-tumor immune response. So far, efforts to directly kill these cells include exploiting serendipitous effects of chemotherapy drugs such as gemcitabine, 5-FU, and bisphosphonates as well as antibody-mediated depletion.<sup>158–161,163,180</sup> However, chemotherapy drugs cause significant morbidity in patients due to a lack of discrimination between normal and malignant cells. The lack of markers for MDSC and TAM that are not shared with potentially beneficial immune cells makes antibody-targeting potentially problematic as well. Ideally, cytotoxic molecules would be specifically targeted to the suppressive cells and/or their cytotoxic action would be restricted to the tumor site.

One approach that limits activation of therapeutic molecules to a specific site is photodynamic therapy (PDT). PDT consists of the administration of a photosensitizer (PS) and its subsequent activation by applying light of a specific wavelength, often with a laser, to a defined site where the PS has accumulated. There is also an absolute requirement for O<sub>2</sub> as the cytotoxic mechanism of PDT depends on the generation of ROS via release of highly-reactive singlet oxygen. Early photosensitizers were porphyrins or derivatives thereof, and newer PS molecules used clinically in cancer therapy are based on chlorins. To date, PDT has been used to treat a wide variety of solid tumors, including lung, brain, lung, breast, prostate, and bladder cancers.<sup>216</sup> PS molecules tend to accumulate in tumors for reasons that have yet to be elucidated, but they can also be directed to specific targets via receptor-ligand interactions. The anti-tumor effects of PDT are mediated through three key mechanisms: direct cell killing, collapse of tumor vasculature, and activation of immune response. Direct killing can occur via induction of apoptosis, necrosis, or autophagy, depending in part upon which organelles or cellular structures are damaged by PDT.<sup>217</sup> PDT-induced collapse of the tumor microvasculature can lead to delayed tumor growth and profound hypoxia within the tumor.<sup>218</sup> Finally, PDT results in the release of inflammatory mediators that attract and stimulate neutrophils and macrophages toward a tumoricidal program. The release of tumor antigens following cell death is believed to further enhance the adaptive immune response via more efficient antigen presentation by phagocytes.<sup>219</sup> Thus, PDT has potential both as a direct anti-cancer treatment but also as an adjuvant to immunotherapy.

Previous work in the Ratliff lab has identified FR $\beta$  as a marker of MDSC and TAM with immunosuppressive capacity at the tumor site. This work also demonstrated that FR $\beta$  is targetable via folic acid conjugates (G. Cresswell, manuscript submitted). Through the studies in this chapter we sought to address the inability to specifically direct cytotoxic therapy to suppressive myeloid

cells in the TME. The key questions were 1) Can TAM and MDSC be depleted from solid tumors using PDT? 2) Does folate-targeted PDT exert a therapeutic anti-tumor effect? Through a collaboration with On Target Laboratories (West Lafayette, IN) we were able to utilize a novel folate-targeted PS to address these questions.

## **3.2 Methods**

### **3.2.1 Mice**

Albino C57BL/6J mice were used in these experiments in order to minimize the impact of melanin on laser light penetration. Female mice were used in tumor experiments to take advantage of the immunogenicity of the male-derived MB49-Luc cell line. When folate-targeted molecules were used, the mice were fed a folate-deficient diet (TD.95247; Envigo, USA) and housed on folate-free pine bedding for a minimum of two weeks prior to and throughout the experiment. This was to reduce the amount of endogenous folate that could compete with the compounds.

#### **3.2.1 Folate-targeted compounds**

Dr. Philip S. Low and Dr. Sumith Kularatne of On Target Laboratories generously provided the non-toxic fluorescent folate conjugate OTL38 and the folate-linked PDT photosensitizer PG05132. OTL38 (MW: 1414.42 Da) is folate conjugated to the near-infrared dye S0456 and can be detected via flow cytometry using an APC/Cy7 filter set.<sup>220</sup> PG05132 (MW: 1493.6 Da) is folate conjugated to bacteriochlorin a.

#### **3.2.2 BCG infection model**

Mice were anesthetized with isoflurane gas, and the ear pinna was immobilized on a rigid surface using double sided tape. A 33-ga tuberculin needle was used to inject 10  $\mu$ L of TICE BCG suspension or sterile saline under the dorsal aspect of the pinna. The exact CFU of the BCG suspension is unknown but is approximately  $1 - 8 \times 10^8$  CFU/mL according to the package leaflet. The infection was allowed to develop for 24 – 96 hours prior to PDT and/or tissue harvest.

#### **3.2.3 OTL38 labeling experiments**

Cell lines: Cells were cultured in folate-free RPMI-1640 medium for 24 hours and under hypoxic conditions (1% O<sub>2</sub>) to mimic the oxygen levels in a TME. The cell monolayers were then incubated with 100 nM OTL38 in either complete RPMI-1640 medium or folate-free medium for 30 minutes. Cells were then washed with PBS and trypsinized. OTL38 labeling was detected by flow cytometry.

**Tumors:** Intradermal MB49-Luc tumors were grown for 14 days. The mice were immobilized using a rodent restrainer and placed under a heat lamp for approximately two minutes in order to dilate the tail veins. A dose of 40 nmol OTL38 was dissolved in 100  $\mu$ L of sterile PBS and injected via the tail vein. Control animals received the same volume of PBS only. Two hours after injection the mice were euthanized and tumors were harvested for analysis by flow cytometry.

### **3.2.4 Photodynamic therapy**

Mice were restrained in a rodent restrainer and placed under a heat lamp for approximately two minutes in order to dilate the tail veins. A dose of 30 nmol (BCG infection model) or 40 nmol (tumor models) PG05132 dissolved in 100  $\mu$ L of sterile PBS was then injected intravenously via the tail vein. Control animals received 100  $\mu$ L of sterile PBS only. The PG05132 was allowed to circulate for two hours prior to laser treatment. During laser treatment, mice were anesthetized with isoflurane gas and placed on a heating pad to maintain body temperature. Laser treatment was accomplished using a 750-nm laser source (BWF1, B&W Tek) set to 400 mA with a spot size of 0.5 cm. The additional information needed to calculate the energy delivered by this setup was unavailable. BCG-infected ears were treated for 15 minutes, and tumors were treated for 30 minutes. For tumors, if the spot size was smaller than the tumor area then the laser was repositioned at regular intervals (e.g. every 10 minutes) to ensure the entire surface of the tumor was exposed. Schematics are shown in Figures 3.1B and 3.2B.

### **3.2.5 Imaging**

Tumor-bearing mice treated with PG05132 underwent fluorescence imaging immediately before and after laser treatment in order to evaluate accumulation of the PS at the tumors site and confirm photobleaching by the laser. An excitation wavelength of 745 nm and a 790-nm emission filter were used. Imaging was performed under isoflurane anesthesia using the Spectral AMI instrument in the Bindley Imaging Facility at Purdue University.

### **3.2.6 Tissue harvest and preparation for FACS**

BCG-infected ears were excised and then separated into dorsal and ventral leaves using forceps. The tissue was minced with a razor blade and digested using 5 mg/mL collagenase type IV in complete RPMI-1640 medium by incubating for one hour at 37°C in an orbital shaker (VWR) set to 100 RPM. The resulting cell suspension was filtered through 70- $\mu$ m mesh and RBCs were removed by incubating in hypotonic lysis buffer for 5 minutes at room temperature. Next, cells were resuspended and stained according to Section 2.4 and analyzed by flow cytometry. Representative images of the gating strategy are show in Figure 3.1A.

Intradermal tumors were excised from the skin and minced using a razor blade. The resulting slurry was digested as described above. The cell suspension was filtered and RBCs were removed as described above. Cells were resuspended and stained according to Section 2.4 and analyzed by flow cytometry. Representative images of the gating strategy are shown in Figure 3.2A.

### 3.3 Results

To test the feasibility of PDT as means of depleting myeloid cells we desired a simple model that is easy to access and manipulate. Martino *et al* showed that BCG rapidly recruit MDSC to the site of infection, so we chose to use the intradermal infection of the mouse ear pinna model described in that work.<sup>221</sup> We first ensured that we could reproduce the model. Inflammation in the ear pinna as indicated by redness and local edema was apparent within 24 hours (Figure 3.3A) post-infection. G-MDSC were prominent among the influx of cells while M-MDSC were less frequent when comparing BCG-infected ears to saline-injected control ears. Though the frequency of G-MDSC remained steady between 24 and 72 hours, the frequency of M-MDSC declined by 72 hours (Figure 3.3B). We next performed a timecourse for FR $\beta$  expression in order to pinpoint the appropriate point in the course of infection for application of folate-targeted PDT. There was a steady increase in FR $\beta$  expression for both MDSC subsets between 24 and 72 hours post-infection that was maintained at 96 hours (Figure 3.3C). After 96 hours, the visually apparent signs of infection began to resolve. We chose to perform subsequent PDT experiments with this model at 72 hours post-infection. This was done despite the decrease in M-MDSC because the frequency of FR $\beta$ -expressing M-MDSC was still trending upward and the frequency of FR $\beta^+$  G-MDSC had increased substantially compared to the 48-hour timepoint but did not increase further at 96 hours.

We next tested whether BCG-recruited MDSC could be depleted by folate-targeted PDT and the time period in which this might occur. For these experiments, both ears were infected with BCG, and mice were randomly assigned to either the PBS vehicle control or the PG05132 treatment group. Only the left ear was exposed to the laser, thus allowing us to use the right ear as an internal untreated reference. Figure 3.4 shows no difference between the vehicle and PG05132 groups at 2 and 4 hours post-PDT while there is a significant reduction in G-MDSC after 24 hours. In this experiment, M-MDSC could not be detected in either treatment group at 24 hours. It is worth noting there are more viable G-MDSC in the laser-treated ears of vehicle control animals, suggesting that the laser treatment itself exerts some effect on the viability of cells.

Since folate-targeted PDT could deplete MDSC from the BCG-infection model we wanted to evaluate its efficacy in a tumor model. We considered three cell lines to generate tumors for these studies: E.G7-ova, RM-1, and MB49-Luc. To select the most suitable model(s), we assessed FR $\beta$  expression by MDSC recruited to the tumors of mice fed a folate-deficient diet. The E.G7-ova tumor model, attractive as an immunogenic target, recruited FR $\beta$ -expressing MDSC at low frequency, making it unsuitable for folate-targeted PDT. The RM-1 and MB49-Luc tumor models both recruited FR $\beta$ -expressing M-MDSC, and MB49-Luc tumors were superior in recruitment of

FR $\beta$ <sup>+</sup> G-MDSC (Figure 3.5A). For initial studies, we utilized the RM-1 tumor model. RM-1 cells are poorly immunogenic, so later studies to assess tumor growth and survival were carried out using MB49-Luc tumors which express the male H-Y minor histocompatibility antigen and are thus immunogenic in female mice.<sup>222,223</sup> Next, we determined that the fluorescent folate compound OTL38 is internalized by tumor-associated myeloid cells *in vivo* (Figure 3.5B). We then verified that the photoactivatable compound PG05132 accumulates at the tumor site. PG05132 is weakly fluorescent in the far-red wavelength range, and Figure 3.5C shows accumulation of the compound in the tumor (left image). The image on the right depicts photobleaching of PG05132 following a 30-minute treatment with a 750-nm laser.

As with the BCG infection model, we needed to determine the timeline over which tumor-associated MDSC are impacted by folate-targeted PDT. The RM-1 tumor model was used for these experiments. We first tested the viability of MDSC subsets at 2 and 4 hours post-PDT. Figure 3.6A show that viability at 2 hours is unchanged while the accumulation of Zombie Violet dye at 4 hours post-PDT indicates decreased viability of both MDSC subsets. The change is only significant for G-MDSC. PG05132 is expected to be internalized almost exclusively by FR<sup>+</sup> cells, so next we investigated whether the frequency of FR $\beta$ -expressing cells among the remaining viable myeloid cells, now including TAM, was altered at the 4-hour timepoint. Compared to mice treated with the vehicle, PG05132-treated mice had significantly fewer FR $\beta$ <sup>+</sup> TAM, G-MDSC, and M-MDSC. We also compared mice treated with the vehicle or PG05132 but without laser treatment and found no difference in FR $\beta$  expression (Figure 3.6B). Durable depletion of suppressive myeloid cells is expected to be necessary for any therapeutic effects on anti-tumor immunity. When we extended the post-PDT timepoint to 24 hours the frequency of FR $\beta$  cells was still significantly reduced in the three myeloid populations under study (Figure 3.6C).

We next conducted a series of experiments using the MB49-Luc tumor model to assess the immunotherapeutic potential of folate-targeted PDT. Because many epithelial tumors overexpress folate receptors we needed to determine whether the tumor cells themselves would be a target. We used the fluorescent folate conjugate OTL38 to test whether MB49-Luc cells would internalize a folate-link compound *in vitro*. The mouse lung carcinoma cell line M109 was used as a positive control, and complete RPMI-1640 medium was used as the source of folic acid (FA) to compete with OTL38. The fluorescence of MB49-Luc was unchanged, indicating that the cells did not internalize any of the FA conjugate. In contrast, the fluorescence of M109 cells incubated with OTL38 in FA-free medium increased nearly 30-fold over OTL38 + FA (Figure 3.7A). In tumor-bearing mice injected with 40 nmol of OTL38 the increase in fluorescence associated with OTL38 in CD45<sup>neg</sup> population is minimal, suggesting that the epithelium-derived tumor cells are not significant targets of folate-linked compounds (Figure 3.7B). Next, we tested whether folate-targeted PDT would deplete myeloid cells at the 24-hour timepoint in the MB49-Luc model as it did in the RM-1 model. There was a significant reduction in the frequency of viable TAM and M-MDSC but not G-MDSC (Figure 3.7C). Myeloid cells in the tumor are constantly replenished by the circulating cells originating from bone marrow, so we sought to determine how long the PDT-

mediated depression in the myeloid populations would last. For both TAM and M-MDSC the effect lasted at least 48 hours post-PDT, and the difference between vehicle and PG05132-treated mice had resolved within 72 hours. The increase in overall cellularity in both treatment groups after 24 hours may indicate, as in the BCG infection model, an inflammatory effect from the laser treatment itself. No differences were observed at any timepoint for G-MDSC (Figure 3.7D). The lack of effect on G-MDSC contrasts with our results from the RM-1 tumor model as well as the BCG infection model. Previous work in the Ratliff lab suggests that while tumor-derived G-MDSC express FR $\beta$  it may not always be functional (G. Cresswell, unpublished data). Together, these results suggest that the context of inflammation may influence whether FR $\beta$ -mediated endocytosis is active in G-MDSC. All experiments with the RM-1 model were carried out using a dose of 40 nmol PG05132, but we wanted to determine whether a higher dose would more profoundly deplete myeloid cells. We found that 24 hours after PDT there was no difference in the frequency of viable TAM, G-MDSC, or M-MDSC between 40 and 80 nmol doses (Figure 3.7E). Based on this result we continued to use the 40 nmol dose for future experiments.

After establishing MB49-Luc as a viable tumor model and determining that 40 nmol of PG05132 is a sufficient dose of photosensitizer we tested the anti-tumor efficacy of folate-targeted PDT. In an initial experiment we followed survival of tumor-bearing mice after treatment. All of the vehicle-treated mice were euthanized within 8 days of treatment due to large tumors whereas 2 of 6 PG05132-treated mice survived long-term and experienced complete tumor regression (Figure 3.8A). In a larger follow-up experiment we measured tumor growth as well as survival. The growth of PG05132-treated tumors remained flat for a week post-PDT and was significantly slower than vehicle-treated tumors (Figure 3.8C). Tumor growth was followed until most of the vehicle group had been euthanized due to large tumor size. Overall survival was significantly better in the PG05132-treated group (Figure 3.8B).

### 3.4 Discussion

We have demonstrated that MDSC and TAM can be targeted for killing by delivery of a cytotoxic agent via FR $\beta$ . Because FR $\beta$  is apparently restricted to myeloid populations it may thus be possible to limit unwanted cytotoxicity toward other immune cell populations. This is an important step forward for immunotherapy as it partially addresses the present inability to target suppressive myeloid cells in a specific manner. We further limited side effects by using PDT to spatially restrict the cytotoxic action to the site of laser treatment. In this way, healthy cells elsewhere in the body that might internalize the folate-targeted PS are protected. TAM have been depleted from mouse tumors using strategies that target the class A scavenger receptor (SRA; CD163) and the mannose receptor (CD206) using PS modified with albumin and mannose, respectively.<sup>224,225</sup> Both CD163 and CD206 are considered to be macrophage markers; however, the exclusive association of these markers with a pro-tumor phenotype is controversial.<sup>226</sup> A few reports have indicated that MDSC also express CD206.<sup>227–229</sup> Importantly, these strategies do not allow dual targeting of suppressive myeloid cells and tumor cells. On the other hand, our folate-targeted PS can be internalized by any



cell with a functional folate receptor. This includes FR $\beta$ -expressing myeloid cells but would also impact tumor cells which frequently overexpress FR $\alpha$  as well as FR $\beta$ .<sup>203</sup> Finally, targeting suppressive immune cells remains a unique application given that PDT is primarily intended to target tumor cells directly rather than other components of the TME. In the course of these studies, we made several interesting observations with bearing on the utility of PDT for targeting suppressive myeloid cells.

In the BCG infection model, we observed that the frequency of viable G-MDSC increased with exposure to the laser, indicating a direct effect of the laser itself on the cells. Indeed, after exposure periods as short as a few seconds, far-red wavelength lasers have been shown to induce a localized heat injury to the skin which results in an influx of neutrophils.<sup>230</sup> As the Ly6C<sup>+</sup> Ly6G<sup>high</sup> population can contain neutrophils as well as G-MDSC this may explain the phenomenon we observed. It is further possible that a similar effect occurred in our tumor models. The frequency of FR $\beta$ -expressing G-MDSC decreased after PDT but the overall frequency of viable G-MDSC was unchanged. If this effect is actually due to an influx of neutrophils the consequences for tumor growth after PDT could be positive or negative based on previous reports.<sup>219</sup>

Another important observation from our studies is that, as in E.G7-ova, not all tumors will recruit FR $\beta$ -expressing MDSC. Similarly, not all tumors, even within the same subtype, express FR $\alpha$ .<sup>231</sup> Shen *et al* performed immunohistochemistry staining for FR $\beta$  expression using human tumor tissue microarrays containing samples from more than 20 different tumor types. Overall, approximately 25% of the tumors expressed FR $\beta$ , and half contained FR $\beta$ <sup>+</sup> macrophages in the stroma. Across tissue types, however, FR $\beta$  positivity in the tumor stroma ranged from 14% (uterus) to 91% (lymph node) in agreement with our observation that FR $\beta$  expression can vary between tumor models.<sup>203</sup> There is rarely a “one size fits all” scenario in cancer therapy, and the inter-tumor variability of the TME is likely a key factor. For instance, hypoxia in the tumor corresponds with higher FR $\beta$  expression in MDSC and TAM. (G. Cresswell, manuscript submitted) Thus, in a clinical setting it will be important to confirm FR expression in the tumor and/or stromal myeloid cells prior to attempting folate-targeted PDT. In cases where FR isoforms are entirely absent from the tumor and the stroma, a different immunotherapeutic strategy, such as ICB or immunization with tumor antigens, would be necessary in order to enhance the effects of direct tumor cell killing.<sup>232,233</sup>

Missing from these studies is an evaluation of MDSC suppressive activity following PDT. The small size of intradermal tumors and correspondingly small number of MDSC in combination with PDT-mediated depletion precluded the technical feasibility of obtaining sufficient numbers of cells for *ex vivo* suppression assays. The low level of folate-conjugate uptake *in vivo* by CD45<sup>neg</sup> tumor-associated cells suggests that direct tumor cell killing is not the main mechanism underlying the observed delay in tumor growth; however, we cannot rule out this possibility. Although microvasculature collapse is another potential mechanism for PDT-mediated tumor destruction this is also unlikely to play a major role in our model. The PS must be within nanometers of its target in order to mediate damage, and the two hours of circulation time in our studies was likely

sufficient to clear the PS from the bloodstream.<sup>234</sup> Thus, the anti-tumor effect we observed could be attributed to the depletion of suppressive myeloid cells and a subsequent increase in anti-tumor immunity. The transience of this effect may be due to the rebound of the myeloid cell populations that occurred within 72 hours of PDT. It should be noted that the functional status of the newly-recruited cells is unknown, and they may not be immediately suppressive. Additional experiments utilizing antibody-mediated depletion of CD8<sup>+</sup> T cells as well as MDSC and TAM prior to PDT are necessary to determine the roles of direct tumor cell killing and indirect immunotherapy in the delayed tumor growth we observed.

Other factors which were not optimized in these studies are the specific parameters of the PDT procedure, including PS dose, total light dose (energy delivered to target site), and fluence rate (energy delivered per unit of time) as well as treatment fractionation. The first three factors are interrelated and influence the efficiency of PDT through oxygen consumption in the treatment site. PDT itself consumes oxygen which is present at a low level in the hypoxic TME. Collapse of vasculature due to inflammation or direct effects of PDT further limits the availability of oxygen. Thus, a high PS dose combined with a high fluence rate will more rapidly deplete oxygen and potentially limit the efficacy of PDT.<sup>235</sup> We preliminarily established that the PS dose used in our studies is maximal but did not test lower doses to determine the minimum effective dose. The fluence rate is determined by changing the total light dose and the exposure time, and we did not test any alternatives from the parameters used in our studies. Finally, treatment fractionation involves multiple dose of the PS and/or multiple applications of the laser treatment at different times. This may be done to manage oxygen consumption, target both the vasculature and the tissue, or further deplete sensitive cells after initial treatment. In our studies, treatment fractionation could be used to address the myeloid cell rebound observed 72 hours post-PDT. This would necessitate studies to determine when a substantial population with functional FR $\beta$  reappears. Taken together, it may be possible to improve myeloid cell depletion and anti-tumor activity by optimizing the aforementioned aspects of the procedure. However, optimizing a single depletion event does not compensate for the rapid rebound of the myeloid cells at the tumor site in the following days. Tumor growth in our studies was restrained for a short period, but the tumors ultimately began to grow rapidly again. Frequent repeat treatments might address the rebound, assuming the infiltrating myeloid cells are targetable, but this is likely not sustainable long-term as a clinical therapy. Thus, as described in Chapters 4 and 5, we considered alternative strategies to address immunosuppression in the TME by reducing MDSC suppressive function in a direct and sustained manner using novel small molecule immunomodulators

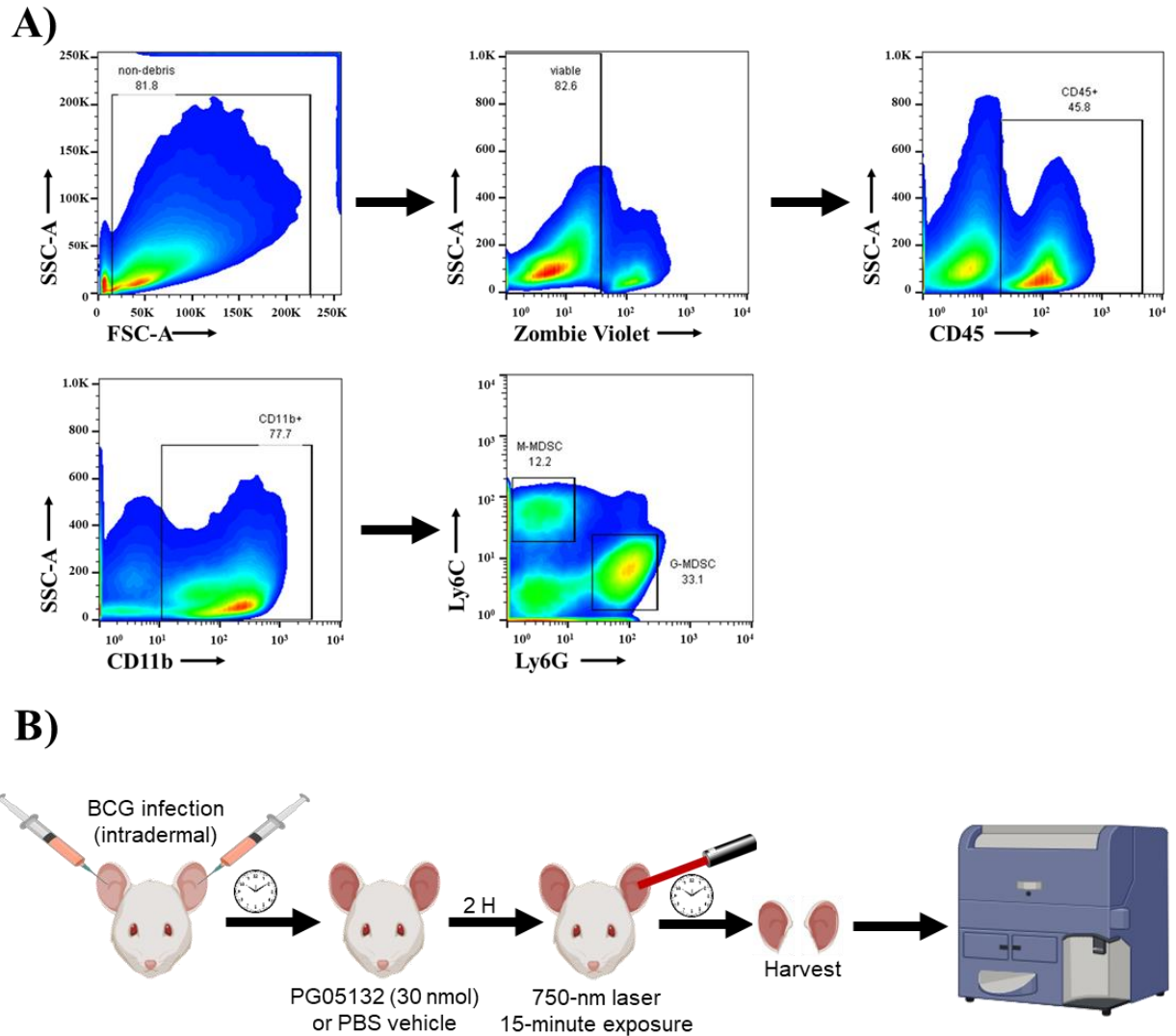


Figure 3.1 FACS gating strategy and photodynamic therapy in a BCG infection model

A) Representative plots show hierarchical gating strategy to exclude debris (SSC-A<sup>low</sup> FSC-A<sup>low</sup>) and dead cells (Zombie violet<sup>+</sup>) from leukocytes (CD45<sup>+</sup>) followed by inclusion of M-MDSC (Ly6C<sup>high</sup> Ly6G<sup>neg</sup>) and G-MDSC (Ly6C<sup>+</sup> Ly6G<sup>+</sup>) from the myeloid gate (CD11b<sup>+</sup>). B) Schematic illustrating the approach for PDT-mediated depletion of MDSC in the BCG infection model. Color change of mouse ears indicates inflammation resulting from BCG infection.

Graphics created with BioRender.com.

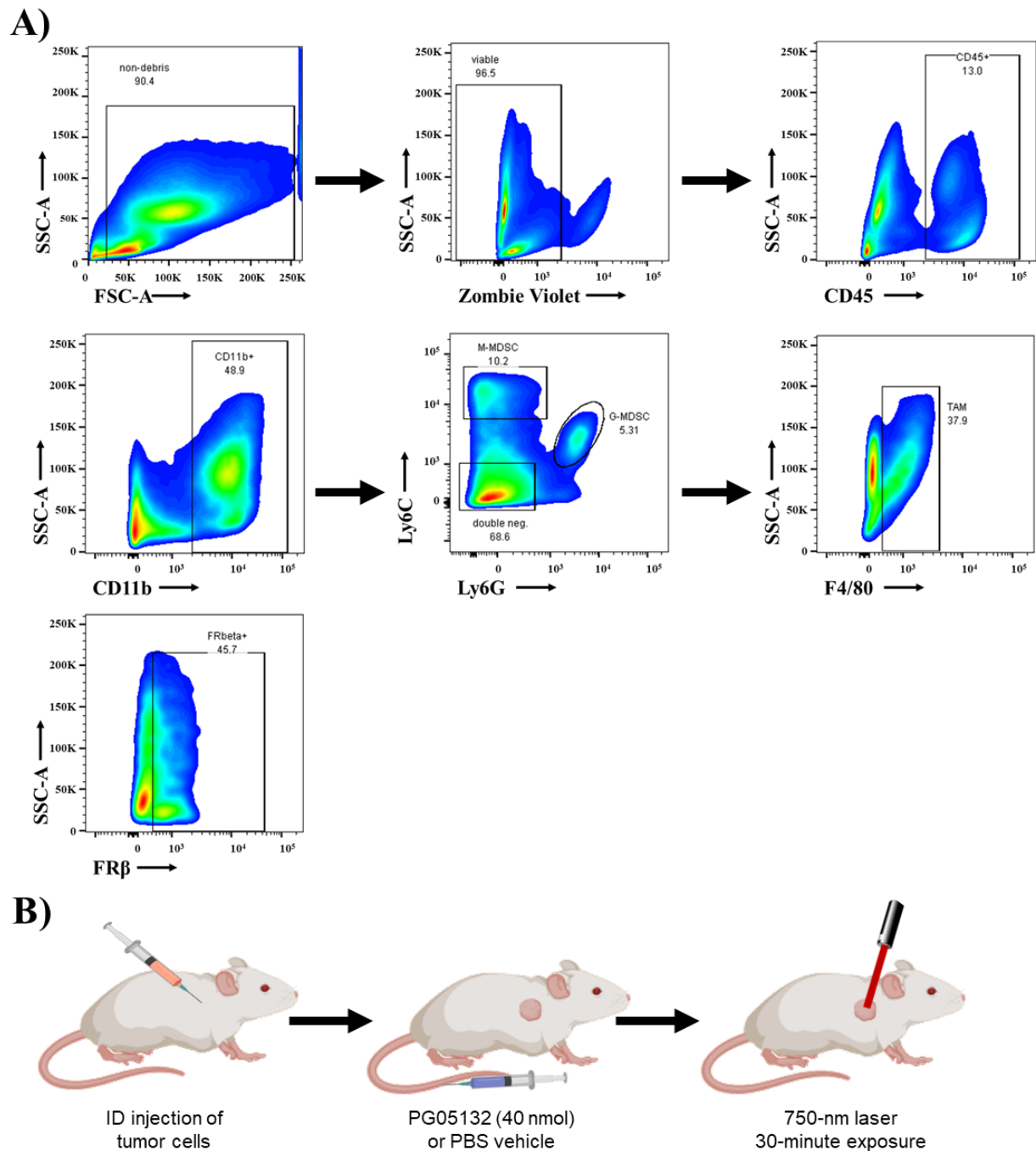


Figure 3.2 FACS gating strategy and photodynamic therapy in a tumor model

A) Representative plots show hierarchical gating strategy to exclude debris ( $\text{SSC-A}^{\text{low}}$   $\text{FSC-A}^{\text{low}}$ ) and dead cells ( $\text{Zombie violet}^+$ ) from leukocytes ( $\text{CD45}^+$ ) followed by inclusion of M-MDSC ( $\text{Ly6C}^{\text{high}}$   $\text{Ly6G}^{\text{neg}}$ ), G-MDSC ( $\text{Ly6C}^+$   $\text{Ly6G}^+$ ), and TAM ( $\text{Ly6C}^{\text{neg}}$   $\text{Ly6G}^{\text{neg}}$   $\text{F4/80}^+$ ) from the myeloid gate ( $\text{CD11b}^+$ ).  $\text{FR}\beta$ -expressing cells were gated within the named populations. B) Schematic illustrating the approach for PDT-mediated depletion of MDSC and TAM in an intradermal tumor model. Graphics created with BioRender.com.

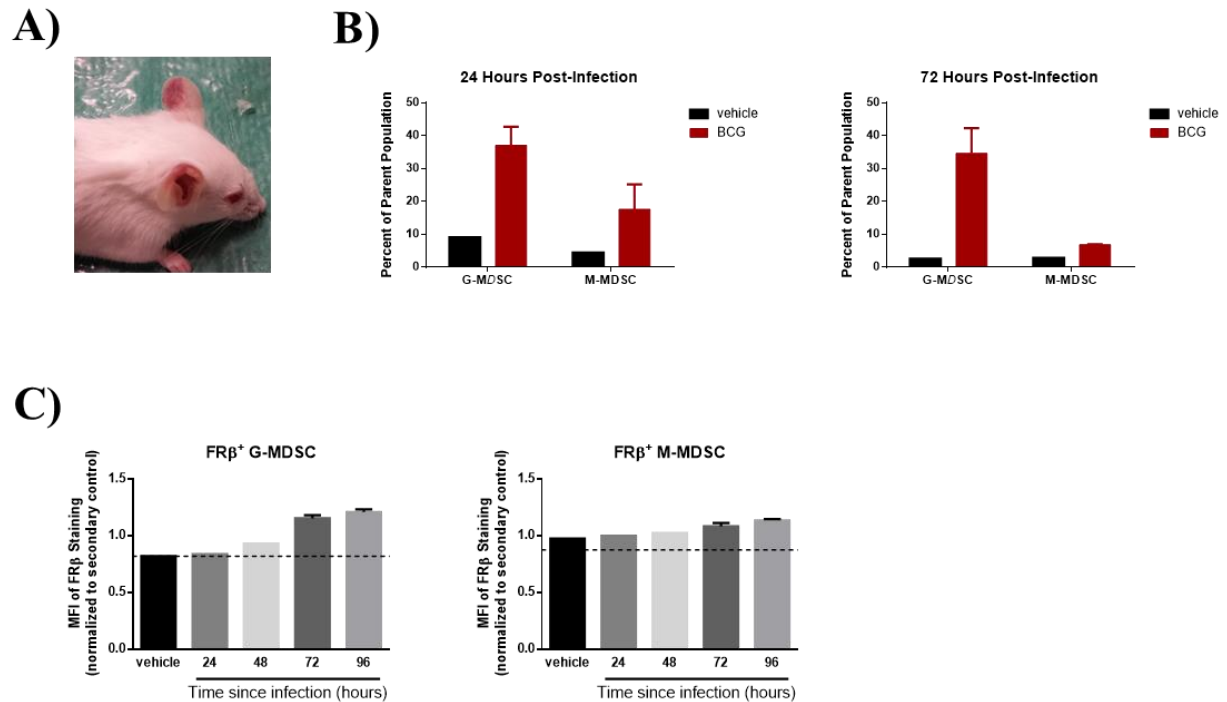


Figure 3.3 Intradermal BCG recruit FR $\beta$ -expressing MDSC subsets to the infection site

A) Photo of a mouse illustrating inflamed ears 24 hours after infection with BCG. B) MDSC infiltration of ear tissue at 24 and 72 hours post-infection. One mouse at each timepoint was injected with saline (vehicle), and two mice at each timepoint were infected with BCG. C) Timecourse of FR $\beta$  expression in MDSC after BCG infection. One mouse was included in the vehicle, 24, and 48 hour groups while 3 mice were included at the 72- and 96-hour timepoints. Error bars represent standard deviation.

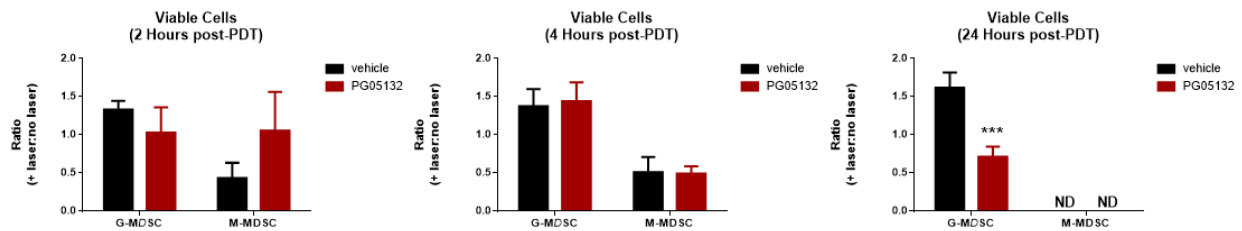


Figure 3.4 Folate-targeted PDT reduces the viability of G-MDSC at the site of BCG infection

Shown is the ratio of viable G-MDSC and M-MDSC in the laser-treated ear compared to the non-exposed ear within the same animal. Two mice were included in each group at 2 and 4 hours, and three mice were included in each group at 24 hours. Error bars represent standard deviation. Statistical test was a one-tailed student's t-test, and \*\*\*p<0.005.

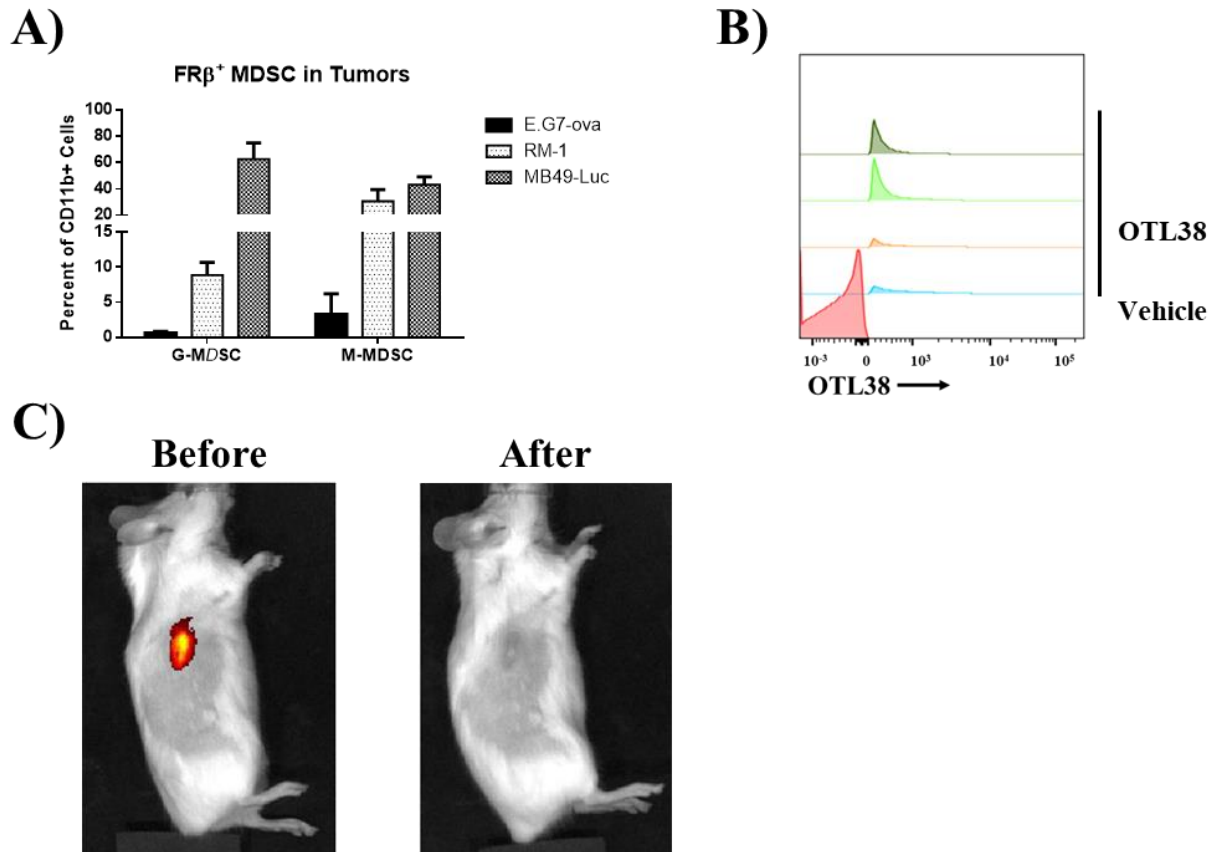


Figure 3.5 Tumors recruit FR $\beta$ -expressing myeloid cells and accumulate a folate-targeted photosensitizer

A) Comparison of FR $\beta$  expression by MDSC among E.G7-ova (n=4), RM-1 (n=3), and MB49-Luc (n=4) mouse tumor models. Mice were fed a folate-deficient chow, and tumors were allowed to grow for 14 days prior to harvest for analysis. Error bars represent standard deviation. B) Histogram showing uptake of OTL38 by CD11b<sup>+</sup> cells isolated from MB49-Luc tumors grown in mice fed a folate-deficient diet. C) Representative image showing accumulation of the folate-targeted photosensitizer PG05132 in an MB49-Luc intradermal tumor (left) with subsequent photobleaching of fluorescence after laser treatment (right).

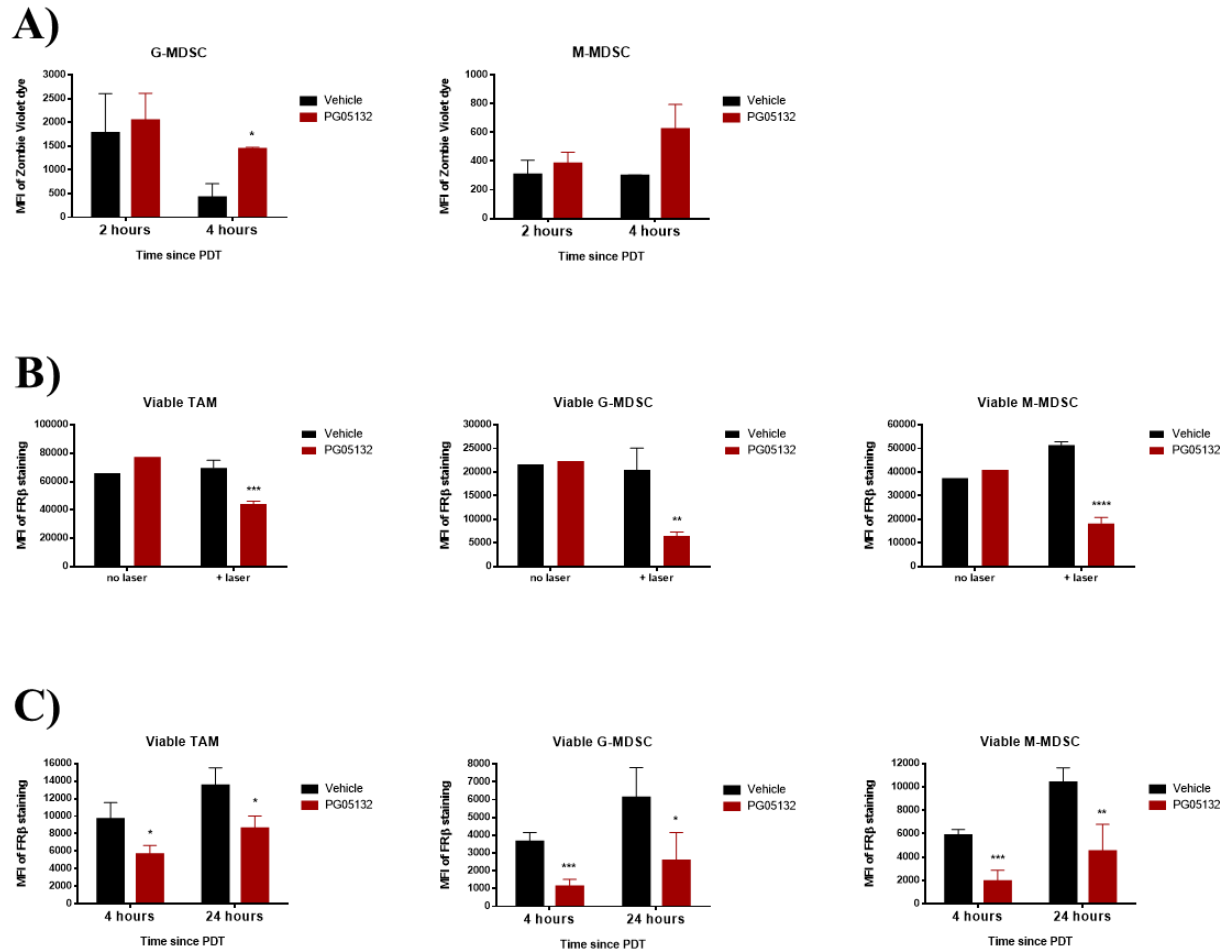


Figure 3.6 Folate-targeted PDT rapidly depletes FR $\beta$ -expressing MDSC from the tumor

A) RM-1 tumors (n=2 per group) were subjected to PDT and harvested after the indicated interval for FACS analysis of cell viability. B) RM-1 tumors (n=3 per group in “+ laser”, n=1 per group in “no laser”) were treated with vehicle or PG05132 and laser exposure as indicated. After 24 hours, FR $\beta$  expression in myeloid cell populations was examined by FACS. C) RM-1 tumors (n=3 per group) were subjected to PDT and tumor-infiltrating cells were analyzed by FACS after the indicated time intervals. Error bars represent standard deviation. Statistical test was a one-tailed student’s t-test, and \*p<0.05, \*\*p<0.01, \*\*\*p<0.005.



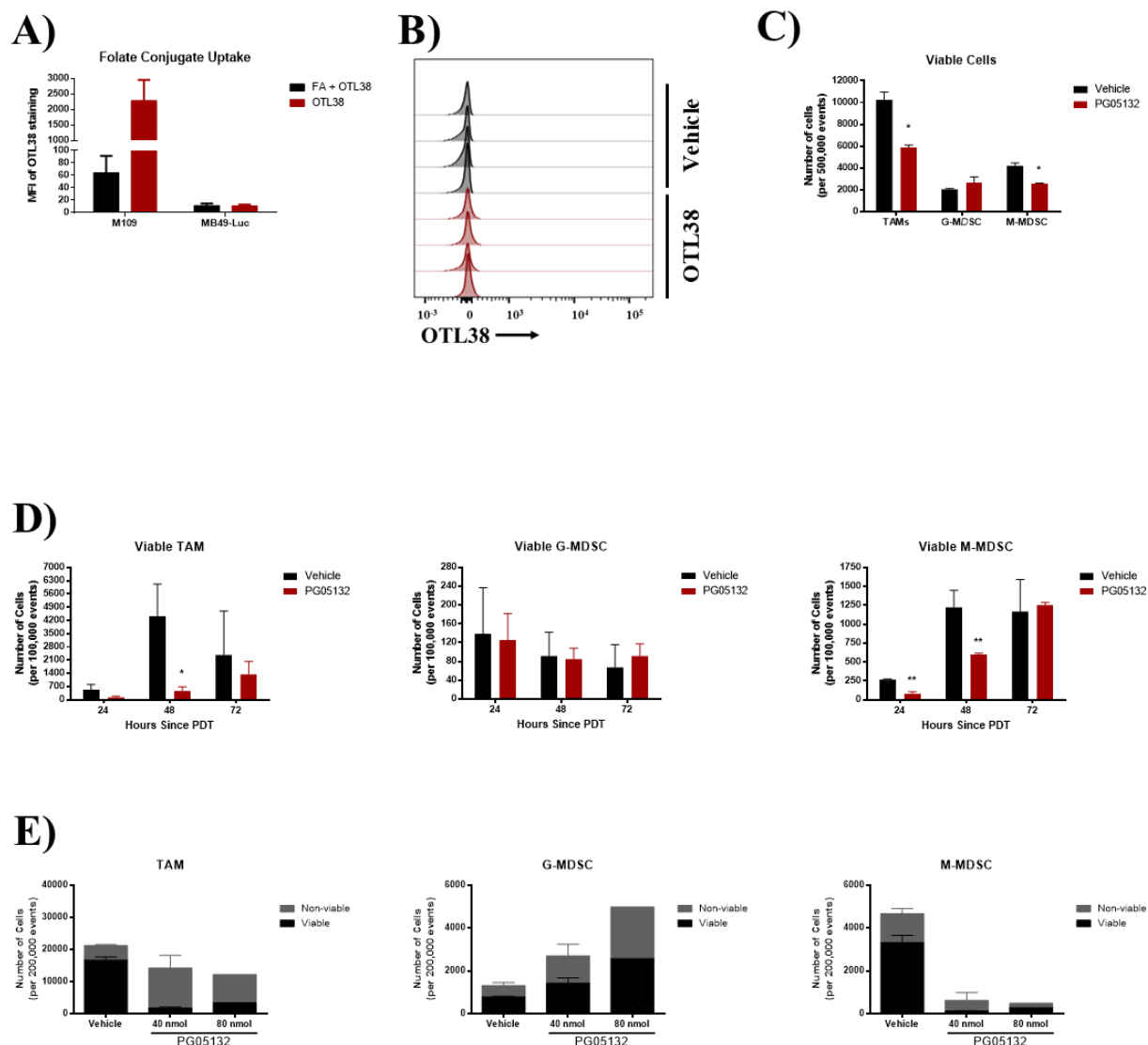


Figure 3.7 Folate-targeted PDT transiently depletes myeloid cells from MB49-Luc tumors

A) In vitro uptake of OTL38 by cancer cell lines in the presence (FA + OTL38) or absence (OTL38) of folic acid from medium. Error bars represent standard deviation from two independent experiments. B) Histograms showing uptake of OTL38 (red) compared to vehicle (black) by CD45neg cells isolated from MB49-Luc tumors grown in mice fed a folate-deficient diet. C - D) MB49-Luc tumors (n=2 – 3 per group) were subjected to PDT, and viability of myeloid cells was quantified via FACS after the indicated time intervals. E) MB49-Luc tumors (n=1 – 2 per group) were subjected to PDT with the indicated doses of PG05132, and viability of myeloid cells was quantified via FACS after 24 hours. Error bars represent standard deviation. Statistical test was student's t-test, and \*p<0.05, \*\*p<0.01.

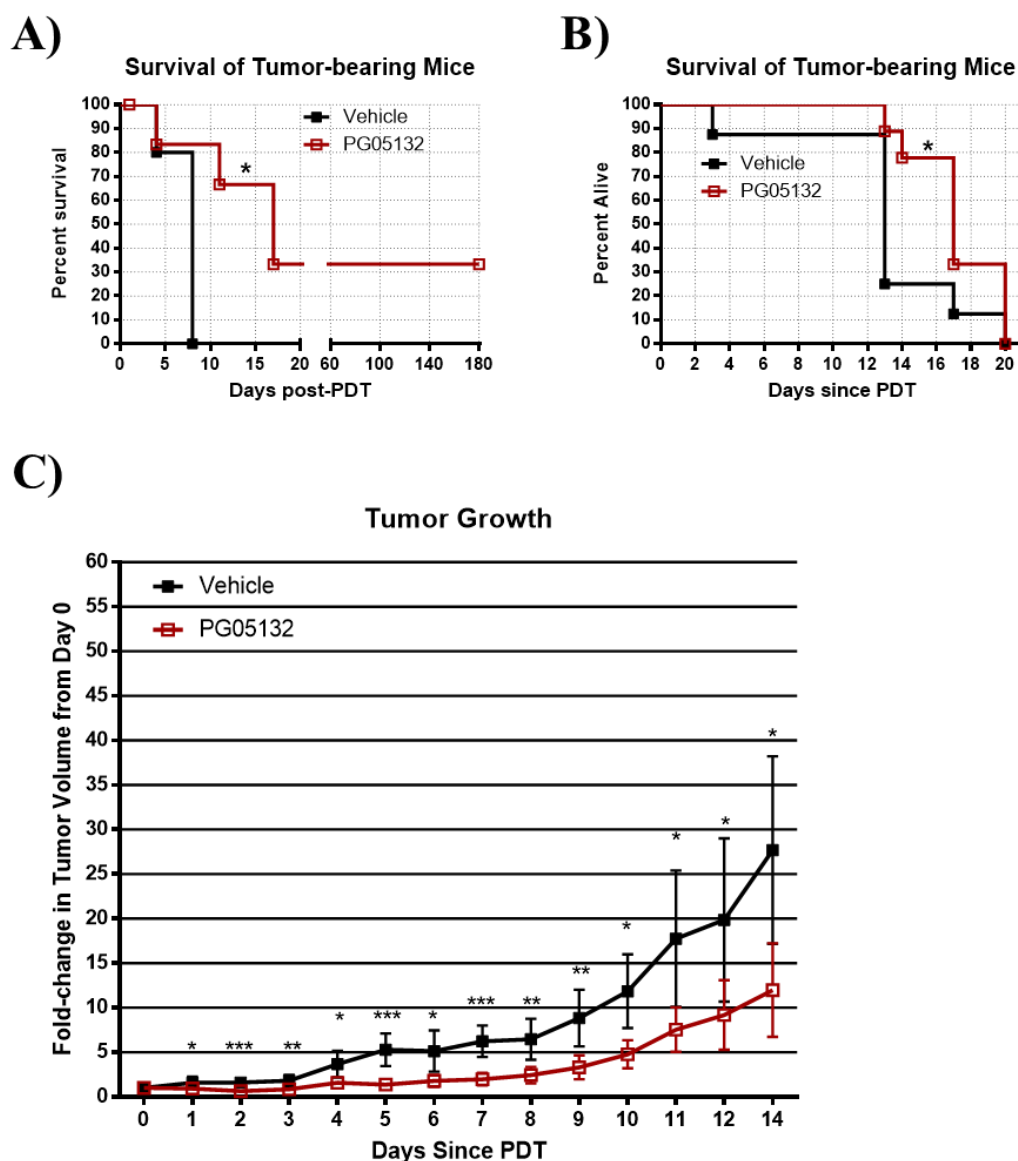


Figure 3.8 Folate-targeted PDT slows tumor growth and improves survival

A-B) Mice with MB49-Luc tumors were subjected to PDT and followed until a humane endpoint was reached or until 6 months post-treatment. Statistical test was Gehan-Breslow-Wilcoxon test, and  $*p < 0.05$ . C) The tumor volume of mice from (B) was calculated daily using measurements taken along perpendicular dimensions with calipers. Error bars represent standard deviation.

Statistical test was student's t-test, and  $*p < 0.05$ ,  $**p < 0.01$ ,  $***p < 0.005$ .

## CHAPTER 4. *IN VIVO* TREATMENT WITH GCL.2, A NUCLEAR HORMONE RECEPTOR MODULATOR, REDUCES TUMOR GROWTH AND MDSC INFILTRATION

### 4.1 Introduction

We initiated this project when our collaborators in the Chopra lab found that a potential repurposed drug for cancer was also predicted to modulate immunity. Briefly, the prediction was made using Computational ANalytics based DOCKing (CANDOCK) to model interactions of the compound, tibolone, with the protein products of a set of differentially expressed genes presumed to be involved in MDSC immunosuppressive function.<sup>236</sup> The list of gene targets was obtained from a gene microarray performed by the Ratliff lab comparing tumor-derived MDSC to their splenic counterparts. (R. Calvert *et al*, manuscript in preparation) Tumor-derived MDSC are immediately suppressive in *ex vivo* assays while splenic MDSC are not, so the differential expression of genes is expected to be associated with acquisition of suppressive function.<sup>117</sup> Tibolone is a nuclear hormone receptor modulator used to treat menopause symptoms.<sup>237</sup> One of its metabolites, GCL.2, mediates the progestogenic and androgenic effects of the parent molecule.<sup>238</sup> Based on its potential targets, GCL.2 is predicted to impact pathways implicated in MDSC expansion. Thus, blocking these pathways could prove beneficial as a cancer immunotherapy. The expansion of MDSC is thought to occur at sites distant to the tumor such as the bone marrow, so it is possible that the cells can be targeted prior to infiltration of the tumor. This circumvents one of the major hurdles in cancer therapy posed by poor penetration of therapeutic molecules into solid tumors.<sup>239</sup> Studies described in Chapter 3 further demonstrate that direct depletion of MDSC and TAM from the tumor may be an inefficient strategy as both populations are rapidly replenished by precursors trafficking into the tumor.

We were initially interested in GCL.2 as a dual therapy molecule that would target both the tumor and the immune response. By using MB49-Luc cells, a GCL.2-insensitive cell line, we could isolate the indirect anti-tumor effects GCL.2 might exert via immunomodulation. The studies in this chapter address the following questions: 1) Does GCL.2 reduce MDSC infiltration of the tumor? 2) Is there any anti-tumor effect associated with GCL.2 treatment *in vivo*? 3) Is T cell function improved as a result of GCL.2 treatment?

### 4.2 Methods

#### 4.2.1 Mice

Female C57BL/6 mice were used in the experiments to take advantage of the immunogenicity of the male-derived MB49-luciferase (Luc) cell line which expresses the male H-Y antigen, a minor histocompatibility antigen.<sup>223</sup> The luciferase-expressing cell line was selected in order to follow

tumor burden over time via bioluminescence imaging. Throughout each experiment, mice were weighed daily and behavior was monitored to assess any adverse effects from drug treatments.

#### 4.2.2 Imaging

Tumor-bearing mice underwent bioluminescence imaging immediately prior to beginning treatment (Day 0) and at indicated timepoints throughout experiments to monitor tumor burden. Mice were injected intraperitoneally (IP) with 15 mg/kg potassium luciferin salt (GoldBio) dissolved in PBS and filter-sterilized. A series of one-minute exposures was collected until the radiance for each mice in the group (photons/sec) had peaked and begun to decline. After imaging on Day 0, mice were randomized into treatment groups using the list randomizer tool at [www.random.org/lists](http://www.random.org/lists). Mice with no tumor burden and mice with much lower or higher burdens than the majority of the cohort were excluded from the study prior to randomization. Mice were considered to have no tumor burden when total abdominal radiance (photons/sec) was similar to the radiance of the chest region where there were no tumor cells. Very high or very low tumor burden as detected by bioluminescence were defined as total abdominal radiance that was an order of magnitude above or below the median for the cohort. Imaging was performed under isoflurane anesthesia using the Spectral AMI instrument in the Bindley Imaging Facility at Purdue University. Images were analyzed using the AMIView software. A schematic of the imaging schedule is shown in Figure 4.1A and the imaging gating is shown in Figure 4.1B.

#### 4.2.3 Drug treatment

GCL.2 was synthesized by the Chopra lab. It is a crystalline solid with limited solubility in aqueous solutions as indicated by the logP<sub>ow</sub> value of 2.85 calculated using ALOGPS 2.1.<sup>240</sup> P<sub>ow</sub> is the partition coefficient which indicates the ratio of solubility in an organic solvent compared to water. Purified GCL.2 is formed as translucent colorless crystals that were crushed to a fine white powder with a mortar and pestle. Unless noted otherwise, drug treatments began three days after tumor cells were injected. For IP injections, we used corn oil as the vehicle since GCL.2 is similar in chemical nature to tamoxifen which is commonly injected IP in corn oil.<sup>241</sup> Solid GCL.2 was dissolved in the vehicle by sonication and overnight incubation. A total volume of 200  $\mu$ L of drug or vehicle was injected twice daily to achieve the indicated daily dose in each experiment. For the oral gavage route of administration a solution of 20% (w/v) hydroxypropyl  $\beta$ -cyclodextrin (HP $\beta$ CD, Sigma) in PBS acidified with 0.12 N HCl was used as the vehicle.<sup>242</sup> HP $\beta$ CD is nontoxic and effectively solubilizes steroid hormones in aqueous solutions.<sup>243</sup> A total volume of 100  $\mu$ L was given once daily. Formulations for oral gavage were prepared freshly with GCL.2 powder each day. A schematic of drug treatment is shown in Figure 4.1A.

#### 4.2.4 Tissue harvest

Peritoneal ascites was recovered using peritoneal lavage with 10 mL of ice-cold PBS. The primary tumor mass, located near the spleen, as well as the spleen, liver, and kidneys were excised using forceps and scissors. Organs were weighed and preserved in 10% neutral-buffered formalin. The tumor tissue was minced with a razor blade and digested using 5 mg/mL collagenase type IV (Gibco) and 100 µg/mL DNase I (Sigma) in complete RPMI-1640 medium by incubating for one hour at 37°C in an orbital benchtop shaker (VWR) set to 100 RPM. Spleens were crushed between frosted microscope slides. Cell suspensions were filtered through 70-µm mesh and RBCs were removed by incubating in hypotonic lysis buffer for 5 minutes at room temperature. Next, cells were resuspended and stained according to Section 2.4 and analyzed by flow cytometry. Figure 4.2 shows the gating strategy for T cells. The gating strategy for myeloid cells is shown in Figure 3.1A.

#### 4.2.5 Organ histology

Organs were fixed for 24 hours in 10% neutral-buffered formalin then transferred to 70% ethanol in water for storage. Tissues were submitted to the Purdue University Histology Research Laboratory for paraffinization, sectioning, and staining with hematoxylin and eosin (H&E).

#### 4.2.5 T cell stimulation

In some experiments, cell suspensions from ascites and tumor were stimulated *ex vivo* to assess cytokine production by T cells. In six-well plates,  $1 \times 10^7$  cells were resuspended in 3 mL of complete RPMI-1640 with stimulation cocktail. The stimulation cocktail consisted of 20 ng/mL phorbol myristate acetate plus 1 µg/mL ionomycin as well as the transport inhibitors brefeldin A (5 µg/mL) and monensin (2µM). The cells were incubated for 5 hours under normal cell culture conditions. Non-adherent cells were collected, stained according to Section 2.4, and analyzed by flow cytometry.

### 4.3 Results

We first assessed the effect of short-term GCL.2 treatment on the overall health of healthy and tumor-bearing mice. We utilized the IP route of administration with once-daily injections of the indicated dose in corn oil vehicle. A single healthy mouse was treated with each indicated dose of GCL.2, and body weights did not differ appreciably from the control (Figure 4.3A); however, there was a slight upward trend in body weight of tumor-bearing mice (n=3 per group) after three days of treatment (Figure 4.3B). The weight-adjusted doses for the two healthy mice were 27 mg/kg (750 mg) and 39 mg/kg (1000 mg). The weight-adjusted doses for the tumor-bearing mice were 30 – 38 mg/kg (750 mg group) and 48 – 51 mg/kg (1000 mg group). In future studies, we used

mg/kg dosing in order to ensure each animal received the same amount of drug relative to body mass. Upon necropsy, there was grossly apparent enlargement of the livers and spleens which reached significance in the tumor-bearing group treated with 1000 mg of GCL.2 (Figure 4.3C). This result was not unexpected given the steroidal nature of GCL.2. The kidney weights were similar in all groups (Figure 4.3C). Interestingly, there were obvious oil droplets in the peritoneal fluid that was likely residual from the corn oil. Throughout these treatments, the mice remained well-groomed, active, and alert.

While harvesting organs and peritoneal ascites during the initial experiment we noted fewer tumor nodules in mice treated with GCL.2 compared to controls. A growth inhibition assay performed by the Chopra lab determined the inhibitory concentration of GCL.2 is greater than 10  $\mu\text{M}$  for MB49-Luc cells *in vitro* which they considered to be insensitive. Thus, we wanted to investigate this potential indirect anti-tumor effect further. First, we tested a few doses of GCL.2 to find a minimal dose at which such an effect could be achieved. We tested 5, 15, and 30 mg/kg given for 10 days beginning on the third day after tumor cells were injected. These were lower weight-adjusted doses than in the previous experiment in order to reduce the steroid-induced side effects. Mice treated with GCL.2 exhibited an increase from pre-treatment body weight (Figure 4.4A), but this was accompanied by a decrease in body condition with apparent abdominal distension. By approximately Day 7, GCL.2-treated mice also exhibited a greasy appearance of their coats. The mice in all four groups began to behave sluggishly by Day 10 though this was likely a result of increasing tumor burden. Higher weights were again noted for livers and spleens in GCL.2-treated mice (Figure 4.4B) though the differences did not reach significance. We observed a reduction in tumor growth rate, based on increase in luminescence, during the first week of treatment. For future studies, we decided to use the 5 mg/kg dose.

We next investigated the impact of GCL.2 on immune cells in tumor-bearing mice. Mice were treated with 5 mg/kg/day of GCL.2 for four days. We again observed a significant increase in liver and spleen weights (Figure 4.5A). In contrast to the previous study, the tumor growth rate was unchanged (Figure 4.5B). We further examined the weight of the primary tumor mass located near the spleen and found it was also not different between treatment groups (Figure 4.5C). On the other hand, as shown in Figure 4.5D, the frequency of M-MDSC in GCL.2-treated mice was reduced in the spleen and slightly reduced in the ascites. Interestingly, the frequency of CD4<sup>+</sup> T cells was reduced in both the spleen and ascites while the frequency of CD8<sup>+</sup> T cells was only reduced in the spleen (Figure 4.5D).

Prior to further study of these potential immunomodulatory effects we decided to change the route of administration and vehicle. Dissolving GCL.2 in corn oil is time-consuming, and corn oil has been shown to cause inflammation when injected intraperitoneally.<sup>244</sup> We decided to utilize once-daily oral gavage as it would be better tolerated than twice-daily injections, and the oral route is more amenable for human patients as well. Murine liver microsome assays to test the stability of GCL.2 were performed by the Chopra lab and 80 – 90% of GCL.2 would be metabolized by the liver. Thus, we selected a dose of 40 mg/kg by oral gavage as that is calculated to result in a

remaining dose of approximately 5 – 10 mg/kg based the liver microsome assays. This was done to maintain some degree of similarity with the experiments using IP administration of GCL.2. We used 20% hydroxypropyl  $\beta$ -cyclodextrin in PBS as the vehicle with the addition of 0.12 N HCl.<sup>242</sup>

Oral gavage treatment of tumor-bearing mice again resulted in significantly increased liver and spleen weights while the kidney weight was unaffected (Figure 4.6A). Histological analysis of the organs revealed some mild changes in the GCL.2-treated mice (personal communication; Meghan Broman, DVM, DAVCP). The kidneys appeared normal (Figure 4.6B, right). There was an increase in the cellularity of the livers with some enlargement of hepatocytes and nuclei consistent with exposure to a steroidal molecule (Figure 4.6C). Finally, there was a small reduction in cellularity in the spleens, but the expected populations were present (Figure 4.6D). There was a significantly smaller increase over time in the tumor burden of GCL.2-treated mice as measured by changes in luminescence (Figure 4.7A). The primary tumors also weighed significantly less (Figure 4.7B). Visually, the extent of tumor luminescence and primary tumor weight corresponded though there were exceptions (Figure 4.8A). Interestingly, there was a correlation between luminescence and primary tumor mass for the GCL.2 group ( $R^2=0.8417$ ) but not for the vehicle group ( $R^2=0.0426$ ) (Figure 4.8B). Finally, we examined the immune cells associated with the tumor ascites and tumor mass. The short tumor growth period in these studies is sufficient for infiltration by clonal populations of T cells, so we examined T cells and myeloid cells.<sup>245</sup> To determine the functional status of T cells we subjected total cell suspensions derived from ascites and solid tumors to non-specific *ex vivo* stimulation with PMA and ionomycin. While the frequency of T cells and IFN $\gamma^+$  T cells in the ascites was unchanged, the frequency of tumor-derived CD4 $^+$  and CD8 $^+$  T cells that could produce IFN $\gamma$  increased in the GCL.2 group (Figure 4.9A). In contrast, changes in MDSC populations were observed in the ascites but not the tumor mass. We were unable to examine G-MDSC in the tumor due to technical problems with detection. For both MDSC subsets in tumor ascites there was a decrease in frequency. Among M-MDSC, the sub-populations expressing the function-associated markers iNOS or PD-L1 were both less frequent in GCL.2-treated mice (Figure 4.9B).

## 4.4 Discussion

Through our collaboration with the Chopra lab we have identified a small molecule that has immunomodulatory properties, making it potentially therapeutic in cancer. GCL.2, which is predicted to interact with molecules involved in MDSC expansion, may act in part by reducing MDSC-mediated immunosuppression. Other attempts to block MDSC expansion include blockade of c-kit signaling in the bone marrow using antibodies or inhibitors such as sunitinib.<sup>53</sup> According to ongoing work in the Chopra lab GCL.2 has the potential to act as a direct anti-cancer agent; however, here we utilized a model that uncouples its immunomodulatory and anti-cancer functions. We observed adverse effects associated with the steroidal nature of GCL.2; however, uncovering the mechanism of its immunomodulatory activity may yield new therapeutic molecules through drug optimization.

Throughout these studies, we observed hepatomegaly and splenomegaly associated with mild histological changes consistent with exposure to a steroid molecule. The GCL.2-treated mice exhibited a decline in body condition despite weight gain and a pot-bellied appearance, suggesting fluid retention. Some nuclear hormones can increase erythropoiesis in the spleen, so the decreased frequency of splenic M-MDSC and T cells may not reflect differences in absolute numbers.<sup>246</sup> It is also possible that trafficking of these cells to/from the spleen was altered by GCL.2. Further study is required to differentiate between these possibilities.

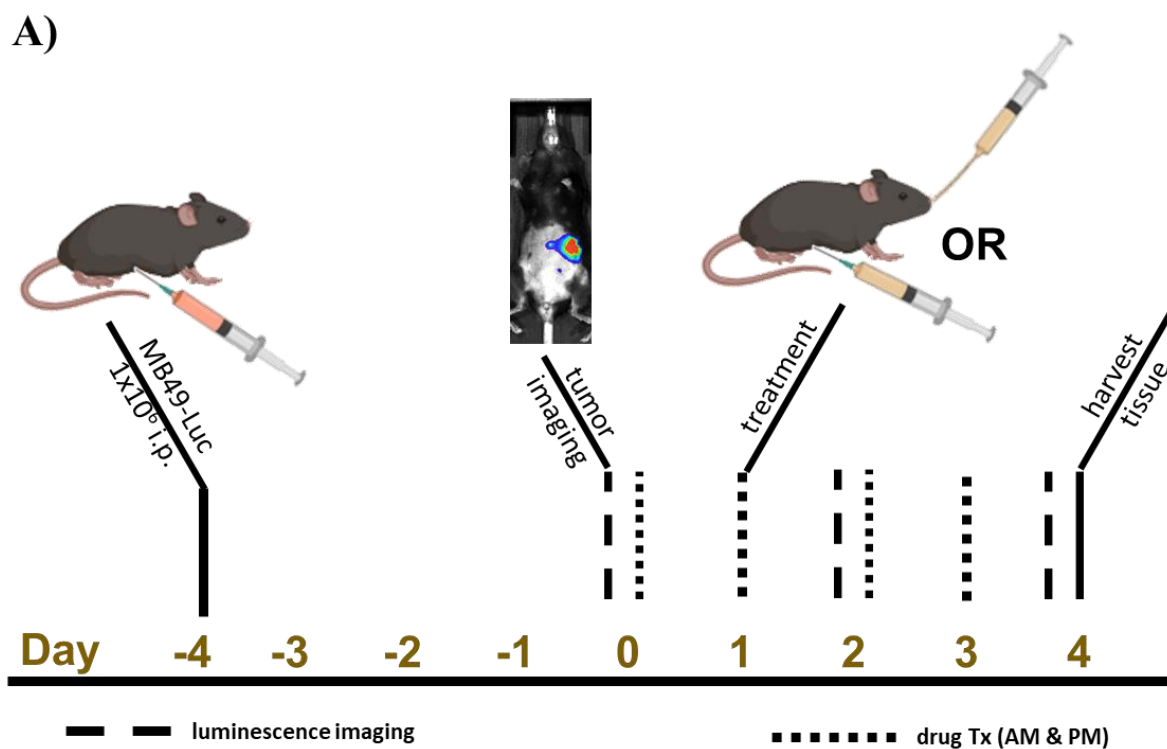
We demonstrated a reduction in the rate of tumor growth as well as in the size of the primary tumor following GCL.2 treatment. This result is encouraging as it is unlikely to be direct anti-tumor action by GCL.2 since MB49-Luc cells are insensitive to it. We recognize that our quantification approaches have limitations and took steps to minimize these as much as possible. In bioluminescence imaging, the light must pass through various organs and tissues as well as skin and hair before reaching the detector. Changes in position of these structures relative to the tumor can alter the quantification from one measurement session to another. Positioning the animals in a reproducible manner at each imaging session can alleviate some of this variation. Additionally, the luciferase reaction requires oxygen and ATP, so changes in tumor oxygenation and viability can drastically alter quantification over time. Early in tumor growth, the correlation between luminescence and tumor size is good; however, large tumors with necrotic regions will not exhibit luminescence in proportion to tumor size.<sup>247</sup> This could explain the lack of correlation between luminescence and tumor size observed for vehicle-treated mice (Figure 4.8B). Measuring the primary tumor mass in this model is inexact as it relies on dissection of the entire tumor mass from the region near the spleen. Though care was taken to do this as completely as possible, it is possible that some tissue was not recovered. Imaging indicated that in a few mice there was another substantial tumor mass elsewhere in the peritoneal space, suggesting that focusing on the most common site of the primary tumor will not capture the bulk of tumor burden in all cases. However, this is a disseminated tumor model, and it would be technically infeasible to attempt to isolate all tumor nodules from the peritoneal space.

We also observed interesting changes in immune cell populations in tumor-associated ascites and in the primary tumor. In the tumor but not in the ascites we observed a higher frequency of IFN $\gamma$ <sup>+</sup> T cells compared to control-treated mice. Since the overall frequency of T cells in the tumor relative to control animals did not change this suggests that immune suppression within the tumor decreased as a result of GCL.2 treatment. On the other hand, neither TAM nor M-MDSC, the more potent suppressive populations, in the tumor mass were changed with GCL.2 treatment. MDSC in the peritoneal ascites were overall less frequent, and fewer iNOS<sup>+</sup> and PD-L1<sup>+</sup> cells were present. The changes in frequency could be due to the interaction between GCL.2 and ROR $\gamma$  such that expansion of the MDSC population was impaired. Further study is required to determine the mechanism underlying this observation as well as its durability over time. The reduced frequency of MDSC expressing functional markers could simply be a consequence of the total population reduction, or GCL.2 may disrupt acquisition of suppressive capacity. We did not directly assay the



suppressive capacity of GCL.2-treated MDSC, and it would be interesting to determine whether that is also affected by GCL.2. Together, the mismatch in location of changes in IFN $\gamma$ <sup>+</sup> T cells and M-MDSC is intriguing. Increased T cell function is expected to accompany a decrease in MDSC frequency and/or function in the same location. It is possible that though functional molecules are expressed by MDSC their activity is impaired. Another possibility is that the spatial relationship between T cells and MDSC in the tumor and ascites might alter their interactions. We have not performed any immunohistochemical analyses of the MB49-Luc tumors to determine whether they correspond to the “hot” T cell-infiltrated or “cold” T cell-excluding immunophenotype. If T cells are confined to the periphery of the tumor they may be in closer proximity to MDSC in the ascites than to those in the tumor.

We encountered some limitations in the course of these studies that would require optimization in any future studies. First, the solubility of GCL.2 in biologically compatible buffers is not ideal. Though care was taken to produce uniform suspensions this could have resulted in variability of the actual amount of drug administered to the mice within and between experiments. Another problem we encountered is the nature of the compound itself. The adverse effects of steroidal drugs, such as hepatomegaly and fluid retention, are well-known and dose-limiting, often requiring a tapered dosing regimen as with prednisone. This is in contrast to the constant dose regimen used in our studies. Finally, the particular clone of MB49 from which the MB49-Luc line used in these experiments was generated is highly aggressive *in vivo* and severely limits the length of tumor therapy studies. Moreover, the aggressiveness of the tumor model likely leaves a very limited window during which to intervene therapeutically.



B)

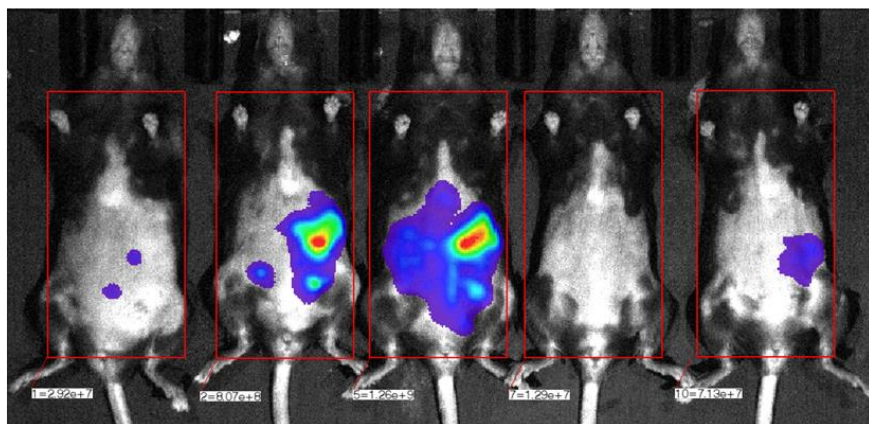


Figure 4.1 In vivo imaging and GCL.2 treatments

A) Experimental schematic of GCL.2 studies. B) Example of gating in AMIView to quantify tumor burden via bioluminescence imaging. Graphics created with BioRender.com.

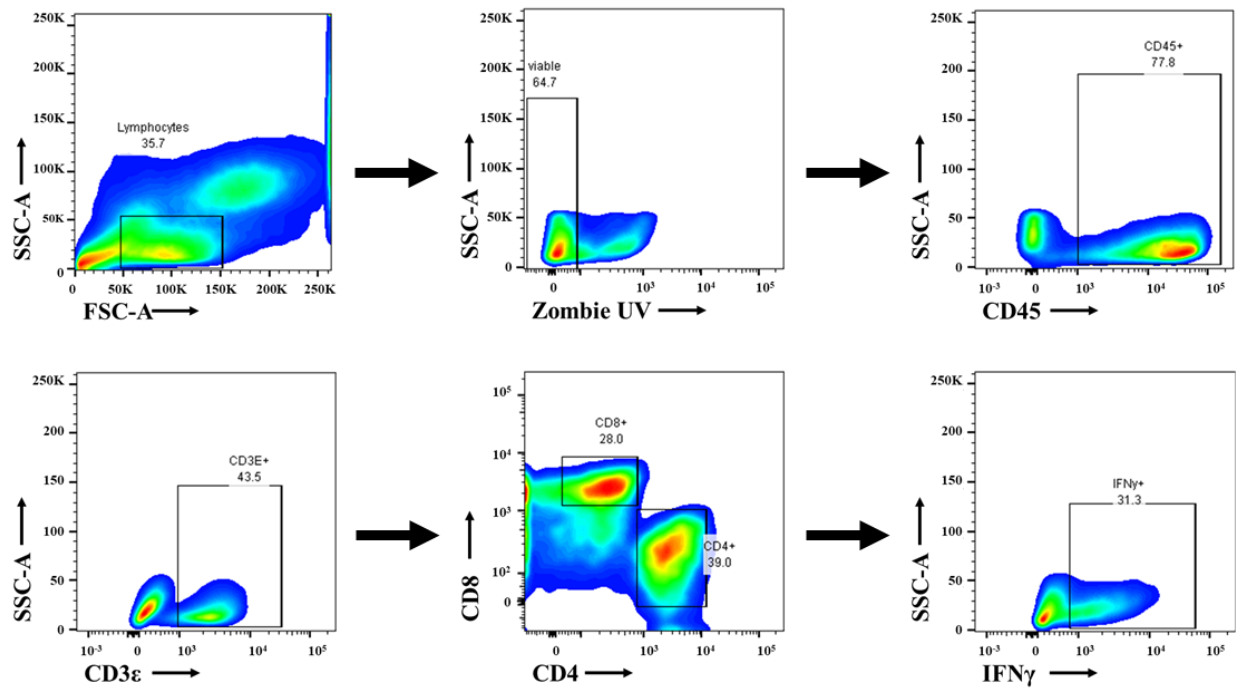


Figure 4.2 FACS gating strategy of T cells in the peritoneal MB49-Luc tumor model

A) Representative plots show hierarchical gating strategy to exclude debris and focus on lymphocytes ( $\text{SSC-A}^{\text{low}}$   $\text{FSC-A}^{\text{low}}$ ) and exclude dead cells ( $\text{Zombie UV}^{\text{neg}}$ ) from leukocytes ( $\text{CD45}^+$ ) followed by inclusion of  $\text{CD3}\epsilon^+$  cells.  $\text{CD8}^+$  and  $\text{CD4}^+$  T cells were gated from within that population.  $\text{IFN}\gamma$ -expressing cells were gated within the T cell subpopulations

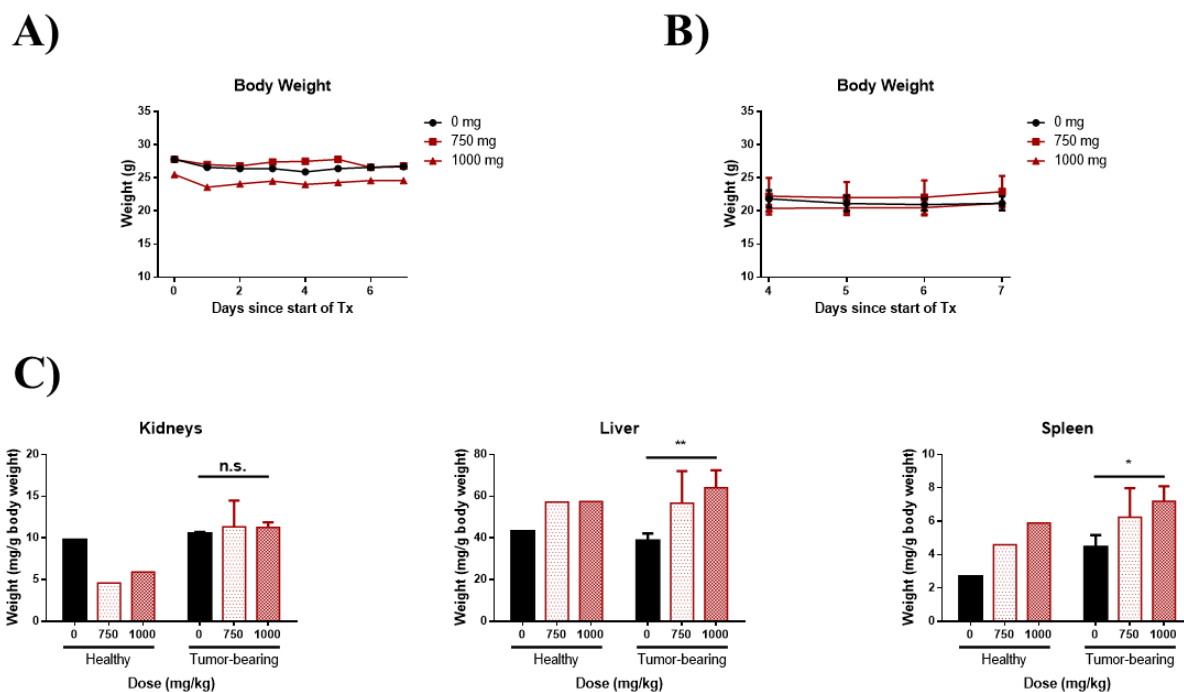


Figure 4.3 Liver and spleen weight increases in healthy and tumor-bearing mice treated with GCL.2

Mice were treated with the indicated dose of GCL.2 in a total volume of 200  $\mu$ L corn oil vehicle via IP injection once daily. Error bars are standard deviation. Statistical test is two-tailed Student's *t-test*, and \* $p < 0.05$ , \*\* $p < 0.01$ . A) Body weights of healthy mice ( $n=1$  per group) treated for 7 days with GCL.2. B) Body weights of tumor-bearing mice ( $n=3$  per group) treated for 3 days with GCL.2. C) Organ weights of healthy and tumor-bearing mice at necropsy

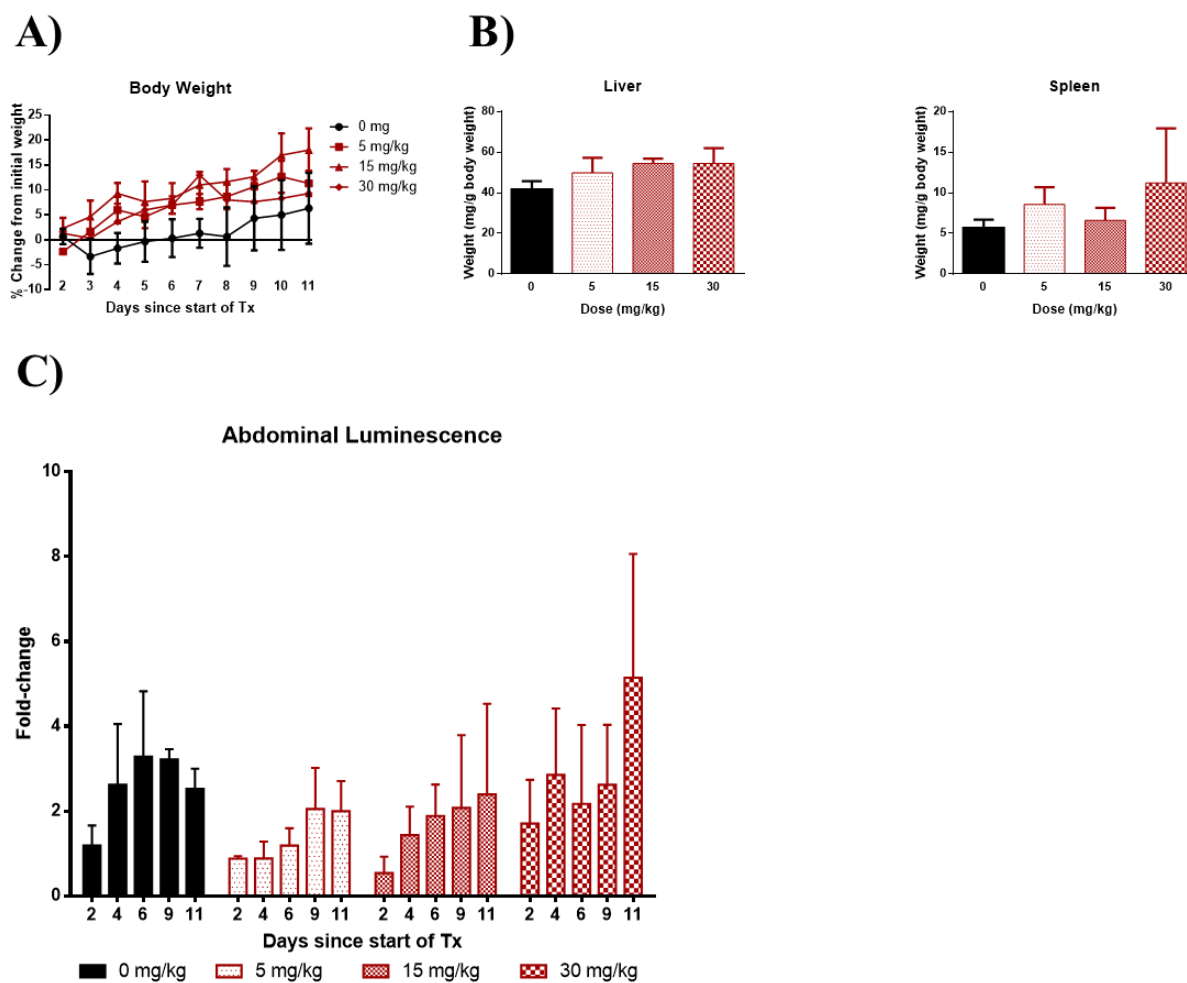


Figure 4.4 GCL.2 slows the rate of early tumor growth *in vivo*

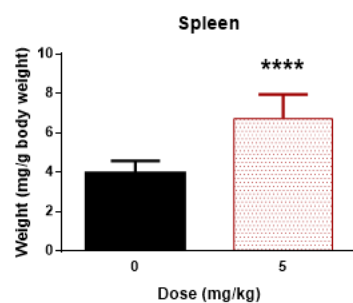
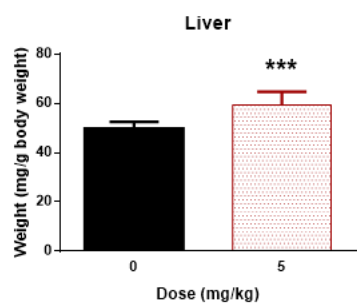
MB49-Luc tumor-bearing mice (n=3 per group) were treated with the indicated daily dose of GCL.2 in corn oil vehicle via IP injection for 10 days. Bioluminescence imaging was carried out on Day 0 and at the indicated timepoints during treatment to assess tumor burden. Error bars are standard deviation. A) Body weights of mice. B) Organ weights at necropsy. C) Change in abdominal luminescence at indicated timepoints calculated from baseline measurement on Day 0

Figure 4.5 GCL.2 administered by IP injection route does not impact tumor growth but does alter immune cell frequencies

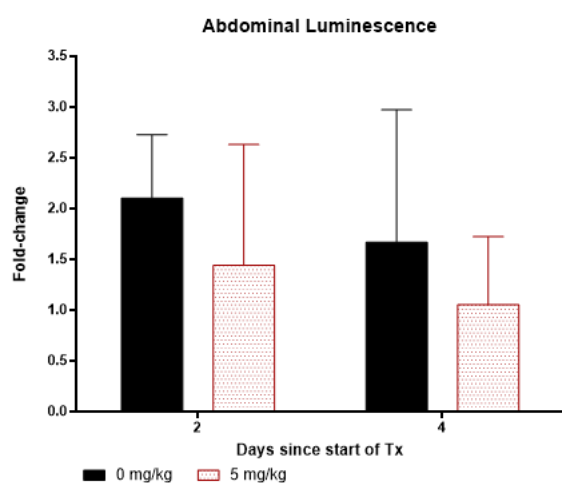
MB49-Luc tumor-bearing mice were given the indicated daily dose of GCL.2 in corn oil vehicle by IP injection for 4 days. Bioluminescence imaging was performed on Days 0, 2, and 4 to assess tumor burden. Data represent two independent experiments with a total of n=7 (0 mg/kg) and n=6 (5 mg/kg) mice per group. Cells from mice in each treatment group within an experiment were pooled for FACS analysis. Error bars are standard deviation. Statistical test is two-tailed Student's *t*-test, and \*\*\* $p < 0.005$ , \*\*\*\* $p < 0.001$ . A) Organ weights at necropsy. B) Change in abdominal luminescence at indicated timepoints calculated from baseline measurement on Day 0. C) Weights of primary tumors. D) FACS analysis of leukocytes in spleen and peritoneal ascites. Ratios are calculated as 5 mg/kg:0 mg/kg groups from frequencies in CD45+ gate.

Dashed lines represent no change compared to 0 mg/kg group.

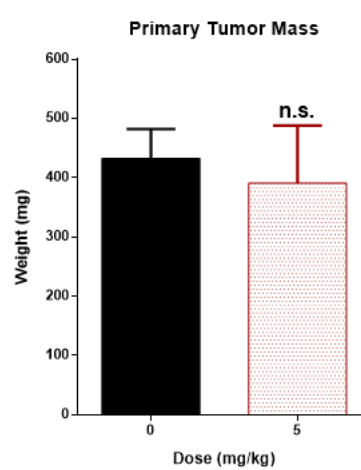
A)



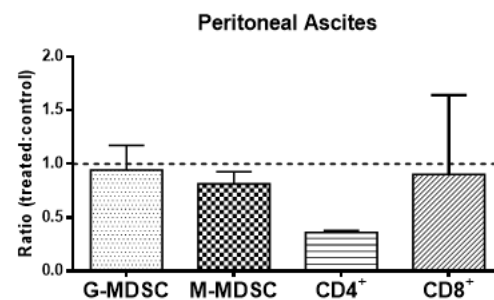
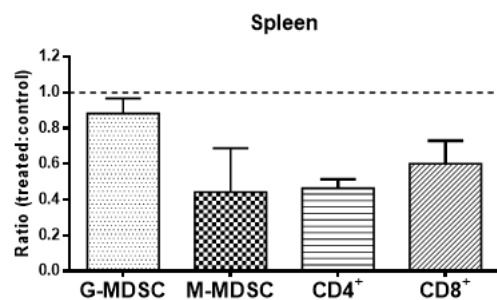
B)



C)



D)



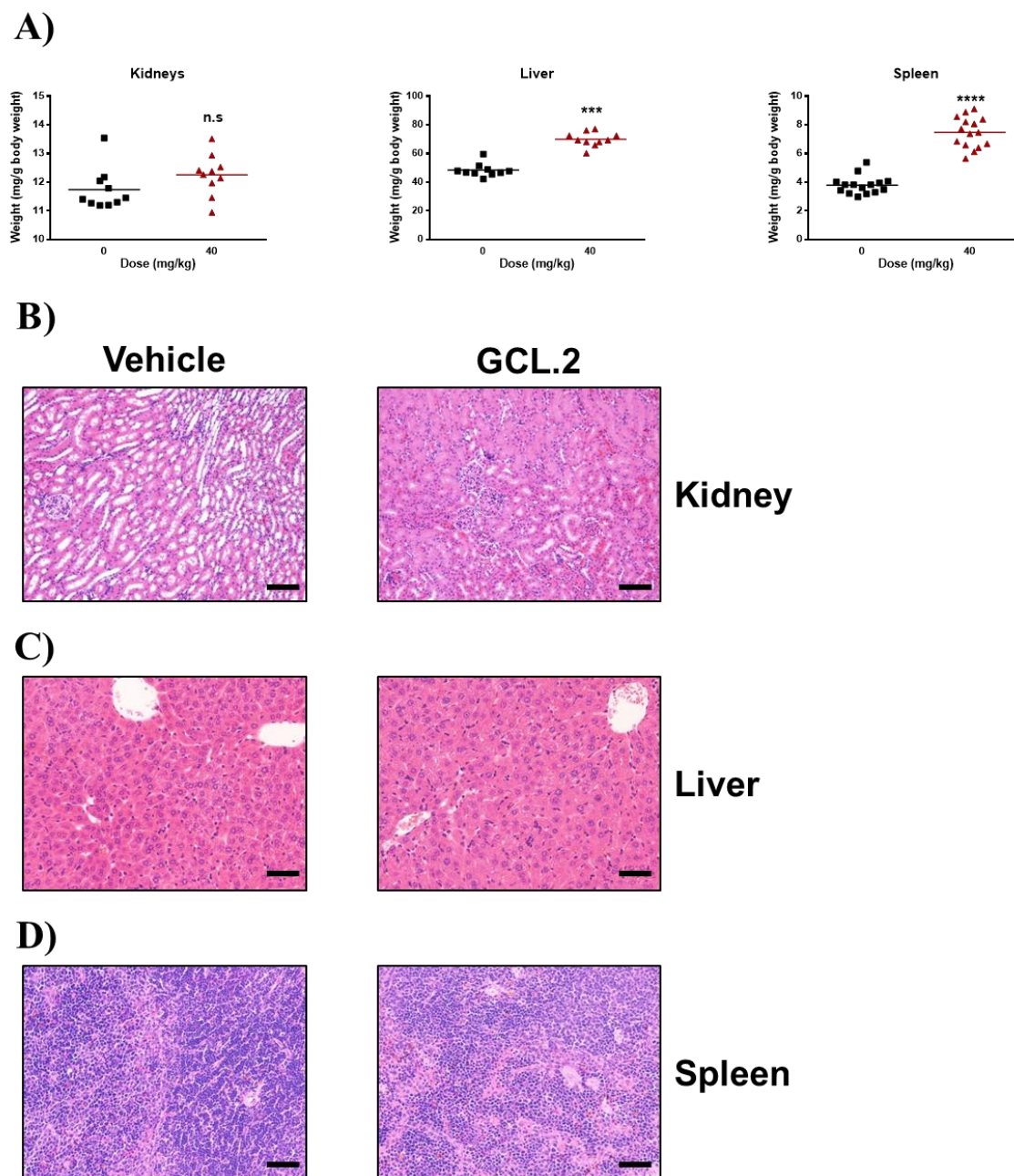


Figure 4.6 GCL.2 increases liver and spleen weight and induces mild histological changes

MB49-Luc tumor-bearing mice were given the indicated dose of GCL.2 by oral gavage for 4 days. Organ weight data represent three independent experiments with a total of  $n=15$  mice per group. H&E-stained images of kidney, liver, and spleen are representative of vehicle (left) and GCL.2-treated (right) mice. Scale bars are 100  $\mu\text{m}$  (kidney; 100X magnification) or 50  $\mu\text{m}$  (liver and spleen; 200X magnification). Statistical test is two-tailed Student's t-test, and \*\*\*\* $p<0.0005$ , \*\*\* $p<0.001$ .



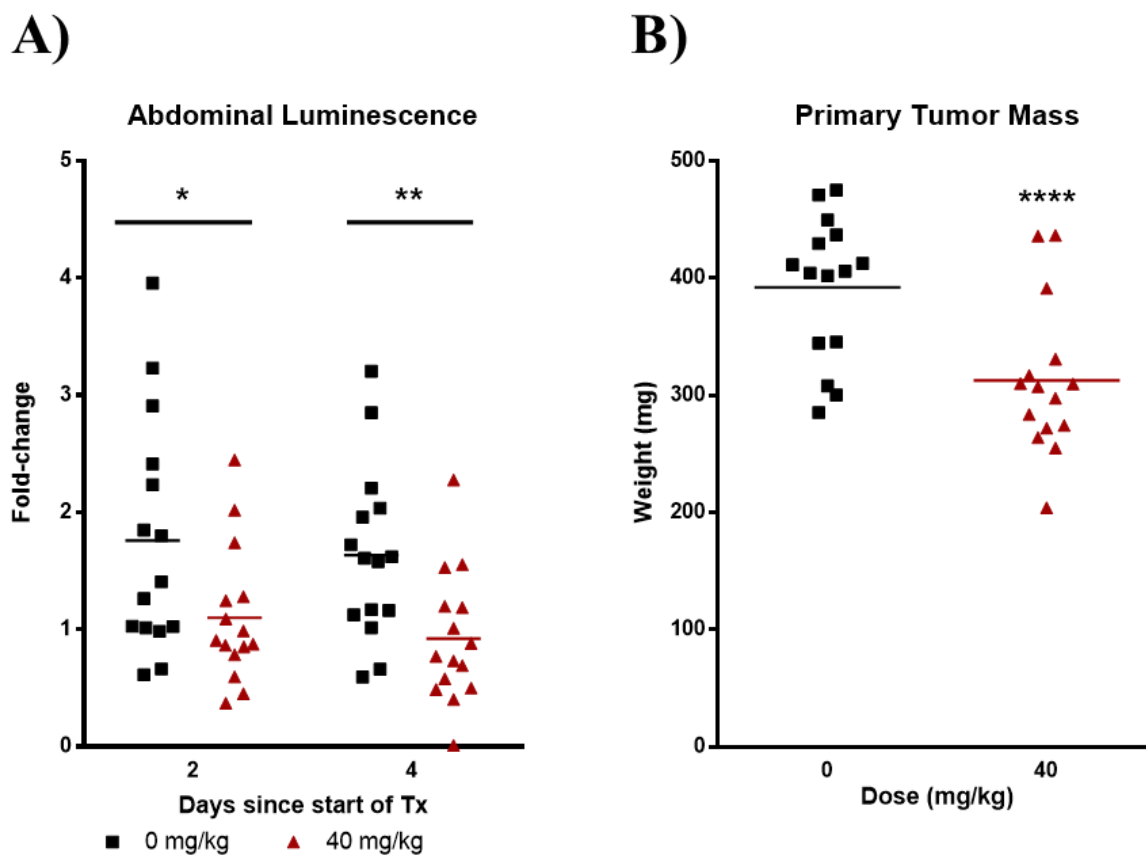


Figure 4.7 GCL.2 administered by oral gavage route slows tumor growth and reduces primary tumor weight

MB49-Luc tumor-bearing mice were given the indicated dose of GCL.2 by oral gavage for 4 days. Bioluminescence imaging was performed on Days 0, 2, and 4 to assess tumor burden. Data represent three independent experiments with a total of  $n=15$  mice per group. Mice within an experiment were pooled for FACS analysis. Statistical test is two-tailed Student's  $t$ -test, and \* $p<0.05$ , \*\* $p<0.01$ , \*\*\* $p<0.005$ , \*\*\*\* $p<0.001$ . A) Organ weights at necropsy. B) Change in abdominal luminescence at indicated timepoints calculated from baseline measurement on Day 0. C) Weights of primary tumors.

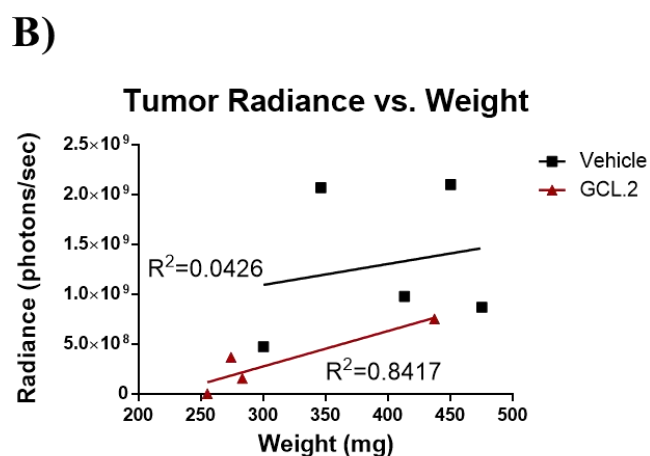
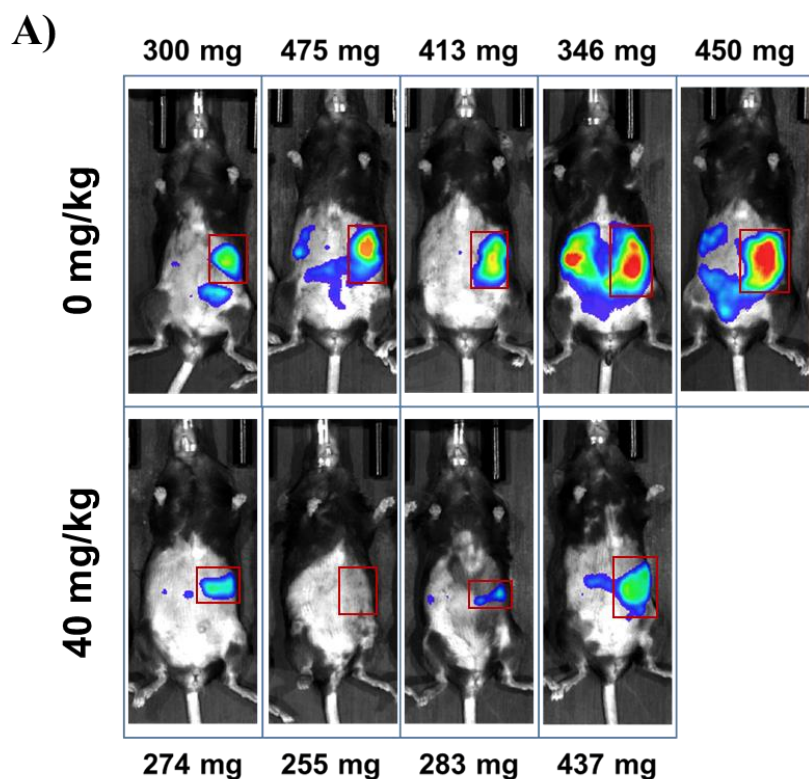


Figure 4.8 Bioluminescence in the primary tumor location correlates with tumor weight

A) Representative luminescence images of tumor-bearing mice after 4 days of treatment (radiance in photons/sec). Weight of primary tumor is shown above/below image. Red boxes correspond to the approximate region of the primary tumor mass and where radiance was measured to (B) compare radiance with tumor weight.

A)



B)

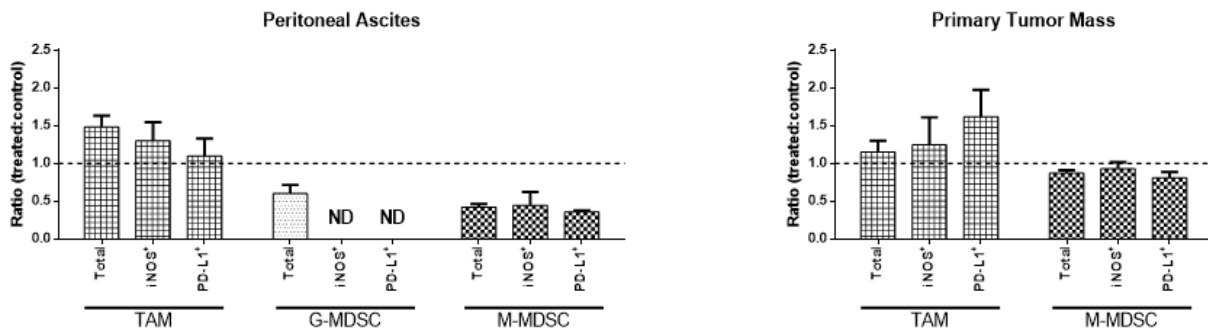


Figure 4.9 GCL.2 treatment increases the frequency of IFN $\gamma$ <sup>+</sup> T cells in the primary tumor and reduces the frequency of MDSC in the tumor ascites

MB49-Luc tumor-bearing mice were given the indicated dose of GCL.2 by oral gavage for 4 days. Data represent two independent experiments with a total of n=11 (0 mg/kg) and 10 (40 mg/kg) mice per group. Mice within an experiment were pooled for FACS analysis. Error bars are standard deviation. A) FACS analysis of T cells in peritoneal ascites and primary tumor. Ratios are calculated as 40 mg/kg:0 mg/kg groups from frequencies in CD45<sup>+</sup> gate. Dashed lines represent no change compared to 0 mg/kg group. B) FACS analysis of myeloid cells in peritoneal ascites and primary tumor. Ratios are calculated as 40 mg/kg:0 mg/kg groups from frequencies in CD45<sup>+</sup> gate. Dashed lines represent no change compared to 0 mg/kg group.

## CHAPTER 5. DEVELOPMENT OF A MACHINE LEARNING APPROACH TO IDENTIFY NOVEL CELL-SPECIFIC IMMUNOMODULATORS OF SUPPRESSIVE MYELOID CELLS IN THE TME

### 5.1 Introduction

Presently, there is a dearth of MDSC-specific drugs currently available in the clinic. In Chapter 4, we showed that GCL.2 exerts some immunomodulatory effects in a mouse model of cancer. Unfortunately, it is a steroidal molecule that can be toxic during long-term treatment, making GCL.2 less desirable as a potential clinical therapeutic. Therefore, we continued our collaboration with the Chopra lab in order to identify novel non-steroidal drugs that reduce MDSC-mediated immunosuppression in cancer. One of the hurdles in drug discovery for MDSC is the infeasibility of applying current screening techniques to this population. High-throughput screening (HTS) requires large quantities of cells, and this is not possible for tumor-derived MDSC. Utilizing immortalized cell lines to approximate MDSC for large screens may not fully capture the complexity of cells isolated directly from the TME. Assay miniaturization can partially address the difficulty in obtaining enough cells for HTS but depends upon the limit of detection for the assay utilized in the screen. A second problem with HTS is the very low percentage of “hits” obtained from screening thousands of compounds.<sup>248,249</sup> Virtual screens in which computer modeling narrows the library to compounds likely to bind the target molecule can be used to improve the low hit rate.<sup>250</sup> This requires knowledge of the target, though, and the biology of MDSC and range of potential therapeutic targets is not fully understood. Focusing only on currently known targets could hinder the discovery of new ones. Finally, even drugging a specific molecule or type of molecule does not guarantee specificity to the target cell. For example, NOS inhibitors targeting NO production, a key mechanism of M-MDSC-mediated suppression, have been tested clinically, but lack specificity for myeloid cells, leading to unacceptable toxicity.<sup>215</sup> An ideal screening approach would allow efficient identification of compounds with activity against a diverse array of targets and that are tailored to the cell population of interest.

To address the difficulty of identifying and testing new compounds we utilized an MDSC-specific gene expression array for protein-compound interaction modeling and machine learning methods developed in the Chopra lab. Importantly, unlike traditional HTS, this method can immediately incorporate experimental data to refine additional predictions prior to continuing the screening process. For these studies, a list of approximately 3000 protein targets putatively overexpressed in the M-MDSC subset was derived from a gene array previously performed by the Ratliff lab (R. Calvert *et al*, manuscript in preparation). The gene array was performed using MDSC subsets isolated from the peritoneal ascites of a tumor-bearing mouse as well as MDSC subsets isolated from the spleen of POET3 mouse that had been inflamed with OT-I cells with the intention of analyzing differential gene expression between the two anatomical sites. Previous work by Haverkamp *et al* demonstrated that MDSC from the inflammatory site are immediately active *ex*

*vivo* whereas the splenic counterparts require stimulation prior to acquisition of suppressive function.<sup>117</sup> Thus, changes in gene expression between the sites may indicate genes involved in suppression. The gene array yielded 6,328 genes that were differentially expressed in both subsets, and there were an additional 2,070 and 2,973 differentially expressed genes that were unique to the G-MDSC and M-MDSC subsets, respectively. We were primarily interested in the M-MDSC subset, so our collaborators in the Chopra lab applied a set of selection criteria to the gene array in order to generate a list of potential targets important for M-MDSC suppressive function. Briefly, the targets selected were significantly upregulated ( $p < 0.05$ , fold-change  $> 1$ ) in tumor-derived M-MDSC when compared to splenic M-MDSC. This list was further refined by removing genes that did not correspond to an expressed protein and/or that lacked a human homolog. All targets were required to be available in the Computational ANalytics of Novel Drug repurposing Opportunities (CANDO) database and have a ligand binding site that could be used to model docking of compounds. Finally, all targets on the final list either have a solved crystal structure deposited in the protein databank (PDB) or can be modeled *in silico* in order to simulate docking of compounds with the protein's ligand binding pocket.<sup>251–255</sup> This yielded a final list of 2,971 targets that were subsequently used to model interactions via the Computational ANalytics based DOCKing (CANDOCK) algorithm with 762 compounds consisting mostly of synthetic molecules designed by the Chopra lab<sup>236</sup>. The result was an interaction profile for each compound against the entire set of potential targets.

The machine learning model used in these studies utilizes the interaction profiles from CANDOCK and a set of training data. The training data consist of a binary “active” or “inactive” designation for each compound in an initial set based on performance in an *ex vivo* assay. The model then attempts to determine which characteristics of the interaction profiles define an “active” versus an “inactive” compound. It can then make predictions for additional “actives” from among the remaining untested compounds based on the interaction profiles of those compounds. To strengthen the model, the experimentally determined activity designations from each additional round of testing are added to the original set of training data. Thus, with each iteration of prediction and testing the model can focus more narrowly on the common characteristics of the interaction profiles associated with active compounds.

This chapter describes the validation of a machine learning-based method for identifying novel compounds that abrogate the immunosuppressive phenotype of myeloid cells exemplified by NO production. To accomplish this, we utilized *ex vivo* assays to screen predicted compounds and refine subsequent predictions made via additional iterations of the machine learning model. To more fully capture the spectrum of suppressive myeloid cells in the TME we studied tumor-derived Ly6C<sup>+</sup> Ly6G<sup>neg</sup> cells rather than a pure population of M-MDSC. We expect there is sufficient similarity in the suppressive mechanisms of M-MDSC and other monocytic cells that the array data can be extrapolated to a broader Ly6C<sup>+</sup> Ly6G<sup>neg</sup> population. We chose NO production as the target phenotype for its key role in immunosuppression. We hypothesized that focusing on modulating NO production rather than directly and specifically inhibiting iNOS may lead to the

discovery of additional functional targets. We also believe broadening the cell population and target phenotype under study will lead to identification of compounds with greater universality among types of cancer and among patients. Key questions addressed in this work include 1) Does the accuracy of the machine learning model improve with the input of experimental data? 2) Is it possible to modulate a phenotype without deliberately selecting compounds that target known components of the functional pathway? 3) Do active compounds identified in the *ex vivo* assay also exhibit activity *in vivo*?

## 5.2 Methods

### 5.2.1 Mouse models and cell isolation

To maintain consistency among the experiments in these studies we used prostate ovalbumin-expressing transgenic 3 (POET-3) mice between 12 and 14 weeks of age for all experiments. The POET-3 mouse is on a C57BL/6 background and carries a transgene under the control of a modified probasin promoter (ARR<sub>2</sub>PB) to drive high-level expression of an ovalbumin-transferrin receptor fusion protein on the surface of prostate epithelial cells. Tissue damage and inflammation occur following adoptive transfer of ova-specific CD8<sup>+</sup> OT-I T cells.<sup>256,257</sup> This model allows the study of acute inducible autoimmune prostate inflammation characterized by infiltration of T cells, MDSC, macrophages, and neutrophils.<sup>258</sup> Female POET-3 mice can be considered as wild-type C57BL/6 mice since the prostate is a male-specific organ. Additionally, in the absence of OT-I cells, male POET-3 mice of the approximate age used in these studies have a very low level of CD45<sup>+</sup> cell infiltration of the prostate.<sup>259</sup> For tumor studies, we thus considered the level of spontaneous background inflammation to be negligible.

Mice were injected intraperitoneally with MB49-Luc cells to generate tumors and recruit suppressive myeloid cells for study. In male mice, 1x10<sup>6</sup> cells were injected while 5x10<sup>5</sup> cells were injected into female mice. For *ex vivo* studies, tumors were allowed to grow for seven days. For *in vivo* treatment studies, mice were subjected to bioluminescence imaging as described in Section 4.2.2. As the purpose of imaging was to detect but not quantify tumor burden only five one-minute exposures were collected. For all experiments, tumor ascites was recovered seven days after tumor cell injection via peritoneal lavage with 10 mL of ice-cold PBS.

For the benign inflammation model, male POET-3 mice were injected retro-orbitally with 5x10<sup>6</sup> OT-I cells that had been pre-activated for 48 hours as described below. Prostate tissue from all four lobes was harvested 6 days after inflammation was initiated. The tissue was digested and prepared for FACS analysis as described in Section 2.4.

For suppression assays, RAG1<sup>-/-</sup> OT-I mice (a kind gift from Dr. William Heath, University of Melbourne) were used to isolate ova-specific CD8<sup>+</sup> OT-I T cells from spleens.<sup>257</sup>

### 5.2.2 OT-I cell activation

CD8<sup>+</sup> OT-I cells were isolated by crushing the spleens from RAG1<sup>-/-</sup> OT-I<sup>+</sup> mice between frosted slides and rinsing with PBS. Cells were then filtered through 70- $\mu$ m mesh and red blood cells were removed by treatment with lysis buffer. The cells were then resuspended in RPMI-1640 and plated at  $1 - 2 \times 10^6$ /well in a 24-well plate with 2 mL of medium supplemented with 55  $\mu$ M beta-mercaptoethanol and 1  $\mu$ g/mL SIINFEKL peptide (Genscript, USA). For suppression assays, a 24-hour pre-activation with  $2 \times 10^6$  cells per well was used while a 48-hour pre-activation with  $1 \times 10^6$  cells per well was used to inflame POET-3 mice.

### 5.2.3 MACS enrichment of Ly6C<sup>+</sup> Ly6G<sup>neg</sup> cells

Cell isolated from tumor ascites were incubated with red blood cell lysis buffer for 5 minutes at room temperature and washed with PBS. Next, cells were resuspended at  $1 \times 10^8$ /mL in PBS and incubated with a 1:250 dilution of Fc block for 10 minutes at 4°C. Fluorescent antibodies against Ly6G (PE) and Ly6C (FITC) were added at final dilution of 1:1000 and incubated for 15 minutes at 4 °C. Cells were then washed with PBS and centrifuged at 300xg for 5 minutes. Miltenyi MACS columns were used according to manufacturer's instructions to sequentially deplete Ly6G<sup>+</sup> cells and enrich Ly6C<sup>+</sup> cells. Briefly, cells were resuspended at  $1 \times 10^8$ /mL in MACS buffer (Miltenyi) and anti-PE microbeads were added to a final dilution of 1:10. The cells were incubated for 15 minutes at 4°C and then washed with PBS as above. Cells were then resuspended in MACS buffer and applied to either LS (*ex vivo* assays) or MS (*in vivo* assays) columns. Cells in the flow-through and column washes were treated as before but using anti-FITC microbeads. After incubation and washing, the cells were again applied to columns. A schematic of this process is shown in Figure 5.1B. Cells eluted from the columns were then used in experiments or analyzed by FACS.

### 5.2.4 *Ex vivo* compound treatments

All compounds for *ex vivo* screening were provided by the Chopra lab as 10 mM stocks in dimethyl sulfoxide (DMSO). Compounds synthesized by the Chopra lab are designated with the prefix "GCL." or "JMGC02S". MACS-enriched Ly6C<sup>+</sup> cells were used for *ex vivo* compound screening and validation experiments. Cells were plated at  $2 \times 10^5$ /well in a 96-well flat-bottom plate in a total volume of 200  $\mu$ L of complete RPMI-1640. Compounds were added to a final concentration of 100 nM except where specified otherwise, and the medium was supplemented to 20% tumor explant supernatant (TES) made from EL-4 cells as previously described and 20 ng/mL of recombinant murine GM-CSF (Peprotech).<sup>260</sup> Cells were incubated at 37°C for 18 hours under hypoxic conditions (1% O<sub>2</sub>, 5% CO<sub>2</sub>) before being returned to normoxic conditions for an additional six hours to allow sufficient nitrites to form for detection via Griess assay.<sup>261</sup> A diagram outlining the *ex vivo* experiment process is shown in Figure 5.1A.

### 5.2.5 Griess assay

Cell culture supernatants from triplicate wells in *ex vivo* assays were collected after centrifugation at 500xg for 3 minutes to remove cells. Nitrites in the supernatant were used as an indirect measurement of NO and were quantified using the Promega Griess Assay kit according to the manufacturer's instructions. The reactions were incubated for 5 minutes. Nitrite standards were diluted in complete RPMI-1640. A Multiskan FC plate reader (Thermo Scientific) was used to quantify the colorimetric assay at 570 nm. Nitrite concentrations were normalized to the total RNA concentration from the same wells (see section 5.2.6) to account for any differences in cell numbers among wells.

### 5.2.6 Gene expression

To isolate RNA for gene expression analysis cells were harvested from triplicate wells by centrifugation at 300xg for 3 minutes and supernatants were removed. The EZNA Total RNA Kit I (Omega Biotek) was used according to manufacturer's instructions to lyse cells and isolate RNA. All samples were subjected to one freeze-thaw cycle at -20°C in the provided lysis buffer prior to continuing RNA isolation. Eluted RNA was quantified using a Nanodrop 2000. Isolated RNA was subsequently used for cDNA synthesis prior to long-term storage at -80°C.

For cDNA synthesis, 50 – 100 ng of RNA was added to a 20 uL reaction using a Bioer GenePro thermal cycler. The reaction mixture consisted of 250µM dNTPs (Amresco), 0.5 µM random hexamers (Promega), 0.5 µM oligo(dT)15 primers (Promega), 10 units of murine RNase inhibitor (NEB), and 200 units of M-MuLV reverse transcriptase combined in the included 10X reaction buffer (NEB). The following PCR program was utilized: 25°C for 5 minutes, 42°C for 30 minutes, 85°C for 5 minutes, 4°C hold.

Relative gene expression was analyzed using real-time quantitative polymerase chain reaction (RT-qPCR) in a Roche Lightcycler 96 machine with PrimeTime qPCR probes (Integrated DNA Technologies). For the reactions, we used PerfeCTa FastMix II (Quanta Biosciences) according to the manufacturer's instructions with probes for genes of interest as well as for the housekeeping gene 18s (ThermoFisher Scientific) as an internal reference. All reactions were set up as duplicate wells. Relative gene expression was calculated using the formula  $2^{-[Ct(\text{gene})-Ct(18s)]}$  where Ct refers to the threshold cycle number given by the instrument. The following PrimeTime probes for mouse genes were used: Mm.PT.58.43705194 (*Nos2*), Mm.PT.58.41471408 (*Cd274*), Mm.PT.58.42405698 (*Folr2*).

### 5.2.7 In vivo drug treatments

The synthetic compound JMGC02S81 was provided by the Chopra lab. It was dissolved at 100 mg/mL in a vehicle composed of 20% hydroxypropyl β-cyclodextrin (Sigma) in PBS. After



imaging, tumor-bearing mice were randomized into treatment groups using the list randomizer tool at [www.random.org/lists](http://www.random.org/lists). Mice with very high or low tumor burden compared to the rest of the cohort were excluded (see Section 4.2.2 for criteria). Inflamed POET-3 mice were randomized into treatment groups without any imaging. In all studies, mice were treated with 100 mg/kg/day by once daily oral gavage. Daily treatments were freshly diluted from the 100 mg/mL stock each day. Mice given the vehicle were gavaged with 100  $\mu$ L of the vehicle only. Mice were weighed and observed daily in order to monitor overall health. Schematics for *in vivo* experiments with tumor-bearing and inflamed POET-3 mice are shown in Figure 5.2A and 5.2B, respectively.

### 5.2.8 T cell suppression assay

We used a short-term *ex vivo* T cell suppression assay developed in the Ratliff lab to assess myeloid cell suppressive activity.<sup>117</sup> Tumor-derived myeloid cells and pre-activated OT-I cells were co-cultured in RPMI-1640 with 1  $\mu$ g/mL SIINFEKL peptide. Myeloid:OT-I cell ratios of 1:1, 1:2, 1:4, and 1:8 were used. A total of  $1 \times 10^5$  OT-I cells were added per well in a 96-well plate while the number of myeloid cells varied. Where indicated, 200  $\mu$ M L-NMMA was added to inhibit NO production in the co-culture. Co-cultures were incubated for 17 hours under hypoxic atmosphere, defined as 1% O<sub>2</sub> and 5% CO<sub>2</sub>, before EdU was added and incubated for another hour prior to beginning the EdU detection protocol. Where indicated, cell supernatants were collected for nitrite quantification. T cell proliferation was quantified using a Click-iT EdU Cell Proliferation kit (Thermo Fisher Scientific) according to manufacturer's instructions. EdU incorporation was quantified by flow cytometry.

## 5.3 Results

The list of targets referenced above is assumed to be associated with the acquisition of M-MDSC suppressive capacity in the TME. As such, we needed to select a parameter by which to evaluate the performance of the compounds. We chose the iNOS pathway because it is central to M-MDSC function, and we measured *Nos2* expression and nitric oxide production after *ex vivo* treatment with compounds. Next, the machine learning model was trained and iteratively refined with experimental data in order to improve subsequent predictions based on compound-proteome interactions and measured activity. Ultimately, compounds designated as active were validated using *ex vivo* and *in vivo* assays. The various phases of this process are summarized in Figure 5.3.

We first tested a set of seven existing drugs and three synthetic molecules in Round 0. Table 5.1 contains all tested compounds. All compounds have favorable interaction profiles but were predicted from the array without the input of any experimental data. So-called "active" compounds were defined with minimal stringency as those inducing a mean reduction in *Nos2* expression or NO production to at most 90% of the vehicle. Using these criteria, we identified four compounds active against at least one of the targets (green columns in Figure 5.4). Only nicotine was active against both *Nos2* expression and NO production. Data from four active and six inactive

compounds (failed to reduce both *Nos2* and NO production) were submitted to the machine learning model for training, and the first set of data-based predictions was generated from among the available designed synthetic compounds. Due to the drawbacks observed with a steroidal compound (see Chapter 4) only nonsteroidal compounds were considered.

We expected that experimental data would increase the accuracy of predictions and that this would be further improved as subsequent iterations incorporated even more data. To test this, each iteration of prediction by the model considered the experiment data for all previously tested compounds. Active compounds were defined as in Round 0. We tested male and female mice separately beginning with Round 1 predictions. For males, we completed three rounds of prediction and testing (summarized in Figure 5.5, left). In Round 1, eight of ten compounds were active based on *Nos2* reduction while none of the compounds reduced NO production. In Round 2, 10 of 13 compounds reduced both *Nos2* and NO production, and none were completely inactive. Finally, in Round 3, only one of the ten predictions was inactive. Between Round 1 and Round 3, *Nos2* expression decreased from 71% of vehicle on average to 57%. For NO production, the average for active compounds was 82% of vehicle in Round 2 and dropped to 68% in Round 3. Thus, the active compounds became more potent with each iteration of machine learning. We also measured *Cd274* (gene for PD-L1) and *Folr2* (gene for FR $\beta$ ) as additional markers of function though these data were not considered in defining activity for prediction (G. Cresswell, manuscript submitted).<sup>262</sup> Interestingly, changes in *Folr2* expression varied inversely with NO production, and a similar pattern was observed for *Cd274* until Round 3. For female mice, we completed two rounds of prediction and testing (summarized in Figure 5.5, right). The compounds tested in Round 1 were the same compounds tested in males. Six compounds were defined as active though none reduced both *Nos2* and NO production. In Round 2, the list of predictions diverged from the compounds predicted for males. Seven of ten compounds reduced both *Nos2* expression and NO production, and the remainder were inactive. *Nos2* expression was 86% of vehicle in Round 1 and 64% in Round 2 for active compounds. For NO production, the level was 63% of vehicle in both rounds, but there was only one active compound in Round 1. As with males, we observed increased potency among active compounds from one round to the next. For female-derived cells, most compounds in both rounds reduced *Folr2*, and there was a small improvement for *Cd274* modulation.

We next selected several compounds to validate against biological variation. Here, we applied more stringent selection criteria to define an active compound as one that reduces *Nos2* expression, *Cd274* expression, and NO production to at most 80% of that for vehicle-treated cells. This yielded eight compounds to test further for males. As show in Figure 5.6, the mean levels of *Nos2* and *Cd274* expression remained at or below 80% across independent experiments and were significantly different from vehicle for six of the nine compounds. There was greater variability between experiments for NO production though four compounds continued to reduce levels to approximately 80% of vehicle. As during the prediction phase, *Folr2* expression was not appreciably changed by these compounds. We did not use potency as a selection criterion and

instead tested compounds at 100 nM to bias our screen toward compounds that were effective at a low concentration. A preliminary dose-response experiment was performed with three compounds to determine whether this concentration is optimal (Figure 5.7). Interestingly, compound JMGC02S81 exhibits a trend of increasing potency as the concentration decreases while compound 70 shows the opposite trend. In parallel with experiments for males, we validated a set of seven compounds defined as active for females using the more stringent criteria (Figure 5.8). Overall, we observed more variability between experiments with females than with males. Most compounds continued to reduce *Nos2* expression to approximately 80% of vehicle but were not as potent as expected based on results in the prediction phase. Only two compounds, JMGC02S63 and JMGC02S99, continued to reduce both *Nos2* expression and NO production below the original 90% threshold.

We next tested the effect of compound treatment in a complete biological system. Among the compounds validated *ex vivo* for males we identified four as candidates for *in vivo* evaluation (green columns in Figure 5.6). These compounds—JMGC02S70, 81, 160, and 189—were selected based on the magnitude and significance of their effects on *Cd274* and *Nos2* expression and NO production. We tentatively selected compound JMGC02S99 as a candidate for *in vivo* study with females (green column in Figure 5.8) though it did not satisfy all three criteria for activity at the 80% threshold. JMGC02S81, a compound predicted for males, had the best activity in the validation phase. This was based on overall reduction of *Cd274* and *Nos2* expression and NO production. Thus, we selected it as the first compound to be evaluated *in vivo*.

To test JMGC02S81 *in vivo*, we utilized the same peritoneal tumor model from which we had been isolating myeloid cells as well as the POET-3 model of benign prostate inflammation. Overall, we did not observe any gross visual differences in the appearance of the liver or spleen between compound-treated and control mice. There were also no differences in the rate of change for body weight (Figure 5.9A), and mice remained active throughout treatment. We isolated peritoneal ascites from tumor-bearing mice following four days of treatment with the compound and enriched for Ly6C<sup>+</sup> Ly6G<sup>neg</sup> cells. These cells were then co-incubated with pre-activated OT-I cells to test their suppressive capacity. Based on results from the validation phase we expected reduced suppressive capacity in cells isolated from compound-treated mice. Indeed, there was a significant decrease in suppression of T cell proliferation at all myeloid:OT-I cell ratios (Figure 5.9B). This suggests that myeloid cells from tumor-bearing mice treated with JMGC02S81 are impaired in their suppressive function. Nitrite concentrations in the supernatants of the co-cultures were decreased by a substantial but non-significant degree (Figure 5.9C). We further found that adding the NOS inhibitor L-NMMA to the suppression assay permitted T cell proliferation at similar levels for co-cultures with cells from control and compound-treated mice. The effect of L-NMMA compared to untreated wells was larger for co-cultures with myeloid cells from vehicle-treated mice (Figure 5.9D). Together, these data indicate that NO is a key mechanism of suppression in this system in agreement with previous reports.<sup>117,206</sup> Interestingly, despite the impairment in function, the frequency of Ly6C<sup>+</sup> Ly6G<sup>neg</sup> cells was unchanged as were the frequencies of

populations expressing FR $\beta$ , iNOS, and PD-L1 (Figure 5.9E). This was unexpected for iNOS and PD-L1 since expression of the corresponding genes was reduced *ex vivo*. We also investigated the effect of modulating myeloid cells with JMGC02S81 on T cells *in vivo*. To accomplish this, we inflamed POET-3 mice with OT-I T cells and treated with JMGC02S81 for four days. We expected a higher frequency of T cells along with an increase in T cell activation as indicated by higher frequencies of T cells expressing LAG-3, PD-1, and/or TIM-3. These inhibitory receptors are expressed on T cells under conditions of chronic stimulation as occur during cancer and inflammation.<sup>263</sup> Changes in the frequencies of T cells expressing these markers may provide insights about the compound's effects on T cell activation status *in vivo*. As in the tumor-bearing model, we did not observe any changes in the frequency of the myeloid cells overall or in any specific subpopulations (Figure 5.10A). On the other hand, the frequency of LAG-3<sup>+</sup> and TIM-3<sup>+</sup> T cells was significantly lower in the compound-treated mice (Figure 5.10B). This is the opposite of the expected result but does suggest some change in the microenvironment that affects T cell activation.

Finally, we analyzed the predicted targets and performed a proteomics analysis of myeloid cells from treated mice in order to understand the mechanism underlying the immunomodulatory activity of JMGC02S81. First, we analyzed a subset of predicted targets from the interaction profile for JMGC02S81. To accomplish this, we used the Reactome Pathway Analysis tool.<sup>264,265</sup> We submitted the 100 highest-ranked entities from each of the sets of targets for which protein structures were either solved and deposited in the PDB or were modeled *in silico* by the Chopra lab. Of the 200 submissions, nine duplicates were removed, 33 were not mapped (Table 5.2), and the remaining 158 were mapped to biological pathways which were subsequently analyzed for enrichment (Table 5.3). The five most significantly enriched pathways are shown in Table 5.4 with the associated targets listed. The MMPs are particularly interesting since MMPs as a group are implicated in tumor metastasis and can also process various signaling molecules. MMP14 is necessary for monocyte extravasation, so inhibiting it could reduce myeloid cell infiltration of the tumor.<sup>266</sup> In a mouse model of cancer, MMP14 blockade resulted in decreased hypoxia and immunosuppression in the TME.<sup>267</sup> CARM1 is a coactivator of *Nos2*.<sup>268</sup> CARM1 inhibition by JMGC02S81 would be consistent with downregulation of *Nos2* in the *ex vivo* assays.

In order to determine whether treatment *in vivo* with JMGC02S81 altered protein expression we submitted matched samples from vehicle- and compound-treated tumor-bearing mice in three independent experiments to the Purdue Proteomics Facility for LC-MS/MS analysis. Decreased suppressive capacity of the compound-treated myeloid cells was confirmed via *ex vivo* suppression assay prior to submission. In total, 4,192 proteins were detected, and 72 were significantly ( $p < 0.05$ ) differentially expressed between vehicle- and compound-treated mice (Table 5.5). Among the significant results, six were exclusively detected in vehicle-treated cells, and two were only detected in JMGC02S81-treated cells (Table 5.6). We also cross-referenced the set of proteins detected in all three sample pairs by proteomic analysis with the set of predicted targets described above. Table 5.7 lists the 78 proteins found in both sets with the predicted rank for that set. Fold

changes in protein abundance were calculated as the ratio of label-free quantification intensity values for compound versus vehicle. SERPINB2 stands out among potential targets with an interaction rank of 20 or higher with a reduction in abundance of nearly 40 percent. SERPINB2 is induced in activated macrophages, and macrophages from *Serpin*<sup>-/-</sup> mice more strongly induced OVA-specific IFN $\gamma$  production by T cells. Thus, reduced SERPINB2 expression in suppressive myeloid cells may reduce their function and illuminate a potential mechanism for JMGC02S81.<sup>269</sup>

## 5.4 Discussion

Tumor-derived myeloid cells are a limited resource, making efforts toward drug discovery for these cells using high-throughput methods rather challenging. Large numbers of cells are required to perform hypothesis-generating screens for druggable targets as well as hypothesis-driven searches for new therapeutic compounds against specific targets. Unfortunately, there are no immortalized cell lines available that can fully reproduce the biology of tumor-derived suppressive myeloid cells. Here, we have successfully bypassed the requirement for large quantities of cells in order to screen potential immunomodulatory compounds against primary suppressive myeloid cells. We began with a set of over seven hundred compounds and, using the novel approach described above, identified 16 “hits” despite screening fewer than 10% of the total compounds against cells. This efficiency greatly exceeds the approximate 1 – 2% hit rate of traditional HTS<sup>248,249</sup>. So far, at least one of these compounds shows immunomodulatory activity *in vivo*. This method is distinct from the virtual screening increasingly used for HTS in that each compound is modeled against a set of potential targets rather than a single target. In this manner, we expect to identify compounds that modulate the NO production phenotype via a multifaceted mechanism that is more likely to be restricted to immunosuppressive myeloid cells than if iNOS is targeted directly. This is important because iNOS is also utilized by a variety of non-myeloid cell types under inflammatory conditions such as infection.<sup>270</sup>

Our approach has several important and unique advantages over traditional HTS. One of these is its flexibility. The interaction profile between compounds and targets can be constructed from any large dataset so long as interactions between compounds and targets can be modeled. Moreover, any measurable experimental output can be used to train the machine learning model. Thus, this method is applicable to biological systems beyond suppressive myeloid cells. Secondly, we can modify parameters throughout the process in order to refine predictions. This is possible because compound selection is done iteratively rather than by screening an entire library at once. This improves the efficiency of drug discovery by excluding suboptimal compounds prior to screening. For example, we could have added reduction in *Folr2* and/or *Cd274* expression to the definition of an active compound prior to making Round 3 predictions for males. In the same way, we can influence the potency of predicted compounds. A stepwise reduction in the threshold for activity with each iteration of machine learning would be expected to increase potency. Interestingly, we observed an increase in potency from one round to the next even though we held the definition of “active” to levels  $\leq$  90% of vehicle. Another advantage comes from the use of compound-target

interaction profiles. Upon identifying an active compound, we can consult the corresponding interaction profile to identify the proteins or networks most likely to be modulated by the compounds. This information may in turn lead to novel therapeutic targets underlying the phenotype of interest. This is particularly advantageous when a phenotype is known but not the underlying pathways or mechanisms that govern it.

A valuable feature of the *ex vivo* screening format used here is that it can be easily and rapidly evaluated using RT-qPCR and a colorimetric assay. However, using 96-well plates to accommodate small cell numbers does not readily allow protein quantification. A large proportion of the cells remain strongly adhered to the wells after treatment such that FACS analysis would not reflect the entire population, and not enough cells are used for Western blotting. Traditional Western blotting would also be time-consuming in this context. In-cell Western blotting with fluorescent antibodies is a technique that can be considered in the future. Thus, although changes in protein levels would be more meaningful in terms of biological activity, we measured gene expression changes with the assumption that eventually changes in mRNA abundance will influence protein levels. Despite using *Nos2* expression rather than iNOS levels to define activity the machine learning model accurately predicted compounds that reduce NO production. In fact, the Round 1 compounds defined as active were exclusively ones that reduce *Nos2* expression, yet several Round 2 predictions reduced both *Nos2* and NO production. Interestingly, reduced *Nos2* expression did not correspond to a lower frequency of iNOS<sup>+</sup> cells after *in vivo* treatment. This is not surprising given that discord between levels of mRNA and protein is widely reported.<sup>271</sup> Even differential gene expression does not necessarily correlate with similar changes in protein levels.<sup>272</sup> Oxidative stress, a prominent feature of the TME, can affect this by changing the time scales on which changes in transcript and protein levels occur.<sup>273</sup> On the other hand, since nitric oxide production by MDSC is directly involved in T cell suppression, we attempted to link the *ex vivo* and *in vivo* assays by quantifying NO production and T cell suppression. The effect of JMGC02S81 on these two parameters was consistent, suggesting that changes in NO production *ex vivo* can predict a compound's impact on suppressive activity.

We examined specific cell populations by flow cytometry after *in vivo* JMGC02S81 treatment in mouse models of cancer and benign inflammation. We did not expect a difference in the frequency of Ly6C<sup>+</sup> Ly6G<sup>neg</sup> cells as a primary outcome since the machine learning model was trained to predict based on modulation of the NO production pathway. That does not rule out the possibility that a predicted compound could interact with targets involved in myeloid cell expansion, trafficking, or cell survival, but we did not observe any changes associated with JMGC02S81 treatment. In the POET-3 inflammation model, the decreased frequency of LAG-3<sup>+</sup> and TIM-3<sup>+</sup> T cells in treated mice was initially surprising. These inhibitory markers are upregulated on activated T cells due to acute and chronic inflammation associated with viral infection as well as cancer.<sup>274–</sup>  
<sup>276</sup> In this model, the OT-I cells used to induce inflammation had been stimulated with ova peptide for two days *ex vivo* and an additional 6 days *in vivo*. The T cells could become exhausted in this scenario and begin expressing markers such as LAG-3 and TIM-3. Indeed, we expected decreased

myeloid cell-mediated suppression during JMGC02S81 treatment to result in higher T cell activation that would correspond to increased expression of LAG-3 and TIM-3. However, this hypothesis did not account for the possibility that the suppressive myeloid cells play a larger role in inducing the exhaustion phenotype than the antigen stimulation. Indeed, dendritic cells stimulated with M-CSF inhibit T cell activation and induce PD-1 expression by the T cells.<sup>277</sup> MDSC co-cultured with T cells have also been shown to induce expression of exhaustion markers after only 3 days through a mechanisms that was not fully elucidated.<sup>278</sup> TIM-3 expression is induced by a variety of factors, including PGE<sub>2</sub> which is known to be produced by MDSC and TAM.<sup>134,274,279</sup> One possibility is that JMGC02S81 reduces PGE<sub>2</sub> production by myeloid cells. This would have to be verified but may explain why blocking MDSC function with JMGC02S81 results in fewer LAG-3<sup>+</sup> and TIM-3<sup>+</sup> T cells.

The bioinformatic analysis of top-ranked targets in the interaction profile for JMGC02S81 revealed potentially relevant targets to myeloid cells and to the iNOS pathway. It is interesting to note that iNOS did not appear in the list of targets though it could simply be further down in ranking. The list of 200 targets analyzed here is less than 10% of the total number of potential targets; including additional targets could provide additional insights toward relevant pathways. Indeed, it is possible that more important targets are not as strongly predicted to interact with JMGC02S81 and would have been excluded from this initial analysis. The proteomics analysis of myeloid cells treated *in vivo* revealed an additional target, SERPINB2, that merits further evaluation as it has been suggested to serve an anti-inflammatory function in macrophages. Interestingly, there was no enrichment of pathways relevant to immune function among the significantly modulated proteins. This may indicate an indirect mechanism for JMGC02S81 against myeloid cell suppressive function, or it may be that statistical significance is not an appropriate filter for the data in this case.

One interesting observation from these studies is that cells derived from male and female mice responded differently to the same compounds in the *ex vivo* screening assays. This resulted in predictions that were sex-specific except for four common predictions. This is not altogether unexpected as it is known that men and women respond differently to various drugs due to physiological, hormonal, and metabolic differences between the sexes.<sup>280</sup> Sex differences in the immune response have also been noted. For instance, innate immune cells from females respond more robustly to stimulation of toll-like receptor (TLR) 7 than males while the opposite is true with regard to TLR4 stimulation.<sup>281</sup> It has been shown in a mouse melanoma model that females respond more favorably than males to PD-L1 blockade due to the influence of PD-L1 on estrogen responsiveness in Tregs.<sup>282</sup> Thus, it is possible that the different predictions for each sex correspond to overall different sets of targets that ultimately modulate NO production. This would need to be determined both experimentally and bioinformatically.





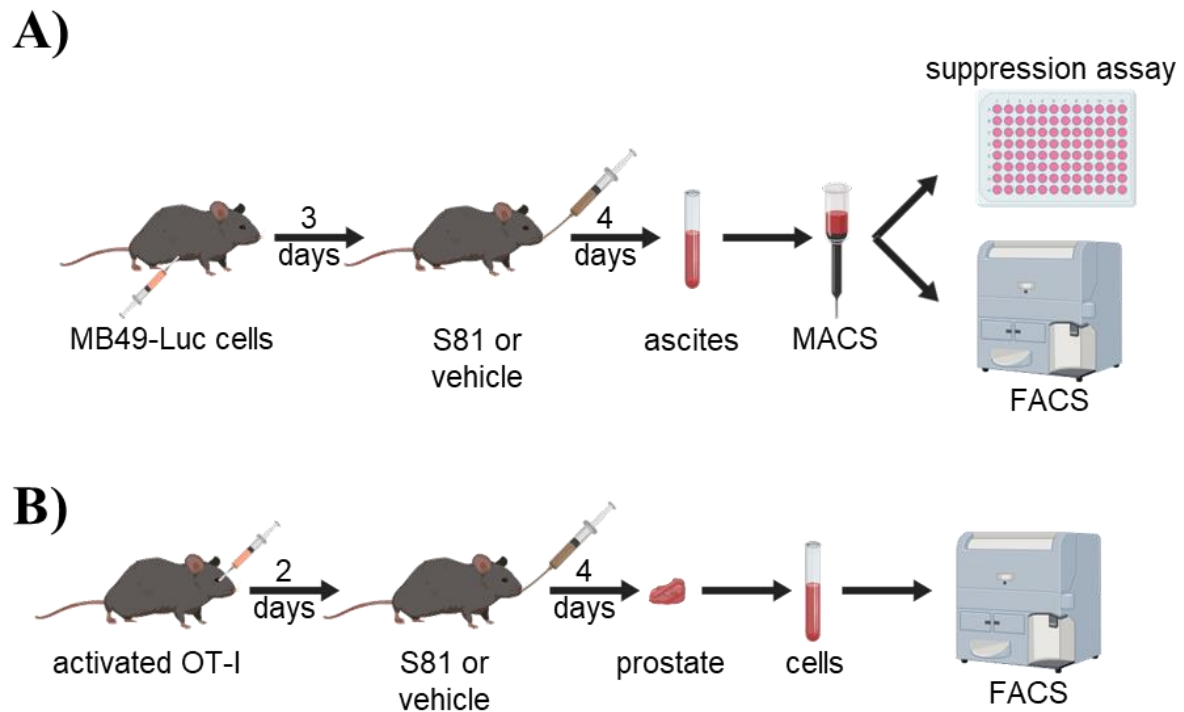


Figure 5.2 *In vivo* treatments with JMGC02S81

A) Schematic of tumor model treatment experiments. B) Schematic of POET-3 benign inflammation treatment experiments. Graphics created with BioRender.com.

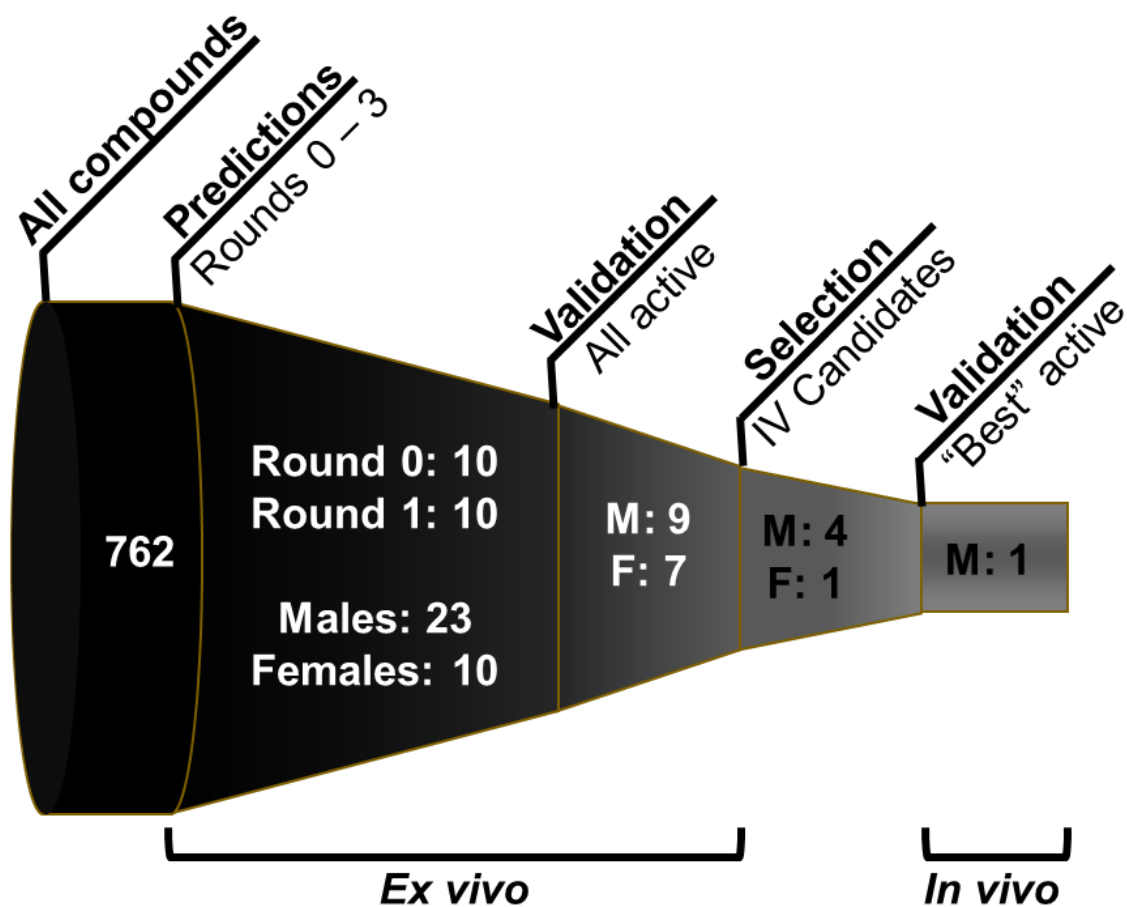


Figure 5.3 Diagram of experiments with compounds

A set of 762 compounds was narrowed through iterative machine learning to generate predictions which were screened *ex vivo* with tumor-derived Ly6C<sup>+</sup> Ly6G<sup>neg</sup> cells for activity against the NO production pathway. Active compounds from the set of predictions were experimentally validated *ex vivo*. A few were identified as candidates for *in vivo* testing, and the compound exhibiting the most potency in *ex vivo* assays was selected for *in vivo* studies.

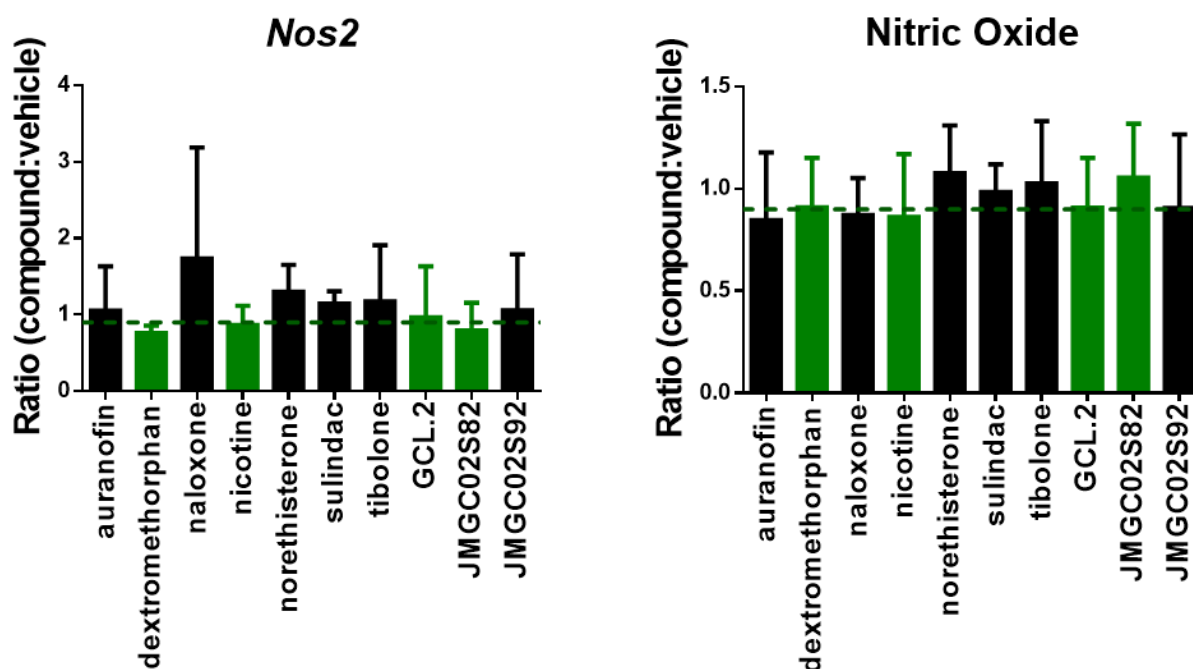


Figure 5.4 Round 0 predictions exhibit minimal activity against the NO production pathway

Ly6C<sup>+</sup> Ly6G<sup>neg</sup> cells isolated from MB49-Luc peritoneal tumor ascites of female mice were incubated with the indicated compounds at 100 nM for 24 hours (18 hours hypoxic/6 hours normoxic). RNA was isolated for gene expression analysis, and the nitrite content of cell-free supernatants was quantified using a Griess assay. Results are shown as a ratio with respect to vehicle-treated cells given by  $\frac{\text{level in compound-treated}}{\text{level in vehicle-treated}}$ . Dashed lines are set at 0.9 and indicate the threshold at or below which a compound is considered active for the given parameter. Green columns indicate compounds designated as active in Round 0 for the purposes of machine learning prediction. Data represent three (gene expression) or two (nitric oxide production) independent experiments with pooled cells from at least five mice per experiment. Error bars are standard deviation.

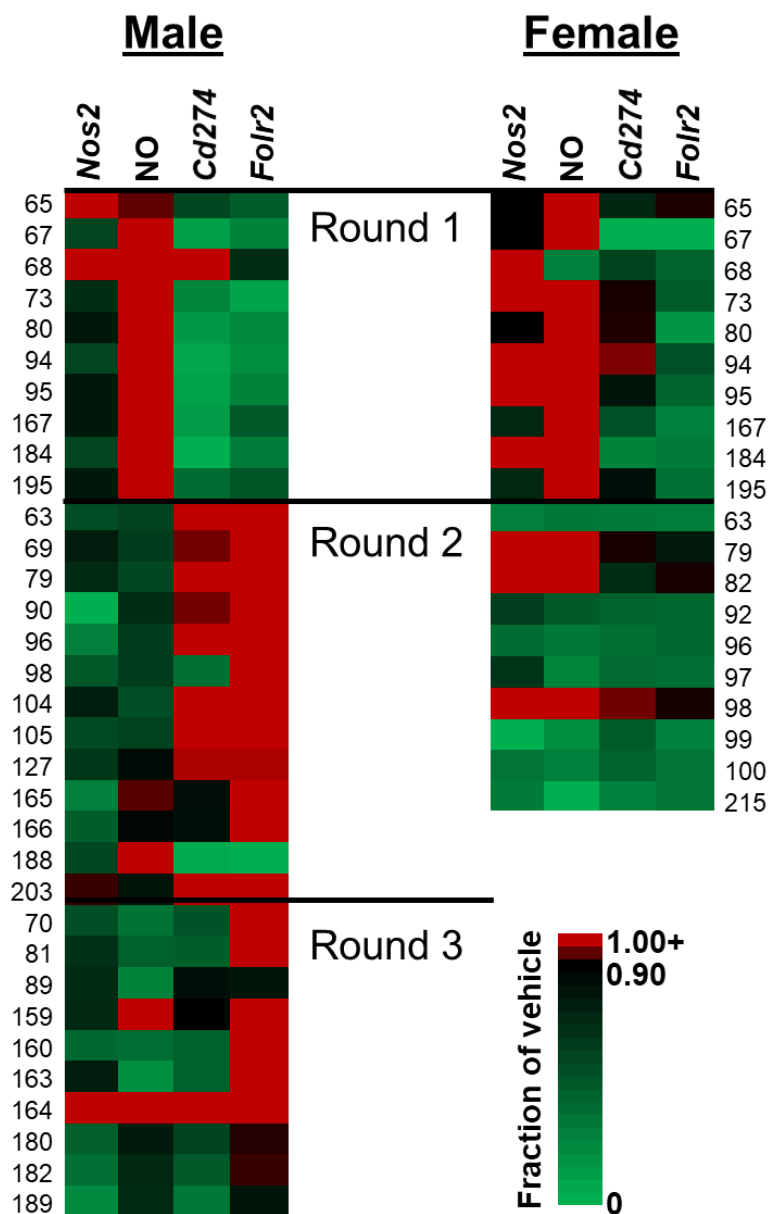


Figure 5.5 The accuracy of machine learning predictions for compounds that modulate the NO production pathway improves with iteration

Ly6C<sup>+</sup> Ly6G<sup>neg</sup> cells isolated from MB49-Luc peritoneal tumor ascites of male and female mice were incubated with the indicated compounds at 100 nM for 24 hours (18 hours hypoxic/6 hours normoxic). RNA was isolated for gene expression analysis (*Nos2*, *Cd274*, *Folr2*), and the nitrite content of cell-free supernatants was quantified using a Griess assay (NO). Results are color-coded based on the ratio with respect to vehicle-treated cells given by  $\frac{\text{level in compound-treated}}{\text{level in vehicle-treated}}$  and represented as a heatmap. The activity threshold of 0.9 is set to black. Shades of green (ratio  $\leq 0.9$ ) denote active compounds for the given parameter, and shades of red (ratio  $> 0.9$ ) denote inactive compounds. Each round of screening was conducted as a single experiment with pooled cells from at least five mice.

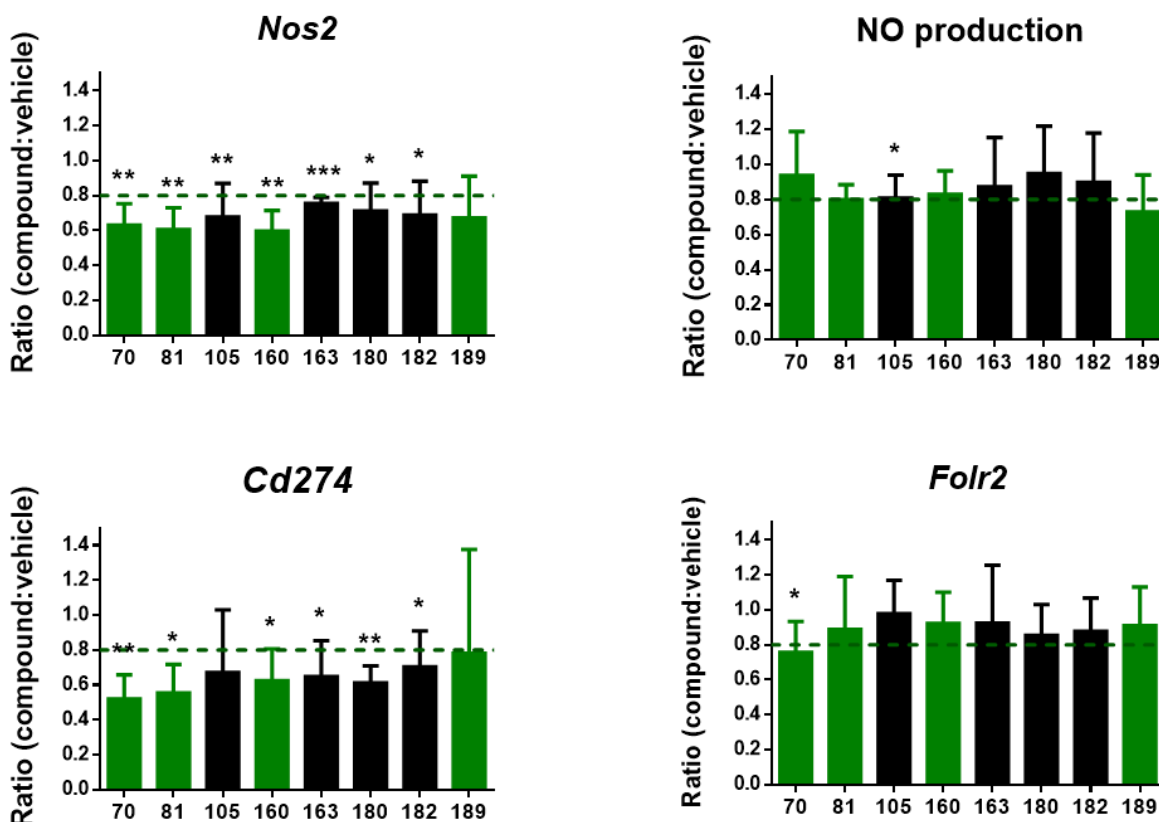


Figure 5.6 Activity defined by single observations during screening is reproducible during the validation phase

Ly6C<sup>+</sup> Ly6G<sup>neg</sup> cells isolated from MB49-Luc peritoneal tumor ascites of male mice were incubated with the indicated compounds at 100 nM for 24 hours (18 hours hypoxic/6 hours normoxic). A) RNA was isolated for gene expression analysis (*Nos2*, *Cd274*, *Folr2*), and the nitrite content of cell-free supernatants was quantified using a Griess assay (NO). Results are shown as a ratio with respect to vehicle-treated cells given by  $\frac{\text{level in compound-treated}}{\text{level in vehicle-treated}}$ . Dashed lines are set at 0.8 and indicate the threshold at or below which a compound is considered active for the given parameter. Green columns indicate compounds designated as active for the purposes of candidate selection for *in vivo* testing. Data represent four (gene expression) or three (nitric oxide production) independent experiments with pooled cells from at least five mice per experiment. Error bars are standard deviation. Statistical test is a one-tailed ratio-paired *t*-test and \**p*<0.05, \*\**p*<0.01, \*\*\**p*<0.005.

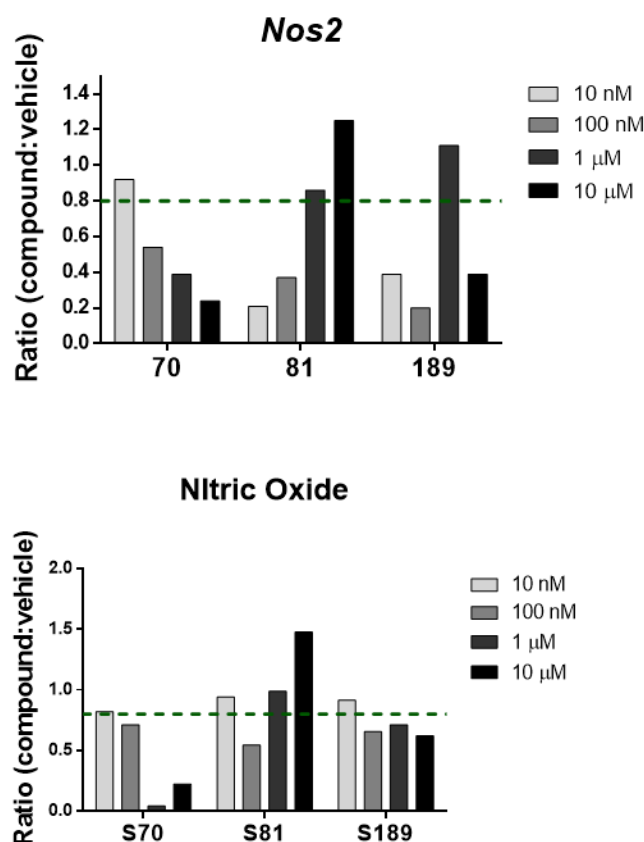


Figure 5.7 Preliminary dose-response shows compound concentration used for screening and validation phases is neither minimal nor maximal

Ly6C<sup>+</sup> Ly6G<sup>neg</sup> cells isolated from MB49-Luc peritoneal tumor ascites of male mice were incubated with the indicated compounds at 100 nM for 24 hours (18 hours hypoxic/6 hours normoxic). RNA was isolated for gene expression analysis of *Nos2* (top), and cell-free supernatants were saved for a nitrite quantification (bottom). Results are shown as a ratio with respect to vehicle-treated cells given by  $\frac{\text{level in compound-treated}}{\text{level in vehicle-treated}}$ . The dashed line set at 0.8 indicates the threshold at or below which a compound is considered active for the given parameter. Data represent a single experiment with pooled cells from five mice

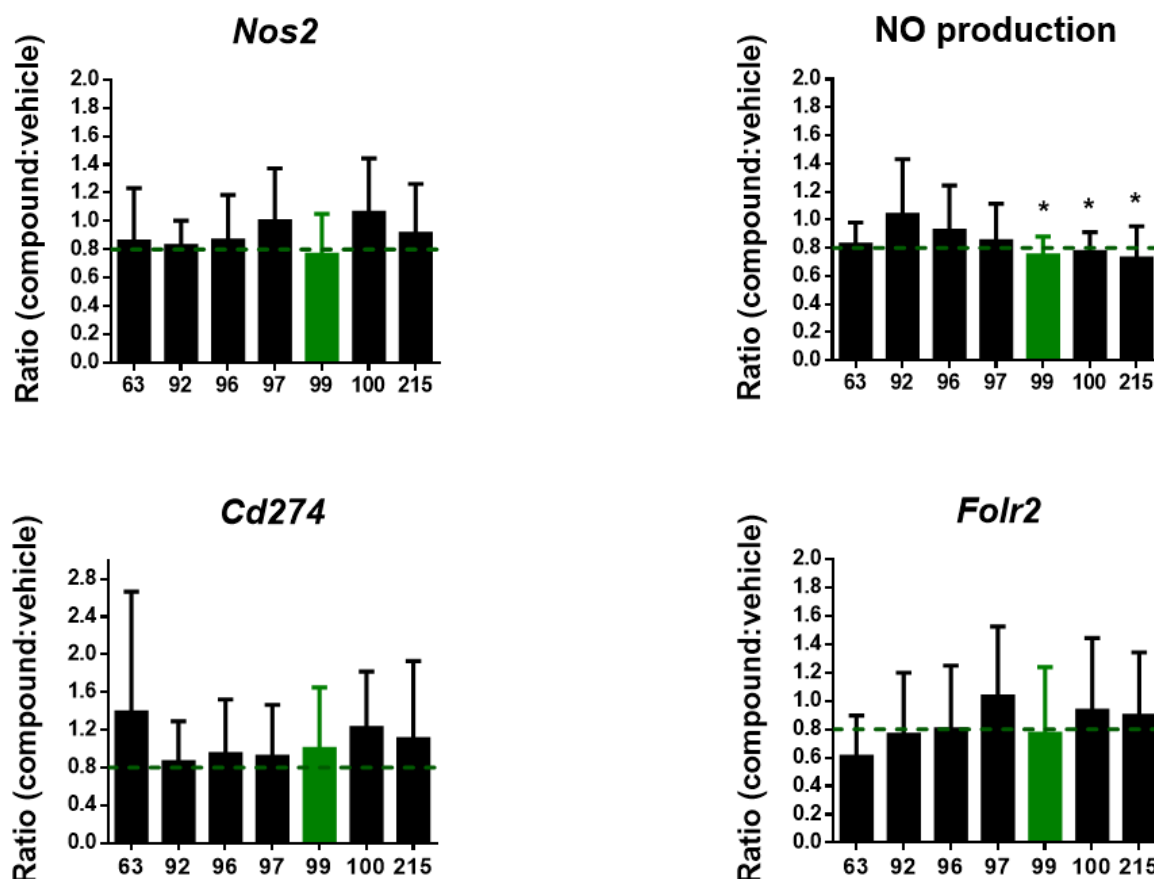


Figure 5.8 Activity defined by single observations during screening is less robust for female-derived cells

Ly6C<sup>+</sup> Ly6G<sup>neg</sup> cells isolated from MB49-Luc peritoneal tumor ascites of female mice were incubated with the indicated compounds at 100 nM for 24 hours (18 hours hypoxic/6 hours normoxic). A) RNA was isolated for gene expression analysis (*Nos2*, *Cd274*, *Folr2*), and the nitrite content of cell-free supernatants was quantified using a Griess assay (NO). Results are shown as a ratio with respect to vehicle-treated cells given by  $\frac{\text{level in compound-treated}}{\text{level in vehicle-treated}}$ . Dashed lines are set at 0.8 and indicate the threshold at or below which a compound is considered active for the given parameter. The green column indicates a compound designated as active for the purposes of candidate selection for *in vivo* testing. Data represent four independent experiments with pooled cells from at least five mice per experiment. Error bars are standard deviation.

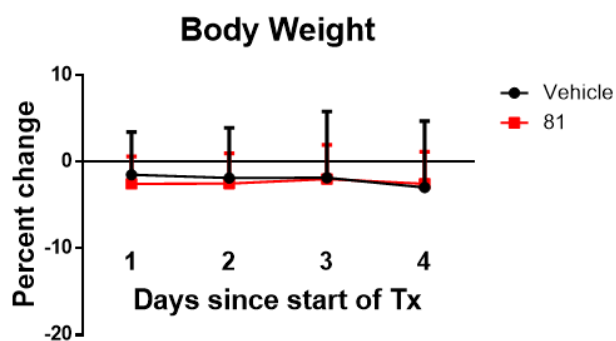
Statistical test is a one-tailed ratio-paired *t*-test and \**p*<0.05.

Figure 5.9 Short-term treatment with JMGC02S81 is non-toxic *in vivo* and reduces the suppressive capacity of tumor-derived Ly6C<sup>+</sup> Ly6G<sup>neg</sup> cells

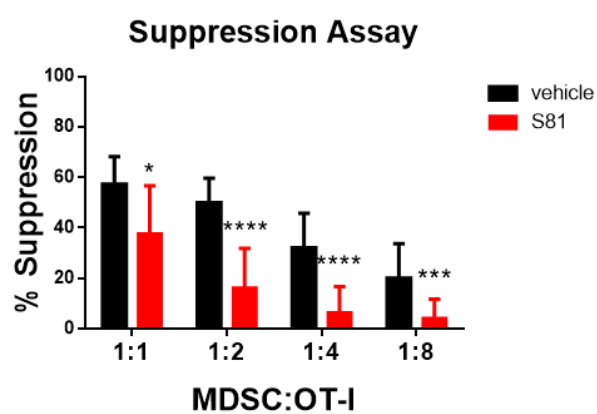
Male mice with MB49-Luc peritoneal tumors were treated for four days with 100 mg/kg/day JMGC02S81 by oral gavage. Ly6C<sup>+</sup> Ly6G<sup>neg</sup> cells were isolated from peritoneal ascites and co-cultured with pre-activated OT-I T cells for 18 hours under hypoxic atmosphere. A) Percent change in body weight. B) Suppression of OT-I cell proliferation quantified via EdU uptake and as calculated by  $\frac{(OT-I_{alone} - OT-I_{81})}{(OT-I_{alone})} \times 100$ . C) OT-I cell proliferation quantified by EdU uptake at 1:1 ratio with myeloid cells with and without the iNOS inhibitor L-NMMA. D) Nitrite concentration in the supernatants from a suppression assay. E) FACS analysis of Ly6C<sup>+</sup> Ly6G<sup>neg</sup> cells. Data in (A) and (E) represent three independent experiments with a total of 11 (vehicle) and 13 (JMGC02S81) mice kept as biological replicates. Data in (B) represent two experiments with eight (vehicle) and nine (JMGC02S81) mice kept as biological replicates. Data in (C) and (D) represent single experiments with 3 – 5 mice kept as biological replicates. Error bars are standard deviation. Statistical test is an unpaired one-tailed Student's *t*-test and \**p*<0.05, \*\**p*<0.01, \*\*\**p*<0.005, \*\*\*\**p*<0.001. The *t*-test for comparisons within treatments in (C) are paired



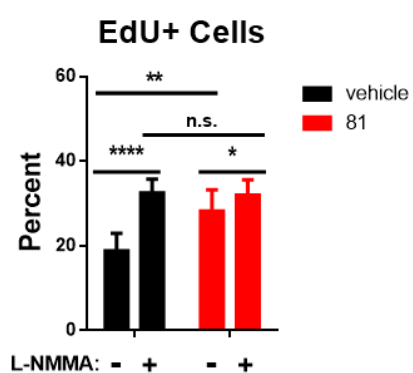
A)



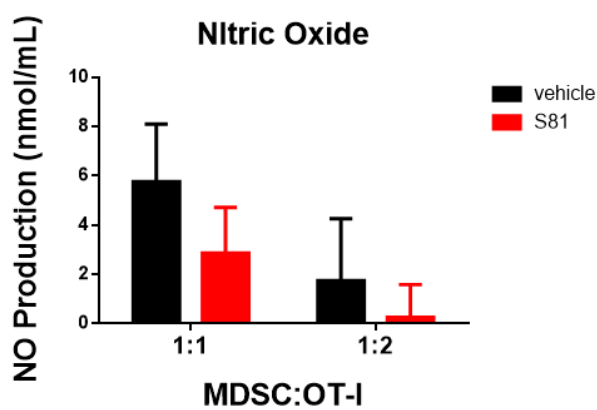
B)



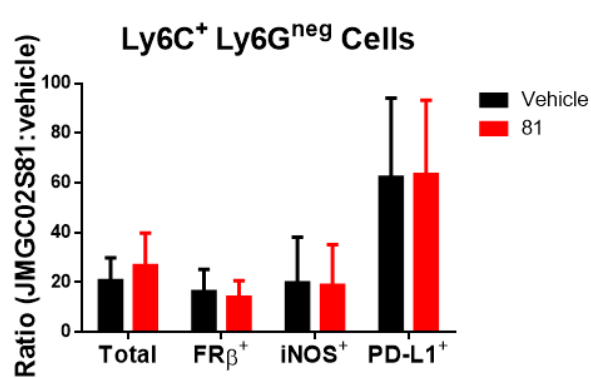
C)



D)



E)



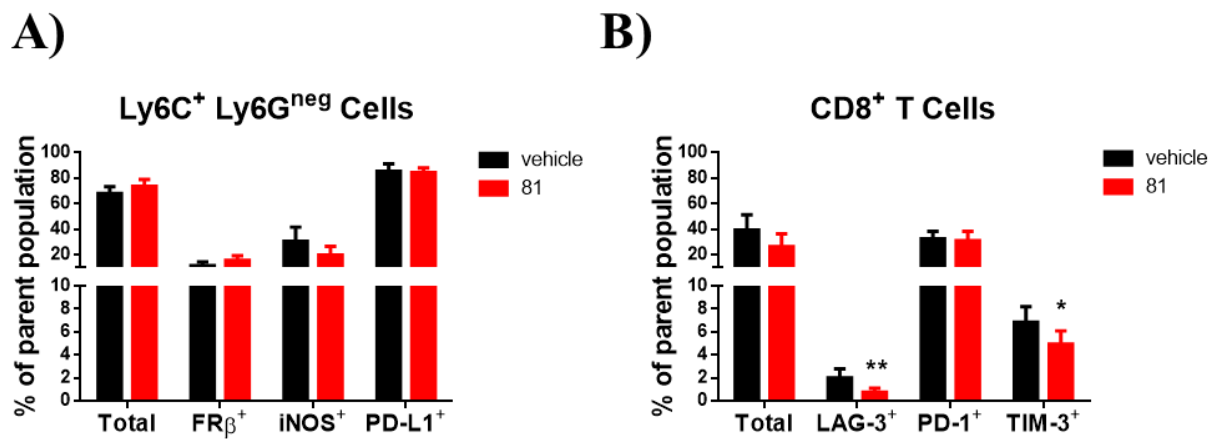


Figure 5.10 Short-term treatment with JMGC02S81 in a model of benign inflammation alters the expression of activation markers on tissue-infiltrating CD8<sup>+</sup> T cells

Prostate inflammation was induced in male POET-3 mice via retro-orbital injection of pre-activated OT-I cells. Mice were treated for four days with 100 mg/kg/day JMGC02S81 by oral gavage. Prostate tissue was harvested and infiltrating Ly6C<sup>+</sup> Ly6G<sup>neg</sup> cells (A) and CD8<sup>+</sup> T cells (B) were analyzed by FACS. Data represent two independent experiments with a total of five mice per group kept as biological replicates. Error bars are standard deviation. Statistical test is a two-tailed ratio-paired *t*-test and \**p*<0.05, \*\**p*<0.01.

Table 5.1 Compounds tested in Rounds 0 – 3

Round	Compound	Sex	Round	Compound	Sex
0	auranofin	F	2	JMGC02S63	F
0	dextromethorphan	F	2	JMGC02S79	F
0	naloxone	F	2	JMGC02S82	F
0	nicotine	F	2	JMGC02S92	F
0	norethisterone	F	2	JMGC02S96	F
0	sulindac	F	2	JMGC02S97	F
0	tibolone	F	2	JMGC02S98	F
0	GCL.2	F	2	JMGC02S99	F
0	JMGC02S82	F	2	JMGC02S100	F
0	JMGC02S92	F	2	JMGC02S215	F
1	JMGC02S65	F, M	3	JMGC02S70	M
1	JMGC02S67	F, M	3	JMGC02S81	M
1	JMGC02S68	F, M	3	JMGC02S89	M
1	JMGC02S73	F, M	3	JMGC02S159	M
1	JMGC02S80	F, M	3	JMGC02S160	M
1	JMGC02S94	F, M	3	JMGC02S163	M
1	JMGC02S95	F, M	3	JMGC02S164	M
1	JMGC02S167	F, M	3	JMGC02S180	M
1	JMGC02S184	F, M	3	JMGC02S182	M
1	JMGC02S195	F, M	3	JMGC02S189	M
2	JMGC02S63	M			
2	JMGC02S69	M			
2	JMGC02S79	M			
2	JMGC02S90	M			
2	JMGC02S96	M			
2	JMGC02S98	M			
2	JMGC02S104	M			
2	JMGC02S105	M			
2	JMGC02S127	M			
2	JMGC02S165	M			
2	JMGC02S166	M			
2	JMGC02S188	M			
2	JMGC02S203	M			
F: female, M: male					

Table 5.2 JMGC02S interaction targets excluded from Reactome enrichment analysis

BNIP3	HSPB7
BOK	KLHL7
BROX	KLK10
CCL24	MAST2
CORO1C	NAA20
CORO2A	NAA50
CRELD1	NT5DC3
CRYGA	NUMBL
CRYZL1	PCSK7
CYP20A1	PDCD6
DCLK1	QPCTL
DDX56	RBMS1
DHX35	RPL7L1
DNAJC17	SEMA3C
ECHDC2	SEPHS1
EML1	SLIRP
HSPB7	SNX12

Table 5.3 JMGC02S interaction targets included in Reactome enrichment analysis

ACADM	DCTD	IARS2	PCMT1	STXBP2
ACADVL	DDB1	IKBKE	PDE8A	SUCLG2
ACO1	DGCR8	IMPDH1	PDGFA	SUMF2
ACOT6	DHX15	IQGAP1	PEBP1	TBL3
ACY1	DIS3	ITGA3	PFKFB3	TFPI
ADAMTS1	DLD	KAT2A	PHF2	TGS1
ADSSL1	DNAJC24	KLHL2	PIGA	TJP2
AIFM2	DNM1L	KMT5A	PIP4K2C	TMX3
AKR1A1	EFNA1	LRP1	PITRM1	TRMT61A
ALKBH2	EFNB2	LYPLA2	POLG	TUBA1C
AMACR	EHD1	MAD2L2	PON3	TUBB4A
ANXA5	EIF2B2	MAN2A1	PRMT1	UBA1
ARFGAP1	EMG1	MAP1LC3B	PRODH	UBA3
ARHGAP21	ENAH	MAP2K1	PROZ	UCHL1
ARHGEF7	F7	MAPRE1	PRPF31	UGDH
ARPC1A	FERMT3	MERTK	PSMD4	WDR20
ATG4B	FGFR1	MMP14	PSMD9	YARS2
ATP9B	FLNA	MMP3	RAB21	YP46A1
B4GALT1	FLNC	MOCS2	RAB31	
B4GALT7	FPGS	MRM1	RCC1	
BACE1	FRS2	MRPL39	RINT1	
BST1	GALE	MSL3	SAE1	
BUB3	GMDS	MUC1	SDCBP	
CARM1	GMPR2	MVD	SEC24B	
CASC3	GNAI3	MVK	SEH1L	
CASK	GPI	MYO1C	SEMA4A	
CASP6	GRHPR	NDUFA9	SERPINB2	
CASP9	GSR	NDUFAB1	SLC27A1	
CDK8	GSTZ1	NMT2	SMAD1	
CLNS1A	GUSB	NPEPPS	SMAP2	
CPNE1	HSD17B7	NRP2	SMYD2	
CSNK1D	HSPA9	NSMCE2	SNUPN	
CTSD	HSPB1	NT5C	SPTLC1	
CUL5	HSPD1	NUDT16	SSB	
CXCL3	HTRA1	OLA1	STAT3	

Table 5.4 Top 5 significantly enriched pathways

Pathway Name (p-value)	Gene	Protein
Activation of Matrix Metalloproteinases (2.92e-4)	MMP3 MMP14	Stromelysin-1 Matrix metalloproteinase-14
Regulation of cholesterol biosynthesis by SREBP (SREBF) (5.62e-4)	CARM1 SEC24B MVD TGS1 MVK	Histone-arginine methyltransferase CARM1 Protein transport protein Sec24B Diphosphomevalonate decarboxylase Trimethylguanosine synthase Mevalonate kinase
Collagen degradation (9.93e-4)	CTSD MMP3 MMP14	Cathepsin D Stromelysin-1 Matrix metalloproteinase-14
Activation of gene expression by SREBF (SREBP) (0.001)	CARM1 MVK MVD TGS1	Histone-arginine methyltransferase CARM1 Mevalonate kinase Diphosphomevalonate decarboxylase Trimethylguanosine synthase
L1CAM interactions (0.001)	FGFR1 NRP2 TUBB4A LYPLA2 SDCBP MAP2K1 TUBA1C	Fibroblast growth factor receptor 1 Neuropilin-2 Tubulin beta-4A chain Acyl-protein thioesterase 2 Syntenin-2 Dual specificity mitogen-activated protein kinase kinase 1 Tubulin alpha-1C chain

Table 5.5: Significantly differentially expressed proteins

Symbol	Name	Symbol	Name
Actc1	Actin	Nup88	Nuclear pore complex protein Nup88
Ankrd44	Serine/threonine-protein phosphatase 6 regulatory ankyrin repeat subunit B	Otud4	OTU domain-containing protein 4
Arl1	ADP-ribosylation factor-like protein 1	Pck2	Phosphoenolpyruvate carboxykinase
Bcl2l13	Bcl-2-like protein 13	Pdcd2	Programmed cell death protein 2
Btaf1		Pdlim1	PDZ and LIM domain protein 1
Ccdc51	Coiled-coil domain-containing protein 51	Ppm1g	Protein phosphatase 1G
Cers5	Ceramide synthase 5	Prpf40a	Pre-mRNA-processing factor 40 homolog A
Cetn3	Centrin-3	Rab18	Ras-related protein Rab-18
Cox7a2	Cytochrome c oxidase subunit 7A2	Ranbp10	Ran-binding protein 10
Cryz11	Quinone oxidoreductase-like protein 1	Rer1	Protein RER1
Cyb5a	Cytochrome b5	Rfc2	Replication factor C subunit 2
Cyp20a1	Cytochrome P450 20A1	Rprd1b	Regulation of nuclear pre-mRNA domain-containing protein 1B
Dlg1	Disks large homolog 1	Rps27a	Ubiquitin-40S ribosomal protein S27a
Dmx11	DmX-like protein 1	Rrs1	Ribosome biogenesis regulatory protein homolog
Eed	Polycomb protein EED	Sgpp1	Sphingosine-1-phosphate phosphatase 1
Eif1a	Eukaryotic translation initiation factor 1A	Slc25a20	Mitochondrial carnitine/acylcarnitine carrier protein
Eif3k	Eukaryotic translation initiation factor 3 subunit K	Smarca4	Transcription activator BRG1
Exosc9	Exosome complex component RRP45	Strn	Striatin
Fgg	Fibrinogen gamma chain	Sumf1	Sulfatase-modifying factor 1
Fryl		Sumo2	Small ubiquitin-related modifier 2
Gyk	Glycerol kinase	Tecr	Very-long-chain enoyl-CoA reductase

Table 5.5 continued

Iba57	Putative transferase CAF17 homolog	Timm17b	Mitochondrial import inner membrane translocase subunit Tim17-B
Isg20	Interferon-stimulated gene 20 kDa protein	Timm23	Mitochondrial import inner membrane translocase subunit Tim23
Iws1	Protein IWS1 homolog	Tmx2	Thioredoxin-related transmembrane protein 2
Luc7l2	Putative RNA-binding protein Luc7-like 2	Tomm22	Mitochondrial import receptor subunit TOM22 homolog
Ly6a	Lymphocyte antigen 6A-2/6E-1	Trpv2	Transient receptor potential cation channel subfamily V member 2
Mrpl49	39S ribosomal protein L49	Tubgcp3	Gamma-tubulin complex component 3
Mrps2	28S ribosomal protein S2	Tufm	Elongation factor Tu, mitochondrial
Nagk	N-acetyl-D-glucosamine kinase	Ufsp2	Ufm1-specific protease 2
Nbeal2	Neurobeachin-like protein 2	Usp25	Ubiquitin carboxyl-terminal hydrolase 25
Ndufs6	NADH dehydrogenase [ubiquinone] iron-sulfur protein 6	Vamp7	Vesicle-associated membrane protein 7
Nelfb	Negative elongation factor B	Vdac3	Voltage-dependent anion-selective channel protein 3
Nfu1	NFU1 iron-sulfur cluster scaffold homolog	Vps25	Vacuolar protein-sorting-associated protein 25
Nol11	Nucleolar protein 11	Xaf1	XIAP-associated factor 1
Nop16	Nucleolar protein 16	Zfpl1	Zinc finger protein-like 1
Nup155	Nuclear pore complex protein Nup155	Znfx1	NFX1-type zinc finger-containing protein 1



Table 5.6 Proteins appearing only in vehicle- or compound-treated samples

Symbol	Protein Name	Treatment
Dmx1l	DmX-like protein 1	Vehicle
Eif1a	Eukaryotic translation initiation factor 1A	Vehicle
Gyk	Glycerol kinase	Vehicle
Ranbp10	Ran-binding protein 10	Vehicle
Tubgcp3	Gamma-tubulin complex component 3	Vehicle
Vps25	Vacuolar protein-sorting-associated protein 25	Vehicle
Cetn3	Centrin-3	JMGC02S81
Sumf1	Sulfatase-modifying factor 1	JMGC02S81

Table 5.7 Proteins contained in sets of predicted and detected targets

Symbol	FC	Rank	Set	Symbol	FC	Rank	Set
PSMD4	1.03	1	M	ARFGAP1	0.94	46	M
SERPINB2	0.63	1	S	PON3	0.97	48	M
CUL5	1.04	2	S	SAE1	1.05	48	S
GUSB	1.04	2	M	LYPLA2	1.28	49	M
HSPA9	1.14	3	S	DLD	1.05	50	S
DNM1L	0.99	4	M	EMG1	0.89	50	M
MAP2K1	0.99	4	S	PSMD9	1.13	51	M
MMP14	1.06	5	S	UGDH	1.08	52	S
HSPD1	1.10	6	M	MAN2A1	1.01	54	M
SEH1L	1.08	8	M	MYO1C	1.05	56	M
TBL3	1.15	12	M	NPEPPS	0.98	57	M
ACO1	0.96	13	S	ARHGEF7	0.95	59	M
LRP1	0.95	14	M	TJP2	1.00	60	M
RAB21	1.09	14	S	UBA3	0.95	60	S
CTSD	0.94	16	S	GMDS	1.15	61	S
DDB1	1.01	18	M	DHX15	1.03	62	M
GNAI3	1.07	18	S	MAPRE1	0.98	62	S
CPNE1	1.01	19	M	NDUFAB1	1.27	64	S
PRMT1	0.95	20	M	ACADVL	1.07	66	M
SDCBP	1.18	20	S	BUB3	1.01	69	M
ACADM	1.06	22	S	CRYZL1	0.61	70	M
UBA1	0.96	24	M	ITGA3	1.13	75	M
FLNA	0.97	25	S	MRPL39	1.01	76	M
SPTLC1	1.20	25	M	TMX3	0.94	78	M
RCC1	1.14	27	S	ANXA5	0.94	80	M
B4GALT1	1.03	28	S	PEBP1	1.36	80	S
DIS3	1.03	30	M	PDCD6	0.95	81	S
FERMT3	1.01	30	S	SSB	1.08	81	M
CYP20A1	1.19	32	M	IQGAP1	0.99	82	S
OLA1	0.97	35	S	NDUFA9	1.05	86	M
PITRM1	1.12	36	M	RBMS1	1.13	86	S
GSR	1.03	37	S	PRPF31	0.96	89	S
SUCLG2	1.07	37	M	EML1	1.06	93	M
EHD1	1.04	38	M	CORO1C	1.05	94	M
SEC24B	0.97	38	S	AKR1A1	1.62	95	S



## CHAPTER 6. SUMMARY AND FUTURE DIRECTIONS

The detrimental impact of suppressive myeloid cells on anti-cancer immunity as well as cancer immunotherapy is well-established. Growing interest in suppressive myeloid cells as a therapeutic target has resulted in greatly expanded knowledge of the biology underlying the origin, development, and function of these cells. Efforts to control suppressive myeloid cells can be summarized by three broad strategies: 1) direct elimination, 2) reduction of accumulation and/or function, and 3) conversion to an anti-tumor phenotype. Currently, effective and specific therapies remain elusive. Strategies such as anti-CCL2 or anti-iNOS therapy are effective in controlling the suppressive cells, but a lack of specificity leads to undesired or toxic side effects. We initiated the studies herein to address the problem with specificity in targeting suppressive myeloid cells for cancer immunotherapy.

First, we attempted to eliminate suppressive myeloid cells. We used folate-targeted PDT to limit the cytotoxic impact of a small molecule to MDSC and TAM by exploiting FR $\beta$  expression and by confining activation of the molecule to the tumor site. PDT depleted the suppressive cells from solid tumors in mice, and a single depletion event is sufficient to slow tumor growth significantly. However, the myeloid cell populations rebounded rapidly, and the anti-tumor effect was short-lived. Thus, direct elimination of suppressive myeloid cells from the tumor is insufficient as a cancer monotherapy and should be combined with tumor-targeting and/or immune-stimulating therapies. Additionally, a universal single-target strategy is not feasible since at least one mouse tumor model does not efficiently recruit FR $\beta^+$  myeloid cells. Inconsistent expression of therapeutic targets such as FR and PD-L1 has also been observed in the clinic.<sup>80,203,231</sup>

Elimination of suppressive cells directly from the tumor is not sustainable long-term, so we next sought to limit MDSC accumulation at the tumor site. To accomplish this, we used GCL.2, a synthetic compound predicted to interact with molecules implicated in MDSC expansion.<sup>283,284</sup> In GCL.2-treated mice, the frequencies of splenic and tumor-associated MDSC were reduced, indicating some impact on expansion and/or trafficking. Additional experiments are necessary to distinguish between these possibilities. A smaller proportion of MDSC expressed the function-associated markers FR $\beta$ , iNOS, and PD-L1, and the frequency of IFN $\gamma^+$  T cells increased in GCL.2-treated mice, suggesting increased T cell function. There was also a significant anti-tumor effect as determined by weighing the primary tumors and measuring changes in tumor burden via bioluminescence imaging. Together, these effects on MDSC, T cells, and tumor growth provide suggestive evidence that GCL.2 impairs MDSC function. Thus, GCL.2 shows promise as an immunomodulator, but its steroidal nature causes treatment-limiting side effects.

There are several avenues of follow-up arising from our work with GCL.2. First, further pursuit of GCL.2 as a therapeutic would require optimization of the dose and treatment schedule to improve tolerability. Future studies would also need to utilize a tumor model that allows more

reliable monitoring of tumor growth and has a longer window for therapeutic intervention. Second, the mechanism underlying GCL.2 activity has not been experimentally determined. Doing so raises the possibility of developing a non-steroidal molecule with the same target(s). GCL.2 was selected based on its interactions with a defined set of targets from a gene array, so candidates could be selected from the targets with the strongest interactions. A proteomics analysis comparing GCL.2-treated MDSC to controls could shed further light on the mechanism based on which pathways are modulated *in vivo*. Third, we observed that MDSC in the tumor ascites but not the solid tumor were affected. Is this due to inefficient drug penetration into the tumor, or do differences in the microenvironments of the two sites result in differential sensitivity to the drug? This could be addressed by sampling the two tissues via mass spectrometry to detect GCL.2, and perhaps GCL.2 could be isolated from cells and quantified. Fourth, are the anti-tumor effects and enhanced T cell IFN $\gamma$  production due to decreased MDSC frequency, or are the MDSC also less potently suppressive as well? A simple way to address this initially is to isolate GCL.2-treated MDSC and test their function in an *ex vivo* suppression assay. Finally, is the anti-tumor effect immunological in nature, or are there direct anti-tumor effects of GCL.2 that weren't observable *in vitro*. Depleting T cells *in vivo* during treatment could help to answer this question.

As we showed in Chapter 3, targeting a single molecule is likely to preclude benefits for patients in whom the target molecule is not expressed. Instead, we developed a selection method for therapeutic compounds based not on a single target but on predicted interactions with a large set of targets. Our goal was to modulate NO production, a key component of the myeloid suppressive phenotype, in a way that is not unique to any single tumor type or TME composition in order to develop more broadly applicable immunotherapies. We coupled the interaction profiling with a machine learning model that could incorporate experimental data about the performance of compounds and identify patterns among the interaction profiles for active and inactive compounds. Machine learning using increasing inputs of experimental data made compound prediction more accurate and enhanced the overall efficiency of the screening process. In contrast to the approximate 1-2% hit rate for HTS the hit rate for our method was over 20% at the end of *ex vivo* validation. We subsequently validated our method by demonstrating that at least one of the predicted compounds, JMGC02S81, successfully negatively impacted the NO production phenotype *ex vivo* and controlled myeloid cell suppressive function after *in vivo* treatment. Importantly, scarcity of primary myeloid cells is a major hurdle complicating drug screening and discovery efforts, and our approach reduces the total number of cells needed for screening. Another valuable aspect of this approach is its applicability to a variety of biological systems and diseases. It requires only a protein dataset associated with the phenotype of interest, a set of compounds for testing, and a phenotypic assay to measure compound performance.

In the future, we wish to elaborate some observations from these studies. First, the apparent sex-specific predictions are intriguing and constitute a very important finding if the specificity is real. To investigate this, we can perform reciprocal experiments to test compounds against cells derived from the opposite sex for which they were predicted. If the efficacy of the compounds is sex-

dependent then their activity should be diminished or absent in these experiments. Comparing the interaction profiles of the most potent compounds for males and females is likely to reveal distinct sets of targets as a result of differential regulation based on biological sex. It is not unreasonable to suggest that the TME differs between males and females, and tailoring therapies to address the differences could improve outcomes for patients. Next, in testing JMGC02S81 *in vivo* we did not examine tumor growth primarily because the peritoneal ascites tumor model used for *in vivo* validation is not ideal for studying tumor growth. Instead, we would use a slow-growing solid flank tumor for therapy studies. This provides a better window for intervention and allows direct measurement of tumor growth. To maintain immunogenicity, we could use the TRAMP-C2 cell line in males and, once we have a candidate for *in vivo* testing, a slow-growing MB49 clone in females. Since specific T cell antigens for both cell lines are known we could directly investigate tumor-specific immunity.<sup>223,285</sup> In the course of therapy studies, the dose of JMGC02S81 should be optimized for maximal anti-tumor effect, assuming this occurs. Finally, we observed differences in expression of T cell exhaustion markers after JMGC02S81 treatment in the prostate inflammation model. We did not fully characterize the T cell phenotype at the time and should examine IL-2 and IFN $\gamma$  production as both are progressively lost during exhaustion.<sup>263</sup> Prostate inflammation in the POET-3 model persists for several weeks after adoptive transfer of OT-I cells, and this affords the opportunity to examine T cell exhaustion and the effect of JMGC02S81 over a period consistent with chronic inflammation as well.<sup>258</sup> In the context of tumor immunotherapy, we could also examine T cell exhaustion using tumor models.

Currently, we are pursuing bioinformatic analyses in order to better understand the mechanism underlying the immunomodulatory activity of JMGC02S81. Throughout these studies herein, we were blinded as to how JMGC02S81 negatively impacts NO production and myeloid cell suppression. Experimentally, we showed that the myeloid cell suppressive function was impaired and that it correlated with diminished NO production. However, FACS analysis of Ly6C<sup>+</sup> Ly6G<sup>neg</sup> cells after *in vivo* treatment revealed that the frequency of iNOS-expressing cells was unchanged. Thus, we can speculate that the mechanism of JMGC02S81 involves modulating iNOS activity rather than reducing the protein level. By examining the interaction profile of JMGC02S81 we can hypothesize about the mechanism and begin to test it experimentally. We will also begin to evaluate potential targets revealed by a proteomic analysis of Ly6C<sup>+</sup> Ly6G<sup>neg</sup> cells isolated from tumor-bearing mice treated with JMGC02S81. We anticipate that differences in protein expression between these cells and those from vehicle-treated mice will help elucidate the mechanism underlying JMGC02S81 immunomodulatory activity. Cross-referencing the interaction profile targets with the proteomics results may help to identify additional candidate proteins involved in the mechanism of JMGC02S81. Ultimately, this work and characterization of other active compounds may lead to the discovery of novel networks governing suppressive function in myeloid cells.

## REFERENCES

1. Couzin-Frankel, J. Cancer Immunotherapy. *Science* (80-. ). **342**, 1432–1433 (2013).
2. Folkman, J. Isolation of a Tumor Factor Responsible for Angiogenesis. *J. Exp. Med.* **133**, 275–288 (1971).
3. Gimbrone, M. A., Leapman, S. B., Cotran, R. S. & Folkman, J. Tumor dormancy in vivo by prevention of neovascularization. *J. Exp. Med.* **136**, 261–76 (1972).
4. Ferrara, N. VEGF and the quest for tumour angiogenesis factors. *Nat. Rev. Cancer* **2**, 795–803 (2002).
5. Folkman, J., Watson, K., Ingber, D. & Hanahan, D. Induction of angiogenesis during the transition from hyperplasia to neoplasia. *Nature* **339**, 58–61 (1989).
6. Kim, K. J. *et al.* Inhibition of vascular endothelial growth factor-induced angiogenesis suppresses tumour growth in vivo. *Nature* **362**, 841–844 (1993).
7. Griffioen, A. W., Damen, C. A., Martinotti, S., Blijham, G. H. & Groenewegen, G. Endothelial intercellular adhesion molecule-1 expression is suppressed in human malignancies: the role of angiogenic factors. *Cancer Res.* **56**, 1111–17 (1996).
8. Hendry, S. A. *et al.* The Role of the Tumor Vasculature in the Host Immune Response: Implications for Therapeutic Strategies Targeting the Tumor Microenvironment. *Front. Immunol.* **7**, 621 (2016).
9. Maishi, N. & Hida, K. Tumor endothelial cells accelerate tumor metastasis. *Cancer Sci.* **108**, 1921–1926 (2017).
10. Bielenberg, D. R. & Zetter, B. R. The Contribution of Angiogenesis to the Process of Metastasis. *Cancer J.* **21**, 267–273 (2015).
11. Khan, K. A. & Kerbel, R. S. Improving immunotherapy outcomes with anti-angiogenic treatments and vice versa. *Nat. Rev. Clin. Oncol.* **15**, 310–324 (2018).
12. Schaaf, M. B., Garg, A. D. & Agostinis, P. Defining the role of the tumor vasculature in antitumor immunity and immunotherapy. *Cell Death Dis.* **9**, 115 (2018).
13. Dvorak, H. F., Senger, D. R. & Dvorak, A. M. Fibrin as a component of the tumor stroma: origins and biological significance. *Cancer Metastasis Rev.* **2**, 41–73 (1983).
14. Nagy, J. A., Chang, S.-H. H., Shih, S.-C. C., Dvorak, A. M. & Dvorak, H. F. Heterogeneity of the Tumor Vasculature. *Semin. Thromb. Hemost.* **36**, 321–331 (2010).
15. Acerbi, I. *et al.* Human breast cancer invasion and aggression correlates with ECM stiffening and immune cell infiltration. *Integr. Biol.* **7**, 1120–1134 (2015).

16. Levental, K. R. *et al.* Matrix Crosslinking Forces Tumor Progression by Enhancing Integrin Signaling. *Cell* **139**, 891–906 (2009).
17. Lu, P., Weaver, V. M. & Werb, Z. The extracellular matrix: A dynamic niche in cancer progression. *J. Cell Biol.* **196**, 395–406 (2012).
18. Dewhirst, M. W. & Secomb, T. W. Transport of drugs from blood vessels to tumour tissue. *Nat. Rev. Cancer* **17**, 738–750 (2017).
19. Cohen, I. J. & Blasberg, R. Impact of the Tumor Microenvironment on Tumor-Infiltrating Lymphocytes: Focus on Breast Cancer. *Breast Cancer Basic Clin. Res.* **11**, 117822341773156 (2017).
20. Kalluri, R. The biology and function of fibroblasts in cancer. *Nat. Rev. Cancer* **16**, 582–598 (2016).
21. Lohr, M. *et al.* Transforming Growth Factor B1 Induces Desmoplasia in an Experimental Model of Human Pancreatic Carcinoma. *Cancer Research* **61**, (2001).
22. Lijnen, P. & Petrov, V. Transforming growth factor-beta 1-induced collagen production in cultures of cardiac fibroblasts is the result of the appearance of myofibroblasts. *Methods Find. Exp. Clin. Pharmacol.* **24**, 333 (2002).
23. Karakasheva, T. A. *et al.* IL-6 Mediates Cross-Talk between Tumor Cells and Activated Fibroblasts in the Tumor Microenvironment. *Cancer Res.* **78**, 4957–4970 (2018).
24. Chen, X. & Song, E. Turning foes to friends: targeting cancer-associated fibroblasts. *Nat. Rev. Drug Discov.* **18**, 99–115 (2019).
25. Sewell-Loftin, M. K. *et al.* Cancer-associated fibroblasts support vascular growth through mechanical force. *Sci. Rep.* **7**, 12574 (2017).
26. Kakarla, S., Song, X.-T. & Gottschalk, S. Cancer-associated fibroblasts as targets for immunotherapy. *Immunotherapy* **4**, 1129–1138 (2012).
27. Tao, L., Huang, G., Song, H., Chen, Y. & Chen, L. Cancer associated fibroblasts: An essential role in the tumor microenvironment. *Oncol. Lett.* **14**, 2611–2620 (2017).
28. Nozawa, H., Chiu, C. & Hanahan, D. Infiltrating neutrophils mediate the initial angiogenic switch in a mouse model of multistage carcinogenesis. *Proc. Natl. Acad. Sci.* **103**, 12493–12498 (2006).
29. Bekes, E. M. *et al.* Tumor-Recruited Neutrophils and Neutrophil TIMP-Free MMP-9 Regulate Coordinately the Levels of Tumor Angiogenesis and Efficiency of Malignant Cell Intravasation. *Am. J. Pathol.* **179**, 1455–1470 (2011).



30. Zins, K., Abraham, D., Sioud, M. & Aharinejad, S. Colon Cancer Cell–Derived Tumor Necrosis Factor- $\alpha$  Mediates the Tumor Growth–Promoting Response in Macrophages by Up-regulating the Colony-Stimulating Factor-1 Pathway. *Cancer Res.* **67**, 1038–1045 (2007).
31. Chakrabarti, S., Zee, J. M. & Patel, K. D. Regulation of matrix metalloproteinase-9 (MMP-9) in TNF-stimulated neutrophils: novel pathways for tertiary granule release. *J. Leukoc. Biol.* **79**, 214–222 (2006).
32. Shiga, K. *et al.* Cancer-Associated Fibroblasts: Their Characteristics and Their Roles in Tumor Growth. *Cancers (Basel)*. **7**, 2443–2458 (2015).
33. Barleon, B. *et al.* Migration of human monocytes in response to vascular endothelial growth factor (VEGF) is mediated via the VEGF receptor flt-1. *Blood* **87**, 3336–43 (1996).
34. Dineen, S. P. *et al.* Vascular Endothelial Growth Factor Receptor 2 Mediates Macrophage Infiltration into Orthotopic Pancreatic Tumors in Mice. *Cancer Res.* **68**, 4340–4346 (2008).
35. Wheeler, K. C. *et al.* VEGF may contribute to macrophage recruitment and M2 polarization in the decidua. *PLoS One* **13**, e0191040 (2018).
36. Ribatti, D. & Crivellato, E. Immune cells and angiogenesis. *J. Cell. Mol. Med.* **13**, 2822–2833 (2009).
37. Lin, E. Y., Nguyen, A. V., Russell, R. G. & Pollard, J. W. Colony-Stimulating Factor 1 Promotes Progression of Mammary Tumors to Malignancy. *J. Exp. Med.* **193**, 727–740 (2001).
38. Wyckoff, J. B. *et al.* Cancer Research. *Cancer Res.* **62**, 6278–6288 (2007).
39. Yang, L. *et al.* Expansion of myeloid immune suppressor Gr<sup>+</sup>CD11b<sup>+</sup> cells in tumor-bearing host directly promotes tumor angiogenesis. *Cancer Cell* **6**, 409–421 (2004).
40. Shojaei, F. *et al.* Tumor refractoriness to anti-VEGF treatment is mediated by CD11b<sup>+</sup>Gr1<sup>+</sup> myeloid cells. *Nat. Biotechnol.* **25**, 911–20 (2007).
41. Yang, L. *et al.* Abrogation of TGF $\beta$  Signaling in Mammary Carcinomas Recruits Gr<sup>+</sup>1<sup>+</sup>CD11b<sup>+</sup> Myeloid Cells that Promote Metastasis. *Cancer Cell* **13**, 23–35 (2008).
42. Gabrilovich, D. I. Myeloid-Derived Suppressor Cells. *Cancer Immunol. Res.* **5**, 3–8 (2017).
43. Noy, R. & Pollard, J. W. Tumor-Associated Macrophages: From Mechanisms to Therapy. *Immunity* **41**, 49–61 (2014).
44. Binnewies, M. *et al.* Understanding the tumor immune microenvironment (TIME) for effective therapy. *Nat. Med.* **24**, 541–550 (2018).
45. Li, J. *et al.* Tumor Cell-Intrinsic Factors Underlie Heterogeneity of Immune Cell Infiltration and Response to Immunotherapy. *Immunity* **49**, 178–193.e7 (2018).

46. Bonaventura, P. *et al.* Cold Tumors: A Therapeutic Challenge for Immunotherapy. *Front. Immunol.* **10**, 168 (2019).
47. Ribas, A. *et al.* Oncolytic Virotherapy Promotes Intratumoral T Cell Infiltration and Improves Anti-PD-1 Immunotherapy. *Cell* **170**, (2017).
48. Cavallo, F., De Giovanni, C., Nanni, P., Forni, G. & Lollini, P.-L. 2011: the Immune Hallmarks of Cancer. *Cancer Immunol. Immunother.* **60**, 319–26 (2011).
49. Kirchner, H. *et al.* Evidence of Suppressor Cell Activity in Spleens of Mice Bearing Primary Tumors Induced by Moloney Sarcoma Virus. *J. Exp. Med.* **139**, 1473–1487 (1974).
50. Klein, B. Y., Sharon, R., Tarcic, N. & Naor, D. Induction of Antitumor Reactive Cells or Suppressor Cells by Different Molecular Species Isolated from the Same Nonimmunogenic Tumor. *Immunobiology* **163**, 7–21 (1982).
51. Gasocyne, R. D., Whitney, R. B. & Levy, J. G. Recovery of immune competence after tumour resection in mice: correlation with loss of suppressor elements. *Br. J. Cancer* **37**, 190–198 (1978).
52. Young, M. R., Newby, M. & Wepsic, H. T. Hematopoiesis and suppressor bone marrow cells in mice bearing large metastatic Lewis lung carcinoma tumors. *Cancer Res.* **47**, 100–5 (1987).
53. Umansky, V. & Sevko, A. Tumor Microenvironment and Myeloid-Derived Suppressor Cells. *Cancer Microenviron.* **6**, 169–177 (2013).
54. Gong, D. *et al.* TGF $\beta$  signaling plays a critical role in promoting alternative macrophage activation. *BMC Immunol.* **13**, 31 (2012).
55. Travis, M. A. & Sheppard, D. TGF- $\beta$  Activation and Function in Immunity. *Annu. Rev. Immunol.* **32**, 51–82 (2014).
56. Mariathasan, S. *et al.* TGF $\beta$  attenuates tumour response to PD-L1 blockade by contributing to exclusion of T cells. *Nature* **554**, 544–548 (2018).
57. Zhong, Z. *et al.* Anti-Transforming Growth Factor Receptor II Antibody Has Therapeutic Efficacy against Primary Tumor Growth and Metastasis through Multieffects on Cancer, Stroma, and Immune Cells. *Clin. Cancer Res.* **16**, 1191–1205 (2010).
58. Becher, B., Tugues, S. & Greter, M. GM-CSF: From Growth Factor to Central Mediator of Tissue Inflammation. *Immunity* **45**, 963–973 (2016).
59. Dolcetti, L. *et al.* Hierarchy of immunosuppressive strength among myeloid-derived suppressor cell subsets is determined by GM-CSF. *Eur. J. Immunol.* **40**, 22–35 (2009).
60. Parmiani, G. *et al.* Opposite immune functions of GM-CSF administered as vaccine adjuvant in cancer patients. *Ann. Oncol.* **18**, 226–232 (2006).

61. Bronte, V. *et al.* Identification of a CD11b /Gr-1 /CD31 myeloid progenitor capable of activating or suppressing CD8 T cells. (2000).
62. Kaneda, M. M. *et al.* PI3K $\gamma$  is a molecular switch that controls immune suppression. *Nature* **539**, 437–442 (2016).
63. Broughton, S. E. *et al.* The GM-CSF/IL-3/IL-5 cytokine receptor family: from ligand recognition to initiation of signaling. *Immunol. Rev.* **250**, 277–302 (2012).
64. Antony, V. B. *et al.* Recruitment of inflammatory cells to the pleural space. Chemotactic cytokines, IL-8, and monocyte chemotactic peptide-1 in human pleural fluids. *J. Immunol.* **151**, 7216–23 (1993).
65. Chang, A. L. *et al.* CCL2 Produced by the Glioma Microenvironment Is Essential for the Recruitment of Regulatory T Cells and Myeloid-Derived Suppressor Cells. *Cancer Res.* **76**, 5671–5682 (2016).
66. Balch, C. M., Dougherty, P. A. & Tilden, A. B. Excessive Prostaglandin E2 Production by Suppressor Monocytes in Head and Neck Cancer Patients. *Ann. Surg.* **196**, 645–650 (1982).
67. Sinha, P., Clements, V. K., Fulton, A. M. & Ostrand-Rosenberg, S. Prostaglandin E2 Promotes Tumor Progression by Inducing Myeloid-Derived Suppressor Cells. *Cancer Res.* **67**, 4507–4513 (2007).
68. Freeman, G. J. *et al.* Engagement of the Pd-1 Immunoinhibitory Receptor by a Novel B7 Family Member Leads to Negative Regulation of Lymphocyte Activation. *J. Exp. Med.* **192**, 1027–1034 (2000).
69. Latchman, Y. *et al.* PD-L2 is a second ligand for PD-1 and inhibits T cell activation. *Nat. Immunol.* **2**, 261–268 (2001).
70. Mazanet, M. M. & Hughes, C. C. W. B7-H1 Is Expressed by Human Endothelial Cells and Suppresses T Cell Cytokine Synthesis. *J. Immunol.* **169**, 3581–3588 (2002).
71. Bennett, F. *et al.* Program Death-1 Engagement Upon TCR Activation Has Distinct Effects on Costimulation and Cytokine-Driven Proliferation: Attenuation of ICOS, IL-4, and IL-21, But Not CD28, IL-7, and IL-15 Responses. *J. Immunol.* **170**, 711–718 (2003).
72. Fuller, M. J. & Zajac, A. J. Ablation of CD8 and CD4 T Cell Responses by High Viral Loads. *J. Immunol.* **170**, 477–486 (2003).
73. Wherry, E. J., Blattman, J. N., Murali-Krishna, K., van der Most, R. & Ahmed, R. Viral Persistence Alters CD8 T-Cell Immunodominance and Tissue Distribution and Results in Distinct Stages of Functional Impairment. *J. Virol.* **77**, 4911–4927 (2003).
74. Ghebeh, H. *et al.* The B7-H1 (PD-L1) T Lymphocyte-Inhibitory Molecule Is Expressed in Breast Cancer Patients with Infiltrating Ductal Carcinoma: Correlation with Important High-Risk Prognostic Factors. *Neoplasia* **8**, 190–198 (2006).

75. Ohigashi, Y. Clinical Significance of Programmed Death-1 Ligand-1 and Programmed Death-1 Ligand-2 Expression in Human Esophageal Cancer. *Clin. Cancer Res.* **11**, 2947–2953 (2005).
76. Hamanishi, J. *et al.* Programmed cell death 1 ligand 1 and tumor-infiltrating CD8<sup>+</sup> T lymphocytes are prognostic factors of human ovarian cancer. *Proc. Natl. Acad. Sci.* **104**, 3360–3365 (2007).
77. Nakanishi, J. *et al.* Overexpression of B7-H1 (PD-L1) significantly associates with tumor grade and postoperative prognosis in human urothelial cancers. *Cancer Immunol. Immunother.* **56**, 1173–1182 (2007).
78. Iwai, Y. *et al.* Involvement of PD-L1 on tumor cells in the escape from host immune system and tumor immunotherapy by PD-L1 blockade. *Proc. Natl. Acad. Sci.* **99**, 12293–12297 (2002).
79. Gong, J., Chehrazi-Raffle, A., Reddi, S. & Salgia, R. Development of PD-1 and PD-L1 inhibitors as a form of cancer immunotherapy: a comprehensive review of registration trials and future considerations. *J. Immunother. Cancer* **6**, 8 (2018).
80. Zhang, T. *et al.* The efficacy and safety of anti-PD-1/PD-L1 antibodies for treatment of advanced or refractory cancers: a meta-analysis. *Oncotarget* **7**, 73068–73079 (2016).
81. Weber, R. *et al.* Myeloid-Derived Suppressor Cells Hinder the Anti-Cancer Activity of Immune Checkpoint Inhibitors. *Front. Immunol.* **9**, 1310 (2018).
82. Mantovani, A., Marchesi, F., Malesci, A., Laghi, L. & Allavena, P. Tumour-associated macrophages as treatment targets in oncology. *Nat. Rev. Clin. Oncol.* **14**, 399–416 (2017).
83. Yamazaki, T. *et al.* Expression of Programmed Death 1 Ligands by Murine T Cells and APC. *J. Immunol.* **169**, 5538–5545 (2002).
84. Youn, J.-I., Nagaraj, S., Collazo, M. & Gabrilovich, D. I. Subsets of Myeloid-Derived Suppressor Cells in Tumor-Bearing Mice. *J. Immunol.* **181**, 5791–5802 (2008).
85. Highfill, S. L. *et al.* Disruption of CXCR2-Mediated MDSC Tumor Trafficking Enhances Anti-PD1 Efficacy. *Sci. Transl. Med.* **6**, 237ra67-237ra67 (2014).
86. Kim, H. *et al.* Combination of Sunitinib and PD-L1 Blockade Enhances Anticancer Efficacy of TLR7/8 Agonist-Based Nanovaccine. *Mol. Pharm.* **16**, 1200–1210 (2019).
87. Guerriero, J. L. *et al.* Class IIa HDAC inhibition reduces breast tumours and metastases through anti-tumour macrophages. *Nature* **543**, 428–432 (2017).
88. Levy, R. B., Waksal, S. D. & Shearer, G. M. Correlation of suppressor cell development in parental and F1 hybrid mouse strains with the growth of a parental tumor in vivo. *J. Exp. Med.* **144**, 1363–1368 (1976).

89. Zembala, M., Mytar, B., Popiela, T. & Asherson, G. L. Depressed in vitro peripheral blood lymphocyte response to mitogens in cancer patients: The role of suppressor cells. *Int. J. Cancer* **19**, 605–613 (1977).
90. Quan, P. C. & Burtin, P. *Demonstration of Nonspecific Suppressor Cells in the Peripheral Lymphocytes of Cancer Patients*. (1978).
91. Bennett, J. A., Rao, V. S. & Mitchell, M. S. Systemic bacillus Calmette-Guérin (BCG) activates natural suppressor cells. *Proc. Natl. Acad. Sci.* **75**, 5142–4 (1978).
92. Maier, T., Holda, J. H. & Claman, H. N. Murine natural suppressor cells in the newborn, in bone marrow, and after cyclophosphamide. Genetic variations and dependence on IFN- $\gamma$ . *J. Immunol.* **143**, 491–8 (1989).
93. Hertel-Wulff, B., Okada, S., Oseroff, A. & Strober, S. In vitro propagation and cloning of murine natural suppressor (NS) cells. *J. Immunol.* **133**, 2791–6 (1984).
94. Moore, S. C., Shaw, M. A. & Soderberg, L. S. F. Transforming growth factor- $\beta$  is the major mediator of natural suppressor cells derived from normal bone marrow. *J. Leukoc. Biol.* **52**, 596–601 (1992).
95. Sykes, M., Sharabi, Y. & Sachs, D. H. Natural suppressor cells in spleens of irradiated, bone marrow-reconstituted mice and normal bone marrow: lack of Sca-1 expression and enrichment by depletion of Mac1-positive cells. *Cell. Immunol.* **127**, 260–74 (1990).
96. Sugiura, K. *et al.* Characterization of Natural Suppressor Cells in Human Bone Marrow. *Stem Cells* **16**, 99–106 (1998).
97. Young, M. R. I. *et al.* Increased recurrence and metastasis in patients whose primary head and neck squamous cell carcinomas secreted granulocyte-macrophage colony-stimulating factor and contained CD34<sup>+</sup> natural suppressor cells. *Int. J. Cancer* **74**, 69–74 (1997).
98. Movahedi, K. *et al.* Identification of discrete tumor-induced myeloid-derived suppressor cell subpopulations with distinct T cell-suppressive activity. *Blood* **111**, 4233–4244 (2008).
99. Almand, B. *et al.* Increased Production of Immature Myeloid Cells in Cancer Patients: A Mechanism of Immunosuppression in Cancer. *J. Immunol.* **166**, 678–689 (2001).
100. Bronte, V. *et al.* Apoptotic death of CD8<sup>+</sup> T lymphocytes after immunization: induction of a suppressive population of Mac-1<sup>+</sup>/Gr-1<sup>+</sup> cells. *J. Immunol.* **161**, 5313–20 (1998).
101. Hoechst, B. *et al.* Myeloid derived suppressor cells inhibit natural killer cells in patients with hepatocellular carcinoma via the NKGp30 receptor. *Hepatology* **50**, 799–807 (2009).
102. Liu, C. *et al.* Expansion of spleen myeloid suppressor cells represses NK cell cytotoxicity in tumor-bearing host. *Blood* **109**, 4336–4342 (2007).
103. Crook, K. R. *et al.* Myeloid-derived suppressor cells regulate T cell and B cell responses during autoimmune disease. *J. Leukoc. Biol.* **97**, 573–582 (2015).

104. Mandruzzato, S. *et al.* Toward harmonized phenotyping of human myeloid-derived suppressor cells by flow cytometry: results from an interim study. *Cancer Immunol. Immunother.* **65**, 161–169 (2016).
105. Bronte, V. *et al.* Recommendations for myeloid-derived suppressor cell nomenclature and characterization standards. *Nat. Commun.* **7**, 12150 (2016).
106. Bian, Z. *et al.* Arginase-1 is neither constitutively expressed in nor required for myeloid-derived suppressor cell-mediated inhibition of T-cell proliferation. *Eur. J. Immunol.* **48**, 1046–1058 (2018).
107. Kusmartsev, S., Nefedova, Y., Yoder, D. & Gabrilovich, D. I. Antigen-Specific Inhibition of CD8 + T Cell Response by Immature Myeloid Cells in Cancer Is Mediated by Reactive Oxygen Species. *J. Immunol.* **172**, 989–999 (2004).
108. Nagaraj, S. *et al.* Altered recognition of antigen is a mechanism of CD8+ T cell tolerance in cancer. *Nat. Med.* **13**, 828–835 (2007).
109. Feng, S. *et al.* Myeloid-derived suppressor cells inhibit T cell activation through nitrating LCK in mouse cancers. *Proc. Natl. Acad. Sci.* **115**, 10094–10099 (2018).
110. Bronte, V. *et al.* IL-4-Induced Arginase 1 Suppresses Alloreactive T Cells in Tumor-Bearing Mice. *J. Immunol.* **170**, 270–278 (2003).
111. Sinha, P., Clements, V. K., Bunt, S. K., Albelda, S. M. & Ostrand-Rosenberg, S. Cross-Talk between Myeloid-Derived Suppressor Cells and Macrophages Subverts Tumor Immunity toward a Type 2 Response. *J. Immunol.* **179**, 977–983 (2007).
112. Park, M.-J. *et al.* Interleukin-10 produced by myeloid-derived suppressor cells is critical for the induction of Tregs and attenuation of rheumatoid inflammation in mice. *Sci. Rep.* **8**, 3753 (2018).
113. Ostrand-Rosenberg, S. & Sinha, P. Myeloid-Derived Suppressor Cells: Linking Inflammation and Cancer. *J. Immunol.* **182**, 4499–4506 (2009).
114. De Almeida Nagata, D. E., Chiang, E. Y., Magnuson, S., Gascoigne, K. E. & Grogan Correspondence, J. L. Regulation of Tumor-Associated Myeloid Cell Activity by CBP/EP300 Bromodomain Modulation of H3K27 Acetylation Graphical Abstract Highlights d The CBP/EP300 bromodomain (BRD) regulates myeloid-derived suppressor cells (MDSCs) d CBP/EP300-BRD controls H3K27 acetylation in intratumoral MDSCs d CBP/EP300-BRD modulates MDSC-associated genes and regulates their function d Inhibition of CBP/EP300-BRD promotes inflammatory MDSCs and attenuates tumor growth. *Cell Rep.* **27**, 269–281 (2019).
115. Toor, S. M. *et al.* Myeloid cells in circulation and tumor microenvironment of breast cancer patients. *Cancer Immunol. Immunother.* **66**, 753–764 (2017).

116. Gielen, P. R. *et al.* Elevated levels of polymorphonuclear myeloid-derived suppressor cells in patients with glioblastoma highly express S100A8/9 and arginase and suppress T cell function. *Neuro. Oncol.* **18**, 1253–64 (2016).
117. Haverkamp, J. M., Crist, S. A., Elzey, B. D., Cimen, C. & Ratliff, T. L. In vivo suppressive function of myeloid-derived suppressor cells is limited to the inflammatory site. *Eur. J. Immunol.* **41**, 749–759 (2011).
118. Kumar, V., Patel, S., Tcyganov, E. & Gabrilovich, D. I. The Nature of Myeloid-Derived Suppressor Cells in the Tumor Microenvironment. *Trends Immunol.* **37**, 208–220 (2016).
119. Solito, S. *et al.* Myeloid-derived suppressor cell heterogeneity in human cancers. *Ann. N. Y. Acad. Sci.* **1319**, 47–65 (2014).
120. Corzo, C. A. *et al.* HIF-1 $\alpha$  regulates function and differentiation of myeloid-derived suppressor cells in the tumor microenvironment. *J. Exp. Med.* **207**, 2439–2453 (2010).
121. Zhang, Q. *et al.* Prognostic Significance of Tumor-Associated Macrophages in Solid Tumor: A Meta-Analysis of the Literature. *PLoS One* **7**, e50946 (2012).
122. Solinas, G., Germano, G., Mantovani, A. & Allavena, P. Tumor-associated macrophages (TAM) as major players of the cancer-related inflammation. *J. Leukoc. Biol.* **86**, 1065–1073 (2009).
123. Weigert, A. & Brüne, B. Nitric oxide, apoptosis and macrophage polarization during tumor progression. *Nitric Oxide* **19**, 95–102 (2008).
124. Lu, G. *et al.* Myeloid cell-derived inducible nitric oxide synthase suppresses M1 macrophage polarization. *Nat. Commun.* **6**, 6676 (2015).
125. Movahedi, K. *et al.* Different Tumor Microenvironments Contain Functionally Distinct Subsets of Macrophages Derived from Ly6C(high) Monocytes. *Cancer Res.* **70**, 5728–5739 (2010).
126. Laoui, D. *et al.* Tumor Hypoxia Does Not Drive Differentiation of Tumor-Associated Macrophages but Rather Fine-Tunes the M2-like Macrophage Population. *Cancer Res.* **74**, 24–30 (2014).
127. Heusinkveld, M. & van der Burg, S. H. Identification and manipulation of tumor associated macrophages in human cancers. *J. Transl. Med.* **9**, 216 (2011).
128. Qian, B.-Z. & Pollard, J. W. Macrophage Diversity Enhances Tumor Progression and Metastasis. *Cell* **141**, 39–51 (2010).
129. Xue, J. *et al.* Transcriptome-Based Network Analysis Reveals a Spectrum Model of Human Macrophage Activation. *Immunity* **40**, 274–288 (2014).
130. Sica, A. *et al.* Autocrine Production of IL-10 Mediates Defective IL-12 Production and NF- $\kappa$ B Activation in Tumor-Associated Macrophages. *J. Immunol.* **164**, 762–767 (2000).

131. Saccani, A. *et al.* p50 Nuclear Factor- $\kappa$ B Overexpression in Tumor-Associated Macrophages Inhibits M1 Inflammatory Responses and Antitumor Resistance. *Cancer Res.* **66**, 11432–11440 (2006).
132. Kratochvill, F. *et al.* TNF Counterbalances the Emergence of M2 Tumor Macrophages. *Cell Rep.* **12**, 1902–1914 (2015).
133. Kusmartsev, S. & Gabrilovich, D. I. Cell Deletion Tumor-Associated Macrophage-Mediated T STAT1 Signaling Regulates. *J Immunol Ref.* **174**, 4880–4891 (2005).
134. Prima, V., Kaliberova, L. N., Kaliberov, S., Curiel, D. T. & Kusmartsev, S. COX2/mPGES1/PGE<sub>2</sub> pathway regulates PD-L1 expression in tumor-associated macrophages and myeloid-derived suppressor cells. *Proc. Natl. Acad. Sci.* **114**, 1117–1122 (2017).
135. Noman, M. Z. *et al.* PD-L1 is a novel direct target of HIF-1 $\alpha$ , and its blockade under hypoxia enhanced MDSC-mediated T cell activation. *J. Exp. Med.* **211**, 781–790 (2014).
136. Zhu, Q., Wu, X., Wu, Y. & Wang, X. Interaction between Treg cells and tumor-associated macrophages in the tumor microenvironment of epithelial ovarian cancer. *Oncol. Rep.* **36**, 3472–3478 (2016).
137. Liu, J. *et al.* Tumor-Associated Macrophages Recruit CCR6<sup>+</sup> Regulatory T Cells and Promote the Development of Colorectal Cancer via Enhancing CCL20 Production in Mice. *PLoS One* **6**, e19495 (2011).
138. Lewis, J. S., Landers, R. J., Underwood, J. C., Harris, A. L. & Lewis, C. E. Expression of vascular endothelial growth factor by macrophages is up-regulated in poorly vascularized areas of breast carcinomas. *J. Pathol.* **192**, 150–8 (2000).
139. Lin, L. *et al.* CCL18 from tumor-associated macrophages promotes angiogenesis in breast cancer. *Oncotarget* **6**, 34758–73 (2015).
140. Hughes, R. *et al.* Perivascular M2 Macrophages Stimulate Tumor Relapse after Chemotherapy. *Cancer Res.* **75**, 3479–3491 (2015).
141. Morales, J. K., Kmieciak, M., Knutson, K. L., Bear, H. D. & Manjili, M. H. GM-CSF is one of the main breast tumor-derived soluble factors involved in the differentiation of CD11b-Gr1<sup>+</sup> bone marrow progenitor cells into myeloid-derived suppressor cells. *Breast Cancer Res. Treat.* **123**, 39–49 (2010).
142. Bronte, V. *et al.* Unopposed production of granulocyte-macrophage colony-stimulating factor by tumors inhibits CD8<sup>+</sup> T cell responses by dysregulating antigen-presenting cell maturation. *J. Immunol.* **162**, 5728–5737 (1999).
143. Condamine, T., Mastio, J. & Gabrilovich, D. I. Transcriptional regulation of myeloid-derived suppressor cells. *J. Leukoc. Biol.* **98**, 913–922 (2015).



144. Lesokhin, A. M. *et al.* Monocytic CCR2+ Myeloid-Derived Suppressor Cells Promote Immune Escape by Limiting Activated CD8 T-cell Infiltration into the Tumor Microenvironment. *Cancer Res.* **72**, 876–886 (2012).
145. Blattner, C. *et al.* CCR5 + Myeloid-Derived Suppressor Cells Are Enriched and Activated in Melanoma Lesions. *Cancer Res.* **78**, 157–167 (2018).
146. Umansky, V., Blattner, C., Gebhardt, C. & Utikal, J. CCR5 in recruitment and activation of myeloid-derived suppressor cells in melanoma. *Cancer Immunol. Immunother.* **66**, 1015–1023 (2017).
147. Franklin, R. A. *et al.* The cellular and molecular origin of tumor-associated macrophages. *Science* (80-. ). **344**, 921–925 (2014).
148. De, I. *et al.* CSF1 Overexpression Promotes High-Grade Glioma Formation without Impacting the Polarization Status of Glioma-Associated Microglia and Macrophages. *Cancer Res.* **76**, 2552–2560 (2016).
149. Linde, N. *et al.* Vascular endothelial growth factor-induced skin carcinogenesis depends on recruitment and alternative activation of macrophages. *J. Pathol.* **227**, 17–28 (2012).
150. Franklin, R. A. & Li, M. O. Ontogeny of Tumor-Associated Macrophages and Its Implication in Cancer Regulation. *Trends in Cancer* **2**, 20–34 (2016).
151. Wang, Y.-C. *et al.* Notch Signaling Determines the M1 versus M2 Polarization of Macrophages in Antitumor Immune Responses. *Cancer Res.* **70**, 4840–4849 (2010).
152. Zhu, Y. *et al.* Tissue-Resident Macrophages in Pancreatic Ductal Adenocarcinoma Originate from Embryonic Hematopoiesis and Promote Tumor Progression. *Immunity* **47**, 323–338.e6 (2017).
153. Kumar, V. *et al.* CD45 Phosphatase Inhibits STAT3 Transcription Factor Activity in Myeloid Cells and Promotes Tumor-Associated Macrophage Differentiation. *Immunity* **44**, 303–315 (2016).
154. Liu, G. *et al.* SIRT1 Limits the Function and Fate of Myeloid-Derived Suppressor Cells in Tumors by Orchestrating HIF-1 -Dependent Glycolysis. *Cancer Res.* **74**, 727–737 (2014).
155. Spinetti, T. *et al.* TLR7-based cancer immunotherapy decreases intratumoral myeloid-derived suppressor cells and blocks their immunosuppressive function. *Oncoimmunology* **5**, e1230578 (2016).
156. Ko, J. S. *et al.* Sunitinib Mediates Reversal of Myeloid-Derived Suppressor Cell Accumulation in Renal Cell Carcinoma Patients. *Clin. Cancer Res.* **15**, 2148–2157 (2009).
157. Ko, J. S. *et al.* Direct and Differential Suppression of Myeloid-Derived Suppressor Cell Subsets by Sunitinib Is Compartmentally Constrained. *Cancer Res.* **70**, 3526–3536 (2010).

158. Suzuki, E., Kapoor, V., Jassar, A. S., Kaiser, L. R. & Albelda, S. M. Gemcitabine selectively eliminates splenic Gr-1<sup>+</sup>/CD11b<sup>+</sup> myeloid suppressor cells in tumor-bearing animals and enhances antitumor immune activity. *Clin. Cancer Res.* **11**, 6713–21 (2005).
159. Eriksson, E., Wenthe, J., Irenaeus, S., Loskog, A. & Ullenhag, G. Gemcitabine reduces MDSCs, tregs and TGF $\beta$ -1 while restoring the teff/treg ratio in patients with pancreatic cancer. *J. Transl. Med.* **14**, 282 (2016).
160. Vincent, J. *et al.* 5-Fluorouracil Selectively Kills Tumor-Associated Myeloid-Derived Suppressor Cells Resulting in Enhanced T Cell-Dependent Antitumor Immunity. *Cancer Res.* **70**, 3052–3061 (2010).
161. Srivastava, M. K. *et al.* Myeloid Suppressor Cell Depletion Augments Antitumor Activity in Lung Cancer. *PLoS One* **7**, e40677 (2012).
162. Sinha, P. *et al.* Proinflammatory S100 Proteins Regulate the Accumulation of Myeloid-Derived Suppressor Cells. *J. Immunol.* **181**, 4666–4675 (2008).
163. Qin, H. *et al.* Generation of a new therapeutic peptide that depletes myeloid-derived suppressor cells in tumor-bearing mice. *Nat. Med.* **20**, 676–681 (2014).
164. Priceman, S. J. *et al.* Targeting distinct tumor-infiltrating myeloid cells by inhibiting CSF-1 receptor: combating tumor evasion of antiangiogenic therapy. *Blood* **115**, 1461–1471 (2010).
165. Xu, J. *et al.* CSF1R Signaling Blockade Stanches Tumor-Infiltrating Myeloid Cells and Improves the Efficacy of Radiotherapy in Prostate Cancer. *Cancer Res.* **73**, 2782–2794 (2013).
166. Mok, S. *et al.* Inhibition of CSF-1 Receptor Improves the Antitumor Efficacy of Adoptive Cell Transfer Immunotherapy. *Cancer Res.* **74**, 153–161 (2014).
167. Zhao, L. *et al.* Recruitment of a myeloid cell subset (CD11b/Gr1 mid ) via CCL2/CCR2 promotes the development of colorectal cancer liver metastasis\*. *Hepatology* **57**, 829–839 (2013).
168. Teng, K.-Y. *et al.* Blocking the CCL2–CCR2 Axis Using CCL2-Neutralizing Antibody Is an Effective Therapy for Hepatocellular Cancer in a Mouse Model. *Mol. Cancer Ther.* **16**, 312–322 (2017).
169. Fridlender, Z. G. *et al.* CCL2 Blockade Augments Cancer Immunotherapy. *Cancer Res.* **70**, 109–118 (2010).
170. Lim, S. Y., Yuzhalin, A. E., Gordon-Weeks, A. N. & Muschel, R. J. Targeting the CCL2-CCR2 signaling axis in cancer metastasis. *Oncotarget* **7**, 28697–28710 (2016).
171. Mirza, N. *et al.* All-trans -Retinoic Acid Improves Differentiation of Myeloid Cells and Immune Response in Cancer Patients. *Cancer Res.* **66**, 9299–9307 (2006).

172. Nefedova, Y. *et al.* Mechanism of All- Trans Retinoic Acid Effect on Tumor-Associated Myeloid-Derived Suppressor Cells. *Cancer Res.* **67**, 11021–11028 (2007).
173. Iclozan, C., Antonia, S., Chiappori, A., Chen, D.-T. & Gabrilovich, D. Therapeutic regulation of myeloid-derived suppressor cells and immune response to cancer vaccine in patients with extensive stage small cell lung cancer. *Cancer Immunol. Immunother.* **62**, 909–918 (2013).
174. Rita Young Joe Ihm Yvonne Lozano Mark A Wright, M. I., Margaret Prechel, M., I Young, M. R., Ihm Lozano M A Wright, J. Y. & I Young M M Prechel, M. R. *Treating tumor-bearing mice with vitamin D 3 diminishes tumor-induced myelopoiesis and associated immunosuppression, and reduces tumor metastasis and recurrence.* *Cancer Immunol Immunother* **41**, (Springer-Verlag, 1995).
175. Ryan D Calvert, Grant N Burcham, Timothy L Ratliff, and J. C. F. Myeloid Derived Suppressor Cells (MDSC) Are Vitamin D Targets and 1 $\alpha$ , 25 Dihydroxyvitamin D (1,25(OH)2D) Inhibits their Ability to Suppress T Cell Function. *The FASEB Journal* **31**, 434.8 (2017).
176. Serafini, P. *et al.* Phosphodiesterase-5 inhibition augments endogenous antitumor immunity by reducing myeloid-derived suppressor cell function. *J. Exp. Med.* **203**, 2691–2702 (2006).
177. Orillion, A. *et al.* Entinostat Neutralizes Myeloid-Derived Suppressor Cells and Enhances the Antitumor Effect of PD-1 Inhibition in Murine Models of Lung and Renal Cell Carcinoma. *Clin. Cancer Res.* **23**, 5187–5201 (2017).
178. Fiorucci, S. *et al.* IL-1 beta converting enzyme is a target for nitric oxide-releasing aspirin: new insights in the antiinflammatory mechanism of nitric oxide-releasing nonsteroidal antiinflammatory drugs. *J. Immunol.* **165**, 5245–54 (2000).
179. De Santo, C. *et al.* Nitroaspirin corrects immune dysfunction in tumor-bearing hosts and promotes tumor eradication by cancer vaccination. *Proc. Natl. Acad. Sci.* **102**, 4185–4190 (2005).
180. Van Acker, H. H., Anguille, S., Willemen, Y., Smits, E. L. & Van Tendeloo, V. F. Bisphosphonates for cancer treatment: Mechanisms of action and lessons from clinical trials. *Pharmacol. Ther.* **158**, 24–40 (2016).
181. Coscia, M. *et al.* Zoledronic acid repolarizes tumour-associated macrophages and inhibits mammary carcinogenesis by targeting the mevalonate pathway. *J. Cell. Mol. Med.* **14**, 2803–2815 (2010).
182. Germano, G. *et al.* Role of Macrophage Targeting in the Antitumor Activity of Trabectedin. *Cancer Cell* **23**, 249–262 (2013).
183. Galmbacher, K. *et al.* Shigella Mediated Depletion of Macrophages in a Murine Breast Cancer Model Is Associated with Tumor Regression. *PLoS One* **5**, e9572 (2010).

184. Nagai, T. *et al.* Targeting tumor-associated macrophages in an experimental glioma model with a recombinant immunotoxin to folate receptor  $\beta$ . *Cancer Immunol. Immunother.* **58**, 1577–1586 (2009).
185. Monti, P. *et al.* The CC chemokine MCP-1/CCL2 in pancreatic cancer progression: regulation of expression and potential mechanisms of antimalignant activity. *Cancer Res.* **63**, 7451–61 (2003).
186. Ries, C. H. *et al.* Targeting Tumor-Associated Macrophages with Anti-CSF-1R Antibody Reveals a Strategy for Cancer Therapy. *Cancer Cell* **25**, 846–859 (2014).
187. Arwert, E. N. *et al.* A Unidirectional Transition from Migratory to Perivascular Macrophage Is Required for Tumor Cell Intravasation. *Cell Rep.* **23**, 1239–1248 (2018).
188. Sanchez-Martin, L. *et al.* The chemokine CXCL12 regulates monocyte-macrophage differentiation and RUNX3 expression. *Blood* **117**, 88–97 (2011).
189. Wong, D., Kandagatla, P., Korz, W. & Chinni, S. R. Targeting CXCR4 with CTCE-9908 inhibits prostate tumor metastasis. *BMC Urol.* **14**, 12 (2014).
190. Huang, E. H. *et al.* A CXCR4 Antagonist CTCE-9908 Inhibits Primary Tumor Growth and Metastasis of Breast Cancer. *J. Surg. Res.* **155**, 231–236 (2009).
191. Ngambenjawong, C., Gustafson, H. H. & Pun, S. H. Progress in tumor-associated macrophage (TAM)-targeted therapeutics. *Adv. Drug Deliv. Rev.* **114**, 206–221 (2017).
192. Hussain, S. F. *et al.* A Novel Small Molecule Inhibitor of Signal Transducers and Activators of Transcription 3 Reverses Immune Tolerance in Malignant Glioma Patients. *Cancer Res.* **67**, 9630–9636 (2007).
193. Xin, H. *et al.* Sunitinib Inhibition of Stat3 Induces Renal Cell Carcinoma Tumor Cell Apoptosis and Reduces Immunosuppressive Cells. *Cancer Res.* **69**, 2506–2513 (2009).
194. Sinha, P., Clements, V. K. & Ostrand-Rosenberg, S. Reduction of Myeloid-Derived Suppressor Cells and Induction of M1 Macrophages Facilitate the Rejection of Established Metastatic Disease. *J. Immunol.* **174**, 636–645 (2005).
195. Dong, R. *et al.* The involvement of M2 macrophage polarization inhibition in fenretinide-mediated chemopreventive effects on colon cancer. *Cancer Lett.* **388**, 43–53 (2017).
196. Sahin, E. *et al.* Macrophage PTEN Regulates Expression and Secretion of Arginase I Modulating Innate and Adaptive Immune Responses. *J. Immunol.* **193**, 1717–1727 (2014).
197. Chen, W. *et al.* Macrophage-induced tumor angiogenesis is regulated by the TSC2-mTOR pathway. *Cancer Res.* **72**, 1363–72 (2012).
198. Mertens, C. *et al.* Intracellular Iron Chelation Modulates the Macrophage Iron Phenotype with Consequences on Tumor Progression. *PLoS One* **11**, e0166164 (2016).

199. Richardson, D. R., Kalinowski, D. S., Lau, S., Jansson, P. J. & Lovejoy, D. B. Cancer cell iron metabolism and the development of potent iron chelators as anti-tumour agents. *BBA - Gen. Subj.* **1790**, 702–717 (2008).
200. Zanganeh, S. *et al.* Iron oxide nanoparticles inhibit tumour growth by inducing pro-inflammatory macrophage polarization in tumour tissues. *Nat. Nanotechnol.* **11**, 986–994 (2016).
201. Bruns, H. *et al.* Vitamin D-dependent induction of cathelicidin in human macrophages results in cytotoxicity against high-grade B cell lymphoma. *Sci. Transl. Med.* **7**, 282ra47–282ra47 (2015).
202. Puig-Kröger, A. *et al.* Folate Receptor  $\beta$  Is Expressed by Tumor-Associated Macrophages and Constitutes a Marker for M2 Anti-inflammatory/ Regulatory Macrophages. (2009). doi:10.1158/0008-5472.CAN-09-2050
203. Shen, J. *et al.* Assessment of folate receptor- $\beta$  expression in human neoplastic tissues. *Oncotarget* **6**, 14700–9 (2015).
204. Hu, Y. *et al.* Depletion of activated macrophages with a folate receptor-beta-specific antibody improves symptoms in mouse models of rheumatoid arthritis. *Arthritis Res. Ther.* **21**, 143 (2019).
205. Lee, M., Rey, K., Besler, K., Wang, C. & Choy, J. in 181–207 (Springer, Cham, 2017). doi:10.1007/978-3-319-54090-0\_8
206. Bozkus, C. C., Elzey, B. D., Crist, S. A., Ellies, L. G. & Ratliff, T. L. Expression of Cationic Amino Acid Transporter 2 Is Required for Myeloid-Derived Suppressor Cell-Mediated Control of T Cell Immunity. *J. Immunol.* **195**, 5237–5250 (2015).
207. PeÑarando, J., Aranda, E. & Rodríguez-Ariza, A. Immunomodulatory roles of nitric oxide in cancer: tumor microenvironment says “NO” to antitumor immune response. *Transl. Res.* **210**, 99–108 (2019).
208. Kimura, H. *et al.* Hypoxia response element of the human vascular endothelial growth factor gene mediates transcriptional regulation by nitric oxide: control of hypoxia-inducible factor-1 activity by nitric oxide.
209. Molon, B. *et al.* Chemokine nitration prevents intratumoral infiltration of antigen-specific T cells. *J. Exp. Med.* **208**, 1949–62 (2011).
210. Madhurantakam, C., Duru, A. D., Sandalova, T., Webb, J. R. & Achour, A. Inflammation-Associated Nitrotyrosination Affects TCR Recognition through Reduced Stability and Alteration of the Molecular Surface of the MHC Complex. *PLoS One* **7**, e32805 (2012).

211. Hardy, L. L., Wick, D. A. & Webb, J. R. Conversion of Tyrosine to the Inflammation-Associated Analog 3'-Nitrotyrosine at Either TCR- or MHC-Contact Positions Can Profoundly Affect Recognition of the MHC Class I-Restricted Epitope of Lymphocytic Choriomeningitis Virus Glycoprotein 33 by CD8 T Cells. *J. Immunol.* **180**, 5956–5962 (2008).
212. Bingisser, R. M., Tilbrook, P. A., Holt, P. G. & Kees, U. R. Macrophage-derived nitric oxide regulates T cell activation via reversible disruption of the Jak3/STAT5 signaling pathway. *J. Immunol.* **160**, 5729–34 (1998).
213. Jayaraman, P. *et al.* Cancer Therapy: Preclinical iNOS Expression in CD4<sup>+</sup> T Cells Limits Treg Induction by Repressing TGF $\beta$ 1: Combined iNOS Inhibition and Treg Depletion Unmask Endogenous Antitumor Immunity. *Clin Cancer Res* **20**, (2014).
214. Ito, H., Ando, T., Ogiso, H., Arioka, Y. & Seishima, M. Inhibition of induced nitric oxide synthase enhances the anti-tumor effects on cancer immunotherapy using TLR7 agonist in mice. *Cancer Immunol. Immunother.* **64**, 429–436 (2015).
215. Cinelli, M. A., Do, H. T., Miley, G. P. & Silverman, R. B. Inducible nitric oxide synthase: Regulation, structure, and inhibition. *Med. Res. Rev.* (2019). doi:10.1002/med.21599
216. Agostinis, P. *et al.* Photodynamic therapy of cancer: an update. *CA. Cancer J. Clin.* **61**, 250–81 (2011).
217. Mroz, P., Yaroslavsky, A., Kharkwal, G. B. & Hamblin, M. R. Cell death pathways in photodynamic therapy of cancer. *Cancers (Basel)*. **3**, 2516–39 (2011).
218. Dolmans, D. E. J. G. J., Fukumura, D. & Jain, R. K. Photodynamic therapy for cancer. *Nat. Rev. Cancer* **3**, 380–387 (2003).
219. The influence of photodynamic therapy on the immune response. *Photodiagnosis Photodyn. Ther.* **2**, 283–298 (2005).
220. Predina, J. D. *et al.* Identification of a Folate Receptor-Targeted Near-Infrared Molecular Contrast Agent to Localize Pulmonary Adenocarcinomas. *Mol. Ther.* **26**, 390 (2018).
221. Martino, A. *et al.* Mycobacterium bovis Bacillus Calmette-Guerin Vaccination Mobilizes Innate Myeloid-Derived Suppressor Cells Restraining In Vivo T Cell Priming via IL-1R-Dependent Nitric Oxide Production. *J. Immunol.* **184**, 2038–2047 (2010).
222. Griffith, T. S. *et al.* Inhibition of Murine Prostate Tumor Growth and Activation of Immunoregulatory Cells With Recombinant Canarypox Viruses. *JNCI J. Natl. Cancer Inst.* **93**, 998–1007 (2001).
223. Loskog, A. *et al.* Optimization of the MB49 mouse bladder cancer model for adenoviral gene therapy. *Lab. Anim.* **39**, 384–393 (2005).
224. Demidova, T. N. & Hamblin, M. R. Macrophage-targeted photodynamic therapy. *Int. J. Immunopathol. Pharmacol.* **17**, 117–26 (2004).

225. Hayashi, N. *et al.* A Novel Photodynamic Therapy Targeting Cancer Cells and Tumor-Associated Macrophages. *Mol. Cancer Ther.* **14**, 452–460 (2015).
226. Elliott, L. A., Doherty, G. A., Sheahan, K. & Ryan, E. J. Human Tumor-Infiltrating Myeloid Cells: Phenotypic and Functional Diversity. *Front. Immunol.* **8**, 86 (2017).
227. Kodumudi, K. N. *et al.* A Novel Chemoimmunomodulating Property of Docetaxel: Suppression of Myeloid-Derived Suppressor Cells in Tumor Bearers. *Clin. Cancer Res.* **16**, 4583–94 (2010).
228. Chen, H.-M. *et al.* Myeloid-Derived Suppressor Cells as an Immune Parameter in Patients with Concurrent Sunitinib and Stereotactic Body Radiotherapy. (2015). doi:10.1158/1078-0432.CCR-14-2742
229. Umemura, N. *et al.* Tumor-infiltrating myeloid-derived suppressor cells are pleiotropic-inflamed monocytes/macrophages that bear M1- and M2-type characteristics. *J. Leukoc. Biol.* **83**, 1136–1144 (2008).
230. Ng, L. G. *et al.* Visualizing the Neutrophil Response to Sterile Tissue Injury in Mouse Dermis Reveals a Three-Phase Cascade of Events. *J. Invest. Dermatol.* **131**, 2058–2068 (2011).
231. Boogerd, L. S. F. *et al.* Concordance of folate receptor- $\alpha$  expression between biopsy, primary tumor and metastasis in breast cancer and lung cancer patients. *Oncotarget* **7**, 17442–54 (2016).
232. Kleinovink, J. W. *et al.* Combination of Photodynamic Therapy and Specific Immunotherapy Efficiently Eradicates Established Tumors. *Clin. Cancer Res.* **22**, 1459–1468 (2016).
233. Xu, J. *et al.* Near-Infrared-Triggered Photodynamic Therapy with Multitasking Upconversion Nanoparticles in Combination with Checkpoint Blockade for Immunotherapy of Colorectal Cancer. *ACS Nano* **11**, 4463–4474 (2017).
234. Hamberg, L. M. *et al.* Spatial heterogeneity in tumor perfusion measured with functional computed tomography at 0.05 microliter resolution. *Cancer Res.* **54**, 6032–6 (1994).
235. Wang, H.-W. *et al.* Effect of Photosensitizer Dose on Fluence Rate Responses to Photodynamic Therapy. *Photochem. Photobiol.* **83**, 1040–1048 (2007).
236. Jonathan Fine, Janez Konc, Ram Samudrala, G. C. CANDOCK: Chemical atomic network based hierarchical flexible docking algorithm using generalized statistical potentials. *bioRxiv* (2018). doi:10.1101/442897
237. Genazzani, A. R., Pluchino, N., Bernardi, F., Centofanti, M. & Luisi, M. Beneficial effect of tibolone on mood, cognition, well-being, and sexuality in menopausal women. *Neuropsychiatr. Dis. Treat.* **2**, 299–307 (2006).

238. de Gooyer, M. E., Deckers, G. H., Schoonen, W. G. E. ., Verheul, H. A. . & Kloosterboer, H. J. Receptor profiling and endocrine interactions of tibolone. *Steroids* **68**, 21–30 (2003).
239. Tannock, I. F., Lee, C. M., Tunggal, J. K., Cowan, D. S. M. & Egorin, M. J. Limited penetration of anticancer drugs through tumor tissue: a potential cause of resistance of solid tumors to chemotherapy. *Clin. Cancer Res.* **8**, 878–84 (2002).
240. Tetko, I. V. *et al.* Virtual Computational Chemistry Laboratory – Design and Description. *J. Comput. Aided. Mol. Des.* **19**, 453–463 (2005).
241. Whitfield, J., Littlewood, T. & Soucek, L. Tamoxifen administration to mice. *Cold Spring Harb. Protoc.* **2015**, 269–71 (2015).
242. Lam, H.-M. *et al.* Characterization of an Abiraterone Ultraresponsive Phenotype in Castration-Resistant Prostate Cancer Patient-Derived Xenografts. *Clin. Cancer Res.* **23**, 2301–2312 (2017).
243. Pitha, J. & Pitha, J. Amorphous water-soluble derivatives of cyclodextrins: Nontoxic dissolution enhancing excipients. *J. Pharm. Sci.* **74**, 987–990 (1985).
244. Hubbard, J. S., Chen, P. H. & Boyd, K. L. Effects of Repeated Intraperitoneal Injection of Pharmaceutical-grade and Nonpharmaceutical-grade Corn Oil in Female C57BL/6J Mice. *J. Am. Assoc. Lab. Anim. Sci.* **56**, 779–785 (2017).
245. Yu, R., Fujio, K., Tahara, H., Araki, Y. & Yamamoto, K. Clonal dynamics of tumor-infiltrating lymphocytes. *Eur. J. Immunol.* **35**, 1754–1763 (2005).
246. Leberbauer, C. Different steroids co-regulate long-term expansion versus terminal differentiation in primary human erythroid progenitors. *Blood* **105**, 85–94 (2005).
247. Jurczok, A., Fornara, P. & Söling, A. Bioluminescence imaging to monitor bladder cancer cell adhesion in vivo: A new approach to optimize a syngeneic, orthotopic, murine bladder cancer model. *BJU Int.* **101**, 120–124 (2008).
248. Clare, R. H. *et al.* Industrial scale high-throughput screening delivers multiple fast acting macrofilaricides. *Nat. Commun.* **10**, 11 (2019).
249. Evelyn, C. R. *et al.* High-Throughput Screening for Small-Molecule Inhibitors of LARG-Stimulated RhoA Nucleotide Binding via a Novel Fluorescence Polarization Assay. *J. Biomol. Screen.* **14**, 161–172 (2009).
250. Hevener, K. E. *et al.* in *Methods in Enzymology* 265–309 (2018). doi:10.1016/bs.mie.2018.09.022
251. Rose, P. W. *et al.* The RCSB Protein Data Bank: views of structural biology for basic and applied research and education. *Nucleic Acids Res.* **43**, D345–D356 (2015).
252. Chopra, J. F. R. L. R. S. G. Computational Chemoproteomics to Understand the Role of Selected Psychoactives in Treating Mental Health Indications. *ChemRxiv* (2018).



253. Minie, M. *et al.* CANDO and the infinite drug discovery frontier. *Drug Discov. Today* **19**, 1353–1363 (2014).
254. Sethi, G., Chopra, G. & Samudrala, R. Multiscale modelling of relationships between protein classes and drug behavior across all diseases using the CANDO platform. *Mini Rev. Med. Chem.* **15**, 705–17 (2015).
255. Chopra, G. & Samudrala, R. Exploring Polypharmacology in Drug Discovery and Repurposing Using the CANDO Platform. *Curr. Pharm. Des.* **22**, 3109–23 (2016).
256. Lees, J. R. *et al.* T-Cell Recognition of a Prostate Specific Antigen Is Not Sufficient to Induce Prostate Tissue Destruction. *Prostate* **66**, 578–590 (2006).
257. Kurts, C. *et al.* Constitutive class I-restricted exogenous presentation of self antigens in vivo. *J. Exp. Med.* **184**, 923–30 (1996).
258. Haverkamp, J. M. *et al.* An Inducible Model of Abacterial Prostatitis Induces Antigen Specific Inflammatory and Proliferative Changes in the Murine Prostate. *Prostate* **71**, 1139–1150 (2011).
259. Wang, H.-H. *et al.* Characterization of autoimmune inflammation induced prostate stem cell expansion. *Prostate* **75**, 1620–1631 (2015).
260. Cao, W. *et al.* Oxidized Lipids Block Antigen Cross-Presentation by Dendritic Cells in Cancer. *J. Immunol.* **192**, 2920–2931 (2014).
261. Inoue, T. *et al.* Hypoxia and Heat Inhibit Inducible Nitric Oxide Synthase Gene Expression by Different Mechanisms in Rat Hepatocytes. (2000). doi:10.1053/jhep.2000.18715
262. Cresswell, G. M. Folate Receptor Beta as a Marker of Immunosuppressive Myeloid Derived Suppressor Cells and Tumor Associated Macrophages in the Tumor Microenvironment. (Purdue University, 2018).
263. Catakovic, K., Klieser, E., Neureiter, D. & Geisberger, R. T cell exhaustion: from pathophysiological basics to tumor immunotherapy. *Cell Commun. Signal.* **15**, 1 (2017).
264. Fabregat, A. *et al.* The Reactome Pathway Knowledgebase. *Nucleic Acids Res.* **46**, D649–D655 (2018).
265. Fabregat, A. *et al.* Reactome pathway analysis: a high-performance in-memory approach. *BMC Bioinformatics* **18**, 142 (2017).
266. Matías-Román, S. *et al.* Membrane type 1-matrix metalloproteinase is involved in migration of human monocytes and is regulated through their interaction with fibronectin or endothelium. *Blood* **105**, 3956–64 (2005).
267. Ling, B. *et al.* A novel immunotherapy targeting MMP-14 limits hypoxia, immune suppression and metastasis in triple-negative breast cancer models. *Oncotarget* **8**, 58372–58385 (2017).

268. Burke, S. J. *et al.* Regulation of iNOS gene transcription by IL-1 $\beta$  and IFN- $\gamma$  requires a coactivator exchange mechanism. *Mol. Endocrinol.* **27**, 1724–42 (2013).
269. Schroder, W. A. *et al.* A physiological function of inflammation-associated SerpinB2 is regulation of adaptive immunity. *J. Immunol.* **184**, 2663–70 (2010).
270. Mühl, H., Bachmann, M. & Pfeilschifter, J. Inducible NO synthase and antibacterial host defence in times of Th17/Th22/T22 immunity. *Cell. Microbiol.* **13**, 340–348 (2011).
271. Liu, Y., Beyer, A. & Aebersold, R. On the Dependency of Cellular Protein Levels on mRNA Abundance. *Cell* **165**, 535–550 (2016).
272. Koussounadis, A., Langdon, S. P., Um, I. H., Harrison, D. J. & Smith, V. A. Relationship between differentially expressed mRNA and mRNA-protein correlations in a xenograft model system. *Sci. Rep.* **5**, 10775 (2015).
273. Vogel, C., Silva, G. M. & Marcotte, E. M. Protein Expression Regulation under Oxidative Stress. *Mol. Cell. Proteomics* **10**, M111.009217 (2011).
274. Banerjee, H. & Kane, L. P. Immune regulation by Tim-3. *F1000Research* **7**, 316 (2018).
275. Cook, K. D. & Whitmire, J. K. LAG-3 Confers a Competitive Disadvantage upon Antiviral CD8 + T Cell Responses. *J. Immunol.* **197**, 119–127 (2016).
276. Wherry, E. J. T cell exhaustion. *Nat. Immunol.* **12**, 492–499 (2011).
277. Kim, Y.-J., Aisen, A. T. & Broxmeyer, H. E. Myeloid-Derived Suppressor Cell Regulation of PD-1 Expression on, and Longevity of, Human CD8+ T Cells. *Blood* **112**, (2008).
278. Zhu, H. *et al.* CXCR2<sup>+</sup> MDSCs promote breast cancer progression by inducing EMT and activated T cell exhaustion. *Oncotarget* **8**, 114554–114567 (2017).
279. Yun, S. J. *et al.* Regulation of TIM-3 expression in a human T cell line by tumor-conditioned media and cyclic AMP-dependent signaling. *Mol. Immunol.* **105**, 224–232 (2019).
280. Soldin, O. P. & Mattison, D. R. Sex Differences in Pharmacokinetics and Pharmacodynamics. *Clin. Pharmacokinet.* **48**, 143–157 (2009).
281. Klein, S. L. & Flanagan, K. L. Sex differences in immune responses. *Nat. Rev. Immunol.* **16**, 626–638 (2016).
282. Lin, P.-Y. *et al.* B7-H1–Dependent Sex-Related Differences in Tumor Immunity and Immunotherapy Responses. *J. Immunol.* **185**, 2747–2753 (2010).
283. Strauss, L. *et al.* RORC1 Regulates Tumor-Promoting “Emergency” Granulo-Monocytopoiesis. *Cancer Cell* **28**, 253–269 (2015).
284. Cheng, H. S., Lee, J. X. T., Wahli, W. & Tan, N. S. Exploiting vulnerabilities of cancer by targeting nuclear receptors of stromal cells in tumor microenvironment. *Mol. Cancer* **18**, 51 (2019).

285. Fassò, M. *et al.* SPAS-1 (stimulator of prostatic adenocarcinoma-specific T cells)/SH3GLB2: A prostate tumor antigen identified by CTLA-4 blockade. *Proc. Natl. Acad. Sci. U. S. A.* **105**, 3509–14 (2008).